High Density Carbon Fiber Array Assembly Machine for Brain Electrophysiological Recordings

by

Tianshu Dong

A dissertation submitted in partial fulfillment
of the requirements for the degree of
Doctor of Philosophy
(Mechanical Engineering)
in the University of Michigan
2022

Doctoral Committee:

Associate Professor Cynthia A. Chestek, Co-Chair
Professor Albert J. Shih, Co-Chair
Assistant Professor Lei Chen, University of Massachusetts Lowell
Assistant Professor Nima Fazeli
Assistant Professor Brendon O. Watson

Tianshu Dong

tdong@umich.edu

ORCID iD: 0000-0002-4424-8337

© Tianshu Dong 2022

Dedication

To my Mom and Dad.

Acknowledgements

Striving for my Ph.D. degree has been the most challenging thing I have done so far in my life. I am truly grateful to the people who have helped me along the path. I will attempt to acknowledge all individuals who helped me achieve this goal.

First, I would like to express my deepest gratitude to my advisors, Professor Albert Shih and Professor Cindy Chestek, for their guidance, patience and support. I learned from Professor Shih in many aspects: conducting research, giving presentations, writing papers, pushing the limit, and keeping fit. Professor Chestek inspired me to divide and conquer, to distinguish the key factor, and most importantly, to celebrate and refresh between milestones. They both taught me how to be a better researcher and engineer. I am eternally grateful for their trust and confidence in me.

My most sincere gratitude also goes to my committee members. Professor Brendon Watson gave me the chance to participate in the application of multiple types of probes and offered great support in the rat tests. Professor Nima Fazeli helped me refine my research plans and accomplish the final steps to complete this research. Professor Lei Chen introduced me to the collaborators as a postdoctoral researcher when I joined the group and now passed on his toolbox, his experience, and his passion to me as a professor.

The topic of this research is novel and multidisciplinary, requiring profound understanding of neuroscience, biomedical engineering, and mechanical engineering, but I had no experience with the first two of the three prior to my graduate study. Fortunately, I met some

ingenious collaborators and they helped me get on track quickly. I would like to thank Paras Patel and Julianna Richie from the Cortical Neural Prosthetics Lab. It took them months even years to figure out how to cope with the single carbon fiber, but they condensed those experience and shared it with me without reservation. And they never hesitated to help whenever I reached out for scientific questions, on-site demos, and even lab equipment. They had my back all the time. I would also like to thank Jeremiah Hartner from the Watson Lab. Those rat tests could not be completed without his impeccable surgical skills. He offered great suggestions on refining our mechanical design as well.

It is my honor to be a member of the Biomedical Manufacturing and Design Lab (BMDL) and I would like to thank all my current and former lab mates. Jeff Plott, Robert Chisena, Yang Liu, Annie Dian-Ru Li, Ketut Bagus Putra, Albert Qianyi Fu, Matthew Hildner, Jingxuan (Jessie) Lyu, Chris Argenti, William van den Bogert, Hansen Li, and James Lorenz, it has been inspiring to share the knowledge, techniques, achievements and difficulties along our journey towards the doctoral degree. Yihao Zheng, Miguel Funes, and Zhaokun (Brandon) Zhang, you helped me greatly as postdoctoral researchers with your experience, insights and resources. Special thanks go to David Van Dyke, Chris Symonds, Zackary Witte, and Su Sung Kim, who have been working with me on this research at different stages. They did great jobs, and their passion has always been encouraging.

I am thankful to my friends that I met here: Fangyuan Chang, Haokui Xu, Hongmei Tang, Jin Li, Lu Wen, Menglou Rao, Xiao Zhu, Xiaofan Cui, Xiaotian Tan, Yuguo Zhong, Yuhao Wang, Yuqing Huang and Zhuo Chen. It is you that keep me socialized by parties, trips, and workouts after the pandemic strikes the world. I would like to specially thank Xin Zan for organizing those amazing trips, initiating cheer-up talks when we were both struggling with our

thesis, and being my matchmaker; thank Qicang Shen for helping me out in many situations and offering great suggestions as one of the most rational person I have ever met; thank Liang Yao for being an amazing roommate and keeping an eye on me after I got my booster shot.

I would like to thank Xiaozhi Yu for the emotional, physical and technical support over the past months.

Finally, my most heartfelt thanks go to my mom and dad. You always support me unconditionally. Without you, none of this would have been possible and I owe you everything. I miss you. I love you.

Thank myself for not giving up.

Table of Contents

Dedication ii

Acknowledgements iii

List of Tables ix

List of Figures x

Abstract xiv

Chapter 1 Introduction 1

1.1 Electrophysiology and microelectrode arrays 1

1.2 Carbon fiber electrode arrays 3

1.3 Gaps in research and dissertation organization 6

Chapter 2 Laser Cutoff and Sharpening of Carbon Fiber Electrodes 9

2.1 Introduction 9

2.2 Carbon fiber electrode sharpening experimental setup 10

2.3 Sharpening procedure 12

2.3.1 Cutting path planning 12

2.3.2 Adjusting laser focus on a carbon fiber tip 13

2.3.3 CFE cutoff and sharpening 13

2.4 Experimental investigation of the laser speed, input voltage, and fabrication of CFE array with custom electrode lengths 14

2.5 Results and discussions 17

2.5.1 Exp. I: Laser speed for cutting off carbon fibers 17

2.5.2 Exp. II: Tip angle and profile 18

2.5.3 Exp. II: Stripped length of Parylene C insulation 22
2.5.4 Exp. II: Impedance of laser sharpened carbon fiber electrodes and in-vivo recordings 22
2.5.5 Exp. III: Fabrication of an array with custom electrode lengths 23
2.6 Conclusions 24
Chapter 3 Algorithms for Automatic HDCF Array Assembly 25
3.1 HDCF array and its components 26
3.2 HDCF array assembly procedure 29
3.3 Algorithm I: CF-shank orientation alignment 31
3.3.1 Input and output variables 32
3.3.2 Orientation measurement 32
3.4 Algorithm II: CF tip – gold pad edge center alignment 36
3.4.1 Input and output variables 36
3.4.2 Datum edges extraction and distance calculation 37
3.5 Experiments for Algorithms I and II performance evaluations 40
3.5.1 Exp. I: CF deviation angle reduction with Algorithm I application 40
3.5.2 Exp. II: CF tip positioning accuracy using Algorithm II 41
3.5.3 Parameter selection for Algorithm II 44
3.6 Conclusions 45
Chapter 4 High Density Carbon Fiber Array Assembly Machine 46
4.1 Overview of the HDCF array assembly machine 47
4.1.1 Subsystem 1: Roller-based extruder 49
4.1.2 Subsystem 2: Motion system 51
4.1.3 Subsystem 3: Imaging system 51
4.1.4 Subsystem 4: Laser cutter 53
4.1.5 Controller and software platform 54

4.2 Carbon fiber electrodes population 55
4.3 Subsystem tests and results 56
4.3.1 Exp. I: Effect of Parylene C coating in the extruder capillary tubes 56
4.3.2 Exp. II: the CF extrusion accuracy of the roller-based extruder 57
4.3.3 Exp. III: Effect of translational speed in the z-direction on CF placement 58
4.4 HDCF assembly machine evaluation 59
4.4.1 Duration of assembly steps 59
4.4.2 Failure analysis 60
4.4.3 EIS and in-vivo electrophysiology recording with assembled HDCF arrays 62
4.5 Conclusions 65
Chapter 5 Conclusions and Future Work 66
5.1 Conclusions 66
5.2 Future work 67
Appendix Flexible High-Resolution Force and Dimpling Measurement System for Pia and Dura Penetration During In Vivo Microelectrode Insertion Into Rat Brain 70
Bibliography 92

List of Tables

Table 2.1: Carbon fiber cutoff speed, tip profile, tip angle, and stripped length results under three laser input voltages 18

Table 4.1: Estimated time of each assembly step 60

Table A. 1: Design parameters of four cantilever beams used in the study..... 73

Table A. 2: Correlation coefficients from calibration results 75

Table A. 3: Cantilever beam selection for each microelectrode based on preliminary insertion tests 80

Table A. 4: Membrane penetration success rates..... 83

Table A. 5: Analysis of variances (ANOVA) results of microwire insertions 87

Table A. 6: Correlation between rupture force and dimpling depth at rupture..... 89

List of Figures

Figure 1.1: Silicon-based MEAs: (a) Utah array [27] and (b) Michigan probe [28]. 3

Figure 1.2: Two types of CFE array configuration: (a) bundle array [6] and (b) linear array [8]. . 5

Figure 1.3: Automatically assembled CFE arrays with 32 μm pitches [39] 6

Figure 2.1: Laser CFE sharpening setup: (a) an overview of the three-axis motion system, stationary camera and PCB, (b) close-up view of the laser head, camera and PCB and (c) camera view of the 1 x 4 carbon fiber array on the PCB. 11

Figure 2.2: Schematic diagram of cutting path: (a) Path I for a uniform CFE length and (b) Path II for CFE arrays with custom electrode lengths. 12

Figure 2.3: The light spot on the CF when the laser beam hit the CF. 13

Figure 2.4: Scanning electron microscope (SEM) pictures of the carbon fiber with Parylene C insulation: (a) before cutting, (b) partially cut off at 25 μm/s and 4 DCV laser input voltage and (c) fully cut off with sharpened conical tip at 20 μm/s and 4 DCV laser input voltage. 15

Figure 2.5: Evaluation metrics for (a) tip profile L_1, L_2, and L_3: the distances between tip and the positions which correspond to $D_2 = 0.2D_1$, $0.5D_1$, and $0.8D_1$, (b) tip angle α, and (c) stripped length S: the distance from the tip to the end of the stripped region. 16

Figure 2.6: Four tips from (a) 5, (b) 4 and (c) 2.5 DCV input. Serrated asymmetric profiles were observed. 19

Figure 2.7: Tip geometry under three laser power levels: tip profile L_1, L_2, L_3, tip angle α and stripped length S. 20

Figure 2.8: Acute electrophysiological spiking data from four laser sharpened CFEs [49]. 23

Figure 2.9: Exp. III results: (a) snapshots of ongoing cutting and sharpening process to get an array of carbon fiber in different lengths (with l_1 = 1.2 mm, l_2 = 1.2 mm, l_3 = 1.6 mm, and l_4 = 1.4 mm in Figure 2.2) and (b) SEM image of the array. 24

Figure 3.1: (a) CFE parallelization mechanism with the device and assistive substrates and (b) CF-hole alignment algorithm: the image of a hole as a template, automatically detected hole positions (teal) and tagged CF positions (yellow) before alignment, and CF alignment with the hole after moving substrates [39,51]. 26

Figure 3.2: (a) HDCF array components: connector, custom PCB, SSS, and CFEs, (b) SSS components, features, and dimensions, and (c) CFEs started from the silver epoxy wells and overhangs from the trenches. 28

Figure 3.3: The SSS fabrication process: Cross-sectional diagram of the shanks and trenches region (A-A) and the silver epoxy wells and gold pads region (A'-A'). 29

Figure 3.5: (a) Seven steps of HDCF array assembly, (b) the connector, PCB, and silicon support structure connected physically and electrically, and (c) SEM photos of CFE tip after sharpening, PEDOT:pTS coating, and PtIr coating (insulation above the arrow removed) [42]. 31

Figure 3.6: The measurement of β_1 and β_2. Green solid lines are the lines extracted from the image. 32

Figure 3.7: Each entry of $\boldsymbol{H}((r_0, \theta_0)$ represents the line $r_0 = x\cos\theta_0 + y\sin\theta_0$ 34

Figure 3.8: Measurement of β_1 and β_2 in Algorithm I. 35

Figure 3.8: Algorithm II: inputs, outputs, and datum edges. 36

Figure 3.9: Algorithm II for Δx and Δy calculation: (a) Input I0, (b) Step 1 I1, (c) Step 2 I2, (d) Step 3 I3, (e) Step 4 $\boldsymbol{H}$ and peaks, (f) Step 5 n extracted lines, (g) Step 6 two datum edges (green) and datum points (red), and (h) Step 7 calculated gold pad edge centers (red), target edge center (yellow), Δx and Δy. 39

Figure 3.10: Definition of CF deviation angle θ_{xy} 40

Figure 3.11: CF tip positioning accuracy in (a) x- and (b) y- directions after first iteration of Algorithm II. The failure area is shaded with ε_{x1} larger than 40 μm. 42

Figure 3.12: (a) ε_x after the first and second Algorithm II iterations (the failure area is shaded with ε_{x2} larger than 40 μm), and (b) ε_y of repeated Algorithm II application. 43

Figure 3.13: Cases not working with default (b, n) = (75, 10) and required parameter searching: (a) searching Step 1 applied, detection works when $b \in [83, 89]$, $n = 10$ and (b) searching Steps 1 and 2 applied, detection works when $b = 75$, $n \in [2, 6]$. 45

Figure 4.1: HDCF array assembly system and its four subsystems: (a) 3D overview of the 1) roller-based extruder, 2) motion system, 3) imaging system, and 4) laser cutter, together with the PCB with SSS as the starting workpiece, (b) close-up view of the red-boxed area in figure 2A including the PCB with SSS, camera (in the imaging system), and CF (from the roller-based extruder); pictures of (c) the physical machine and (d) close-up view of the roller-based extruder, the PCB with SSS, Camera #1, and the CF. 48

Figure 4.2: Roller-based extruder: (a) overview of the adjustable base, the rollers, the motor, and the glass capillary tubes, (b) the adjustable base, (c) rollers and shaft with soft silicone coating (colored in transparent azure) and CF extrusion mechanism (motions are marked in red arrows),

and (d) a photo of CF being advanced from capillary tube #1 to capillary tube #2 by the friction from the rollers. 50

Figure 4.3: (a) Motion system: three linear stages for PCB translation in x-, y- and z-directions and the rotary stage R for CF rotation and (b) the rotary stage rotates the roller-based extruder, the imaging system, and the laser cutter together (top view). 52

Figure 4.4: Imaging system: (a) camera #1 and camera #2, (b) top view of assembly area from camera #1, and (c) side view of assembly area from camera #2. 53

Figure 4.5: (a) Laser cutter components: laser head, motorized linear stage, and manual linear stage and (b) laser beam cutting off the CF (top view). 54

Figure 4.6: Photos from camera #2 (a) before and (b) after the deionized water application around the epoxy covering the wire bonds between the SSS and the PCB. 55

Figure 4.7: CF landing: (a) CF tip touching the gold pad and (b) CF pulled into the trenches on the shanks by the surface tension of the water. 56

Figure 4.8: Parylene C coated capillary tube exhibiting more static charges and attracting CF from a larger distance. 57

Figure 4.9: CF extrusion length measurement based on the pixel of the CF tip (blue circle) with the capillary tube diameter as the scale. 58

Figure 4.10: Shank breakage due to deionized water application. 61

Figure 4.11: CFE escaped from the trench: (a) CFE landed in the trench before cutting and (b) CFE deviated from the shank and touched the nearby CFE. 61

Figure 4.12: (a) Fully populated HDCF array and (b) the closed-up view of CFEs on the gold pads (before silver epoxy application). 63

Figure 4.13: (a) Bode magnitude plots of the measured impedance after the three major functionalization steps (n=27 fibers, mean ± SD) and (b) one kilohertz impedance values (n=27 fibers, mean ± SD) shown for the three major processing steps. As seen in previous results, coating with PEDOT:pTS greatly reduces the impedance of the electrodes. 64

Figure 4.14: Spike panel of the detected unit activity from layer V motor cortex of an anesthetized rat. 64

Figure 5.1: Automatic water pool refill using a water pump to constantly dispense deionized water on the SSS for compensation of the water evaporation. 68

Figure A. 1: The in vivo microwire force measurement system: (a) conceptual overview, (b) side-view of cantilever beam bending during insertion, and (c) perspective view of experimental setup with anesthetized rat. 72

Figure A. 2: FEM of the cantilever beam system with Beam #1 as example: (a) model configuration overview, (b) FEM mesh setup, and (c) perspective and side views of the beam deflection result under 6 mN load. 74

Figure A. 3: Calibration results of mapping between (a) F_i and d_c and (b) d_l and d_c for four different cantilever beam structures. 75

Figure A. 4: Experimental setup of microwire force measurement system: (a) anesthetized rat test setup overview and (b) close-up view of the microwire insertion into exposed rat brain. 78

Figure A. 5: Microelectrodes used in the animal insertion tests: (a) scanning electron microscope images of various microwires and (b) single- and dual- shank silicon probes from Buzsaki64 – H64LP probe by Neuronexus fixed in capillary tube. 81

Figure A. 6: Sample force profiles of tungsten microwires: (a) blunt and (b) sharp microwires for pia-only penetration and (c) blunt and (d) sharp microwires for dura-pia penetration. 85

Figure A. 7: The (a) pia-only and (b) dura-pia rupture force during microwire insertions and dimpling depth at (c) pia-only and (d) dura-pia penetration by different microwires. Average value of each condition is plotted with standard error as the error bar. 85

Figure A. 8: Rupture force and dimpling depth of pia-only penetration by silicon probes containing various number of shanks. Average value of each condition is plotted with standard error as the error bar. 90

Abstract

Carbon fiber electrodes (CFEs) are ideal for chronic electrophysiological recordings because of their small diameter (5 to 10 μm), high Young's modulus (241 GPa), and low electrical resistivity. To minimize buckling during CFE array implantation, electrodes are sharpened to reduce the insertion force and attached to a support structure to reduce the unsupported length. The thin carbon fiber (CF) requires great hand stability and is labor-intensive to cut, sharpen, and assemble the array. The aim of this research is to develop a laser CF cutting and sharpening method enabling custom electrode lengths and to build a high density carbon fiber (HDCF) array assembly machine that can precisely place the CFEs along with the thin silicon support structure (SSS).

The first study established a CFE cutting, sharpening, and insulation removal method using a moving laser beam. Custom lengths of CFEs in an array were achieved in one cut by designing the laser moving path. The combination of high laser input voltage (5 DCV) and large moving speed (25 μm/s) resulted in a sharp tip (27.9°) and short insulation stripped length (122.5 μm). Custom electrode lengths of 1.2, 1.2, 1.6, and 1.4 mm were realized in a CFE array with 200 μm pitch. The laser sharpened CFEs had an electrochemical impedance spectroscopy (EIS) measurement of 460 ± 225 kΩ at 1 kHz, which was significantly lower than that of scissor cut or torch burned CFEs. The in-vivo recording performance in rat motor cortex was comparable with CFEs sharpened with torch burning.

The second study developed two image-based algorithms for aligning the CF with other parts of the HDCF array as the foundation for the HDCF assembly machine. The HDCF array

has a printed circuit board (PCB) with an Omnetics connector and a SSS with gold pads and shanks. The Algorithm I measured the difference between the orientation of the CF and the shanks and corrected the deviation by rotating the CFE. The deviation angle was reduced from 1.16 ± 0.94 to 0.54 ± 0.51 degrees after rotation compensation. Algorithm II calculated the distance between the CF tip and the target position on gold pads and translated the PCB to get them aligned. The error was less than 40 μm for 91.7% of the placement tests.

The third study constructed an HDCF array assembly machine for automatic precise placement of CFEs, integrating the algorithms developed in the second study. CFEs were placed along shanks of SSS using the machine, which had four subsystems: 1) a roller-based extruder adapted from an open-source system, 2) a motion system, 3) an imaging system, and 4) a laser cutter. The CF was extruded from the extruder, rotated parallel to and translated to place along a trench in the shank of SSS by the motion system, and cut off by the laser. With the Parylene C coating on its tube, the extruder achieved 4.009 ± 0.073 mm for a target of 4 mm in extrusion length. The delicate and stable adjustment of CF orientation and SSS position ensured their great alignment. Two HDCF arrays of 16 and 8 CFEs with 80 μm pitch were assembled without manual manipulation of CF after the initial loading.

Future work of this research includes automating the water dispensing and expanding the application to arrays with other electrode materials and configurations.

Chapter 1 Introduction

Electrophysiological recordings are conducted to measure electrical activities in the brain. Microelectrode arrays (MEAs) are implanted to perform single unit recordings, tracking the field potentials of discharging neurons, and revealing the fundamental correlations between the excitability and discharge patterns [1,2]. Microwire-based MEAs have thin electrodes with the flexibility to mitigate the immune response and rigidity for implantation and demonstrated their capability of recording over several months [3–5]. Among various microwire materials, carbon fiber (CF) has the smallest diameter of 5 to 10 μm, low electrical resistivity, and good biocompatibility. These characteristics have made CF electrodes (CFEs) ideal for chronic recording [6,7]. Most CFE arrays for neural recording are manually assembled. The process is labor-intensive, time-consuming, and limited by the accuracy and repeatability of human operations to build fine pitch (smaller than 150 μm) CFE arrays. The primary focus of this dissertation is to demonstrate the novel manufacturing methods to break this limitation in CF MEA manufacturing, including CFE tip sharpening and automatic CFE array assembly.

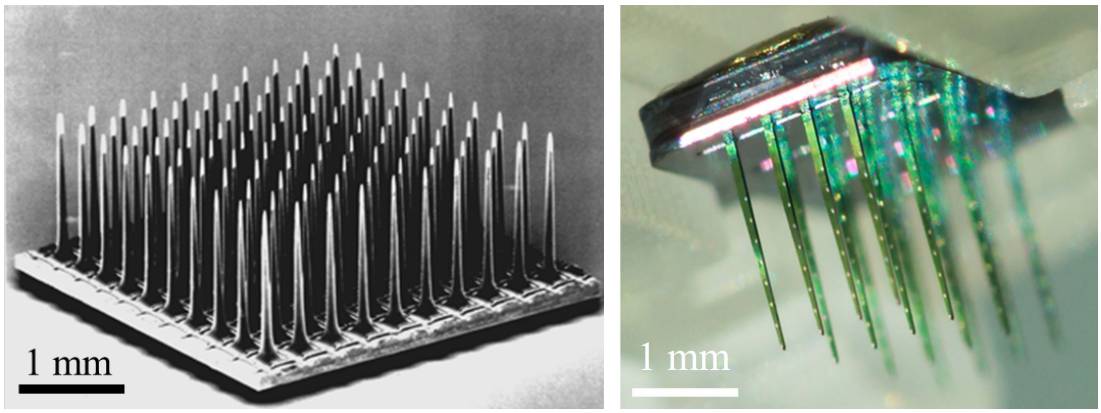
1.1 Electrophysiology and microelectrode arrays

Electrophysiological recordings contribute to both the study of neurophysiological mechanisms and the construction of brain-machine interfaces [3,8–10]. The human brain consists of about 86 billion neurons, and each neuron communicates with 7,000 other neurons on average via axons through electric signals generated by Na^+ and K^+ ion transportation across the membrane [11]. Single neuronal firing generates 80 to 100 mV change in potential in

milliseconds and is only distinguishable within an approximately 150 μm radius [12]. Single unit recordings help reveal the fundamental correlations between the excitability and discharge patterns of the central nervous system and animal behaviors such as vision, sleep and wakefulness, and movement [11–14]. Electrophysiology methods like electroencephalography (EEG), magnetoencephalography (MEG), and functional magnetic resonance imaging (fMRI) lack the spatial and/or temporal resolution to record the single neuron activities [15,16]. Implantation of MEAs in the brain places recording sites next to neurons and enables the electrophysiological recording of single neuron actions [15,17].

There are three types of MEAs: silicon-based MEA, flexible MEA, and microwire MEA. Silicon-based MEAs, like the Michigan Probe [18] and Utah Array [19], stimulate the formation of scar tissue due to the rigidity of silicon electrodes and can lead to a signal loss over a few weeks after the implantation in the brain [20,21]. Flexible MEAs are built on thin (typically 4 to 14 μm in thickness) polyimide, which has great flexibility and biocompatibility [22,23]. However, the thin polyimide has low stiffness and requires a thick shuttling device (e.g. a 30 μm thick silicon stiffener [22] or a Tungsten-Rhenium needle of 40 μm diameter [23]) to facilitate the implantation, causing extra brain trauma and affecting long-term recording quality.

Microwire MEAs use fine cellular-scale microwires as the recording electrodes. Microwire MEAs are made of different biocompatible materials, including 5 to 10 μm diameter carbon fiber [5,6,8,24] and 10 to 75 μm diameter metal (tungsten, stainless steel, platinum-iridium, etc.) [3,9,25,26], have been developed and implanted for the recording of neuron signals in the brain. The small diameter of these microwires gives the flexibility to prevent the formation of scar tissue and enable long-term recording (e.g. over three months using carbon fiber [24]).



(a) (b)

Figure 1.1: Silicon-based MEAs: (a) Utah array [27] and (b) Michigan probe [28].

1.2 Carbon fiber electrode arrays

Among various microwire materials, carbon fiber (CF) has the smallest diameter of 5 to 10 μm [29], minimizing the immune responses. CF also has a low electrical resistivity, which facilitates the detection of low voltage signals without noise contamination [30]. These characteristics have made carbon fiber electrodes (CFEs) ideal for chronic recording [24,29,30].

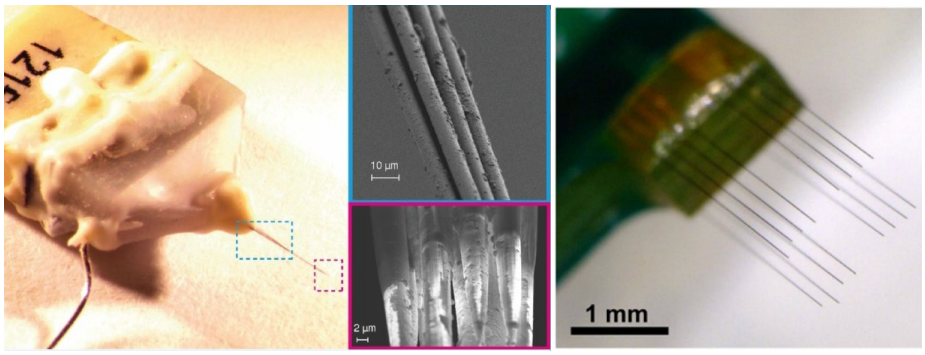
The electrode tips in microwire MEAs are often sharpened to reduce the insertion force and avoid microwire buckling during insertion [31–33]. Three methods are currently applied in CFE tip sharpening. The first is torch burning [6,34,35]. Tips of CFEs of an assembled array are protruded over the surface of a water bath. A torch passes over the water surface to burn off and sharpen the CFE. This method applies only to CFE arrays with tips aligned in the same plane. CFE arrays with custom electrode lengths are necessary when recording neuron activities from multiple layers at different depths from the curved brain surface [36]. The second sharpening method is electrical discharge machining (EDM) [37]. A tungsten cathode was brought within a few microns from the CFE tip to create electrical discharges and generate a conical sharp tip. The third method is electrochemical machining (ECM) [38]. Both ends of CF were submerged in saline and the tip was etched with 9V 60Hz alternating current. For CFE arrays with electrical-

insulated Parylene C coating [6,8,39], the tips are not electrically conductive for EDM or ECM sharpening. The study aims at developing a new cutting and sharpening method enabling arbitrary CFE lengths.

Two configurations of CFE arrays are: 1) bundle and 2) linear array, as shown in Figure 1.2. The bundle CFE array was first developed by Guitchounts et al. using 16 CFEs threaded by hand through a 3D-printed plastic block, dipped in a water bath with surplus fiber section exposed in the air, and trimmed along the water surface by torch burning [6]. This design of bundle CFE array was expanded to 64 CFEs [34]. Based on the same technique, Lee et al. [40] constructed a bundle of 4 CFEs and added a biodegradable silk fibroin support to facilitate the deeper penetration into the brain. The bundle CFE array has a high local recording density but sacrifices the spatial coverage and the miniature size advantage of the CFE.

The linear CFE array could overcome limitations of bundle CFE by using individual CFEs distributed in a high spatial density. There are two fabrication methods for high density carbon fiber (HDCF) arrays: manual and automatic assembly. For manual fabrication, Patel et al. [8,24] constructed the first linear HDCF array with 16 CFEs in a 150 μm pitch. The array was constructed using a printed circuit board (PCB) with 16 gold traces. Silver epoxy was dispensed on the gold traces and the CF was placed in the epoxy pool manually under a microscope. Then the silver epoxy was cured, held CFEs in place, and established the electrical connection between the CFE and PCB. An array with 16 CFEs in 132 μm pitch on a flexible polyimide PCB was built and a 532 nm laser was applied to replace scissors for cutting the CFE [7,41]. Huan et al. applied a silicon support structure for the 16 CFE array with 80 μm pitch to achieve up to 9 mm insertion depth [42]. Individual CF was cut to length and manually placed along the shanks in the

silicon support structure using forceps. This manual assembly of CF MEA is labor-intensive, time-consuming, and limited by the accuracy and repeatability of the operator.



(a) (b)

Figure 1.2: Two types of CFE array configuration: (a) bundle array [6] and (b) linear array [8].

For automatic fabrication of HDCF arrays, Massey et al. [39] proposed an automated microassembly method to build a 32-channel CFE array with 32 µm pitches. Using a silicon substrate with holes in a grid, a CF extruded from a movable roll feeder is guided using the microscope camera, motion stages, and control algorithm to find the holes in the image and to align the tip of CFE with each hole. During assembly, an assistive substrate with identical holes was aligned with the base substrate. The CF was inserted into holes in both substrates and soldered at holes in the device substrate using the silver epoxy. The assistive substrate was moved in the fiber direction towards and away from the device substrate periodically and formed a CFE parallelization mechanism. Small pitch distance and high assembly accuracy were realized using high precision linear stages. However, there is a practical problem with 2.5 to 3 mm of CFE length because the large unsupported length would lead to buckling during implantation [43]. To ensure the accuracy and facilitate a deep insertion even up to 9 mm, the unsupported length needs to be reduced, which could be realized if the CFEs are secured on a

minimally invasive support structure. This study is aimed to develop a new automatic assembly method for placing CF along a thin support structure with high precision.

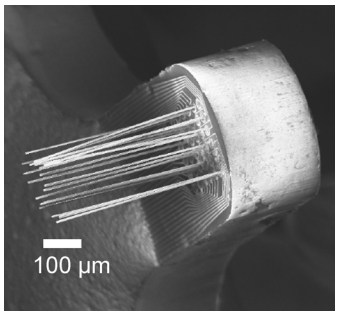


Figure 1.3: Automatically assembled CFE arrays with 32 µm pitches [39]

The motivation of the research elaborated in this dissertation is to break the limitation in CF MEA research application which mainly comes from the demanding manual operations of single carbon fiber and the long training period of highly specialized personnel. The small dimensions of CFEs and compact configurations of HDCF arrays limit the space for operation and assistant devices, leading to great difficulties in the handling of materials and visualization of the fabrication process. Therefore, an HDCF array assembly system is desired if it provides clear visual monitoring and minimizes the manual handling of CFEs with high precision and stability requirements.

1.3 Gaps in research and dissertation organization

This dissertation aims to develop an automatic assembly machine for HDCF array for brain electrophysiological recording. Two key gaps in research addressed by this dissertation are: 1) lacking studies investigating the CFE cutoff and sharpening method enabling custom lengths for each electrode in an array and 2) the automatic HDCF array assembly machine. To address these two gaps, the research goals are to: 1) develop a laser CF cutoff and sharpening method

with adjustable cutting path, and 2) build an HDCF array assembly machine that is able to precisely place CFEs along with the thin support structure.

In Chapter 2, a moving laser beam was traced across the CF to realize the cutting, sharpening, and insulation removal of CFEs in an array with custom electrode lengths simultaneously. The effect of laser input voltage and moving speed were investigated on the sharpness and insulation stripped length of the CF tip. The laser path was designed based on targeted electrode lengths. To validate the function of the laser sharpened CFEs, electrochemical impedance spectroscopy (EIS) and an in-vivo recording in rats were conducted. An array of four laser sharpened CFEs was evaluated, proved functional in EIS impedance, and its in-vivo recording performance was comparable with CFEs sharpened with other established methods.

In Chapter 3, two image-based algorithm was developed for aligning the CF with other parts of the HDCF array during assembly. The HDCF array has a printed circuit board (PCB) with an Omnetics connector and a silicon support structure with gold pads and shanks. Both algorithms used images taken from the top of the CF and the PCB as input. The first algorithm measured the difference between the orientation of the CF and the shanks. The second algorithm calculated the distance between the CF tip and the desired target on gold pads which the tip would land on. Four parameters within the algorithm can be selected based on some searching strategies, to provide some flexibility under different working conditions.

In Chapter 4, an HDCF array assembly machine was constructed for automatic precise placement of CFEs with an 80 μm pitch. CFs are placed along shanks (with an 80 μm pitch) of the silicon support using the HDCF array assembly machine, which has four subsystems: 1) a roller-based extruder to advance the CF, 2) a motion system to translate the PCB and rotate the CF extruder, 3) an imaging system with two microscope cameras, and 4) a laser cutter to cut off

the CFs. CF got extruded from the roller-based extruder, paralleled to the shanks by rotating the extruder, then placed along shanks by moving PCB, and lastly cut off by the laser cutter. A water pool was applied on shanks to facilitate CF placement with surface tension. Three subsystem tests were conducted on extruder performance and accuracy, and the effect of motion system speed on placement outcome. The machine was tested by assembling an HDCF array with 16 CFEs. Failures were characterized and plausible solutions were proposed.

In Chapter 5, a summary of the findings in this dissertation is provided. Insights into the future directions of this work are offered.

Chapter 2 Laser Cutoff and Sharpening of Carbon Fiber Electrodes

The work introduced in this chapter has been published at Journal of Micro- and Nano-Manufacturing and Tianshu Dong is the first author [44].

The electrode tips in microwire MEAs are often sharpened to reduce the insertion force and avoid microwire buckling during insertion [31–33,45]. MEAs with custom electrode lengths are necessary when recording neuron activities from multiple layers at different depths from the curved brain surface [36]. Among various methods applied in CFE tip sharpening: torch burning applies only to CFE arrays with tips aligned in the same plane [6,34,35], while ECM and EDM are not suitable for CFEs with an electrical-insulated Parylene C coating [6,8,37–39,46]. With a moving laser beam, a new CF cutting and sharpening method is elaborated, enabling the cutoff and sharpening of Parylene C insulated CFEs with custom lengths.

2.1 Introduction

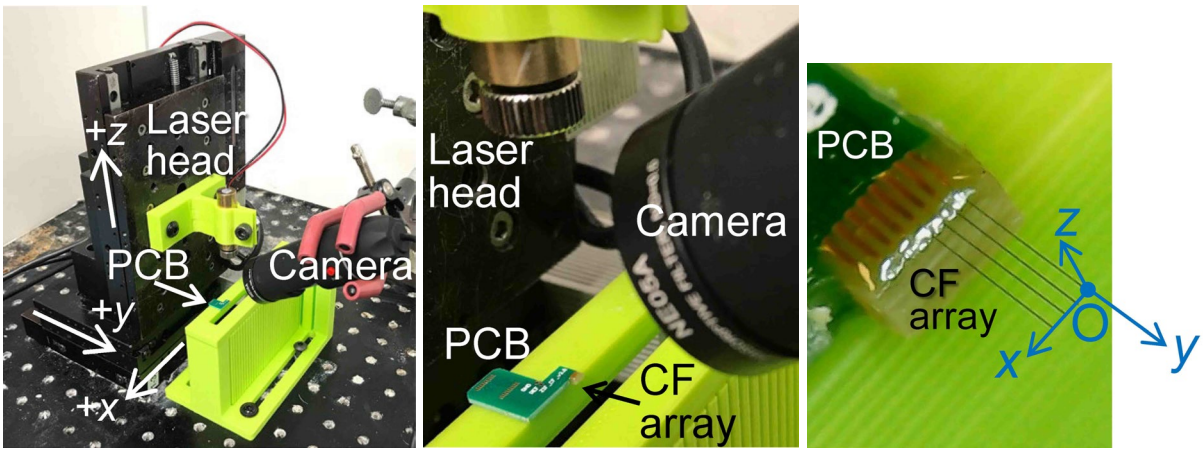
A laser-based carbon fiber cutoff and sharpening method proposed in this chapter enables the fabrication of CFE arrays with sharp tips and custom lengths. Experiments were conducted to study effects of laser input voltage and transverse speed on CFE tip geometry. Results of the tip sharpness and stripped length of the insulation as well as the electrochemical impedance spectroscopy (EIS) measurement at 1 kHz were evaluated and analyzed. The laser input voltage and traverse speed have demonstrated to be critical for the sharp tip, short stripped length, and low electrical impedance of the CFE for brain recording MEAs. A CFE array with custom

electrode lengths was fabricated to validate the laser-based approach. In-vivo recording with rats was also performed to test the function of laser sharpened CFEs.

2.2 Carbon fiber electrode sharpening experimental setup

The experimental setup, as shown in Figure 2.1, consisted of a 3-axis motion system, a laser head, a microscope camera for process monitoring, and a PCB with carbon fibers. The motion system was composed of three orthogonally configured linear stages. Two horizontal linear stages (200cri-R by Siskiyou, Grants Pass, OR) were denoted as *x* and *y*. The vertical linear stage *z* (100cri-R by Siskiyou, Grant Pass, OR) carried the laser head and could be moved horizontally by the *x* and *y* linear stages. The positive directions of motion for linear stages *x*, *y* and *z* are marked in Figure 2.1 (a) and denoted as positive *x*-, *y*-, and *z*-directions, respectively. The positioning accuracy of all three linear stages was 2 μm and the 3-axis motion was coordinated through the same controller (PCI-7344 by National Instruments, Austin TX). Both the PCB and camera were stationary. A multimode InGaN semiconductor laser (1.5 W maximum output power and 405 nm violet wavelength) made by WER (Shanghai, China) was fixed on the linear stage *z* and pointing down in the negative *z*-direction. The laser head was 12 mm in diameter and 40 mm in length. The convex lens attached to the laser head had a focal length of 100 mm. The laser beam had a 1 mm depth of focus and a 75 μm beam waist radius. It had a 1.5 W maximum power under the 5 DCV input voltage and the lower input voltage can be adjusted to reduce the laser power. The multimode InGaN semiconductor lasers are widely used as engraver lasers and are of compact size, enabling their broad integration in biomedical and neuroscience research labs. This specific laser had the suitable power (1.5 W maximum) to cut off and sharpen 6.8 μm diameter carbon fibers in this study.

A 1 × 4 carbon fiber array was fixed at the side of the PCB, which was stationary and located on a fixture, as shown in Figure 2.1(a). The close-up view of the PCB on the fixture is shown in Figure 2.1(b). The close-up view of the four carbon fibers in PCB is shown in Figure 2.1(c). The 6.8 μm carbon fiber (T-650/35 3K by Cytec Thornel, Woodland Park, NJ) had 800 nm thick Parylene C coating by chemical vapor deposition (using PDS-2010 by Specialty Coating Systems, Indianapolis, IN) for electrical insulation. All four carbon fibers on the PCB had Parylene C coating, 8.4 μm in diameter (coating included), 2 mm overhanging length, and 200 μm pitch. As shown in Figure 2.1(c), these four carbon fibers were placed horizontally in the *xy* plane and aligned along the *y*-direction. The distal end of the first carbon fiber in the array was assigned as the origin, marked as point O. Four carbon fibers were accurately aligned in the *xy* plane with their variation in height in the *z*-direction less than 250 μm, which is less than a quarter of the laser depth of focus and ensures the laser cutting zone coverage of all carbon fibers.



(a) (b) (c)

Figure 2.1: Laser CFE sharpening setup: (a) an overview of the three-axis motion system, stationary camera and PCB, (b) close-up view of the laser head, camera and PCB and (c) camera view of the 1 x 4 carbon fiber array on the PCB.

2.3 Sharpening procedure

Three steps were taken for CFE sharpening. First, a cutting path for laser head motion is planned according to the desired electrode lengths. Second, the laser was first adjusted to focus at the tip of the carbon fiber by moving linear stages x, y and z. Last, the CFEs were cut off and sharpened. The laser head was guided by two linear stages (xy) along the planned path in a horizontal plane with linear stage z remained stationary. Three steps are introduced in Sections 2.3. 1, 2.3.2 and 2.3.3 respectively.

2.3.1 Cutting path planning

Two types of cutting paths, denoted as Path I and Path II, in the xy plane are planned as shown in Figure 2.2. The center of the laser focal spot was in the carbon fiber plane ($z = 0$) for cutting and sharpening. In Path I, as shown in Figure 2.2(a), the laser was moved along a straight line in the x-direction across all four carbon fibers. The CFEs had a uniform length. In Path II, the laser was moved in both the x- and y-directions to fabricate a CFE array with varying electrode lengths shown as l_1, l_2, l_3, and l_4 in Figure 2.2(b).

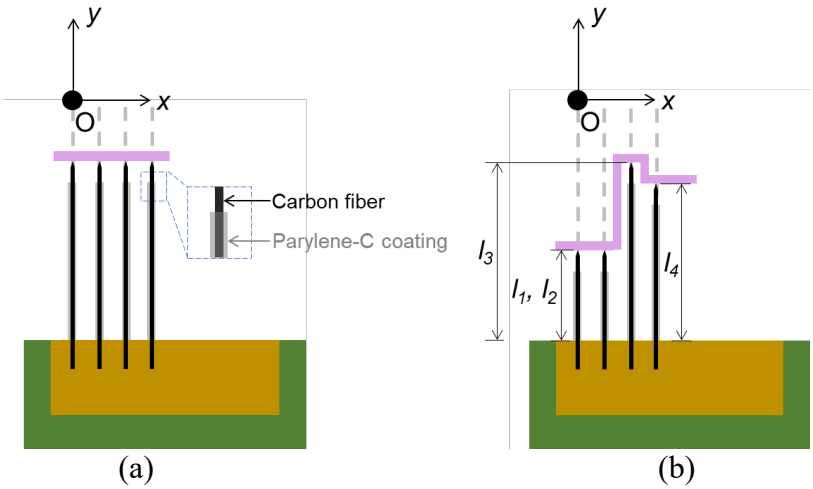


Figure 2.2: Schematic diagram of cutting path: (a) Path I for a uniform CFE length and (b) Path II for CFE arrays with custom electrode lengths.

2.3.2 Adjusting laser focus on a carbon fiber tip

When the power of the visible laser beam was sufficiently low, the carbon fiber could not be cut off and an oval-shaped light spot, as shown in Figure 2.3, was visible by the camera due to the reflection of the laser light on the Parylene C coating and the carbon fiber. In this study, 1.7 DCV was found to be the lowest input voltage for the laser to have a visible light spot and could not cut off the carbon fiber after focusing on it for over 5 minutes, which was long enough to focus the laser center of focal spot at point O based on the following three steps. In Step 1, linear stages x and y were moved to find the largest light spot on the carbon fiber with point O at the tip. The center of the focal spot was moved to $x = 0$. In Step 2, the linear stage z was adjusted vertically to find the smallest light spot size on the carbon fiber. The center of the focal spot was at $z = 0$. In Step 3, the linear stage y was moved until the length of the light spot in y-direction was equal to half of that in Step 2. The center of the focal spot was moved to $y = 0$ and aligned with point O.

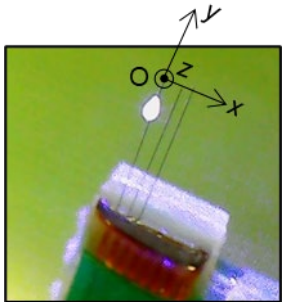


Figure 2.3: The light spot on the CF when the laser beam hit the CF.

2.3.3 CFE cutoff and sharpening

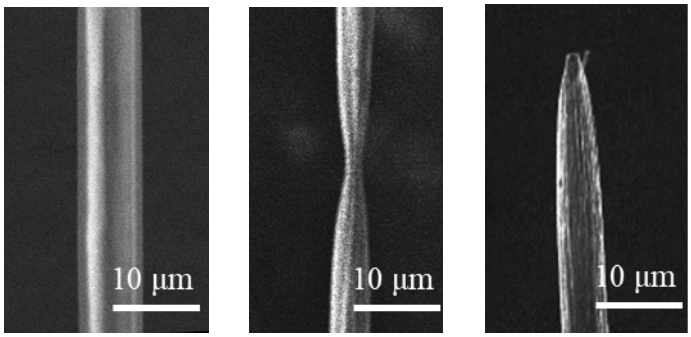
The laser moved transversely across the carbon fiber in the x-direction with its power on during cutting and sharpening. Along the y-direction, the laser was moved without power on. Linear stage z remained stationary so that the laser focal spot stays in the plane $z = 0$.

2.4 Experimental investigation of the laser speed, input voltage, and fabrication of CFE array with custom electrode lengths

Three experiments, marked as Exps. I, II, and III, were conducted to study the effects of laser speed and input voltage on the sharpness and stripped length of Parylene C coated carbon fiber tips.

Exp. I identified the maximum allowable speed for the cutoff of all four carbon fibers in an array under three laser input voltage levels (2.5, 4.0, and 5.0 DCV) using Path I. A minimal thermal energy accumulation from laser is needed for the carbon fiber cutoff. Thus, there exists a maximum allowed speed under each laser input voltage level, CF cannot be fully cut off if the speed exceeds the limit, as shown in Figure 2.4. During laser cutting, the thermoplastic Parylene C insulation on carbon fiber is partially removed. The exposed surface area affects the microelectrode impedance, which is crucial for single neuron activity recording. An electrode is defined to be functional if its 1 kHz impedance is lower than 4 MΩ [6]. Carbon fiber microelectrodes with small exposed surface area would yield high impedance (e.g. 3.9 MΩ at 1kHz for carbon fiber with 257 μm^2 exposed area in [7]) close to the 4 MΩ upper limit. A large exposed surface area leads to lower impedance but will reduce the electrode's sensitivity to single unit spikes [6,7]. In this preliminary study, the laser cutting generates a stripped length over 100 μm and an exposed area over 2000 μm^2, which is larger than the approximately 700 μm^2 exposed area generated by the current torch burning approach [6]. Thus, it is preferred for the laser cutting to be operated at or near the maximum allowed speed to enable the cutoff of Parylene C coated carbon fiber with minimal Parylene C stripping. Under 5 DCV laser input voltage, Exp. I started with the laser moving in the *x*-direction at 30 μm/s. This speed was decreased by the 2 μm/s increment until the speed with all four carbon fibers were cut off.

Another test was carried out with the speed increased by 1 μm/s. The larger speed of these two with the cutoff of all four carbon fibers was selected for 5 DCV. This procedure was repeated in tests at 4.0 and 2.5 DCV to find the laser speed enabling the cutoff of all four carbon fibers.

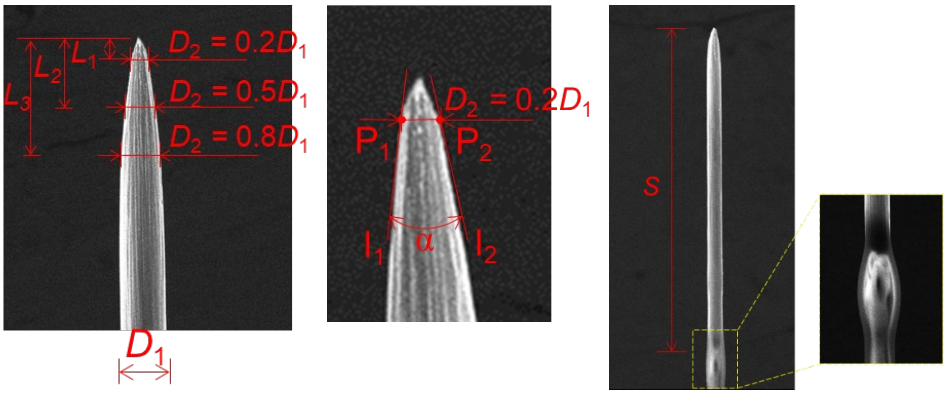


(a) (b) (c)

Figure 2.4: Scanning electron microscope (SEM) pictures of the carbon fiber with Parylene C insulation: (a) before cutting, (b) partially cut off at 25 μm/s and 4 DCV laser input voltage and (c) fully cut off with sharpened conical tip at 20 μm/s and 4 DCV laser input voltage.

The largest allowable speed under each voltage found in Exp. I was utilized in Exp. II to study the effects of the laser input voltage on carbon fiber tip sharpness and stripped length of Parylene C. For each laser input voltage, one cut across four carbon fibers using Path I was carried out based on the speed and laser input voltage identified in Exp. I. Micrographs of carbon fiber tips were acquired with the scanning electron microscope (SEM) (JSM-IT500HR by JEOL, Tokyo, Japan). Using the Fiji image processing package [47] in ImageJ (v.1.52r) [48], the tip profile, tip angle, and Parylene C stripped length were measured based on SEM micrographs of carbon fiber tips. The diameter of bare carbon fiber without Parylene C coating is denoted as D_1, as shown in Figure 2.5(a). In this study, D_1 was 6.8 μm. The diameter of the sharpened carbon fiber at different axial positions on the carbon fiber tip was denoted as D_2 in Figure 2.5 (a). The conical tip profile was characterized by three axial distances, denoted as L_1, L_2, and L_3, between the tip and the positions corresponding to D_2 of $0.2D_1$, $0.5D_1$, and $0.8D_1$, respectively.

For a conical carbon fiber tip, the tip angle α was measured as illustrated in Figure 2.5 (b). Two points P_1 and P_2 on the tip profile where $D_2 = 0.2D_1$ were identified. At P_1 and P_2, two lines l_1 and l_2 tangent to the tip profile were generated. The angle between l_1 and l_2 is the carbon fiber tip angle α. The stripped length S was defined as the distance from the carbon fiber tip to the end of the stripped region of Parylene C, as shown in Figure 2.5 (c).



(a) (b) (c)

Figure 2.5: Evaluation metrics for (a) tip profile L_1, L_2, and L_3: the distances between tip and the positions which correspond to $D_2 = 0.2D_1$, $0.5D_1$, and $0.8D_1$, (b) tip angle α, and (c) stripped length S: the distance from the tip to the end of the stripped region.

To ensure the function of laser sharpened CFEs, the electrochemical impedance spectroscopy (EIS) test and in-vivo recording with rats were performed. During EIS, the array of four carbon fibers with the sharpest tip in Exp. II was submerged 1 mm in the 1X phosphate buffered saline (PBS) (BP3994 by Fisher, Waltham, MA) along with an Ag|AgCl reference electrode (RE-5B by BASi, West Lafayette, IN) and a stainless steel counter electrode [7]. Signals with 10 μV_{RMS} amplitude at frequency ranging from 10 Hz to 31 kHz were utilized during the EIS measurement. The impedance of the carbon fiber electrodes at 1 kHz frequency, commonly used as the evaluation criterion in neuroscience [6,7,39], was recorded. Exposure area was measured by reconstructing axisymmetric 3D models of the sharp electrodes according to

their SEM images in computer-aided design software (Solidworks 2019 by Dassault Systèmes, Waltham, MA). Acute in-vivo recordings were taken from a Long Evans rat acutely implanted with an array of 4 laser cut and PEDOT:pTS treated fibers to demonstrate the viability of this sharpening method [49].

Exp. III investigated the fabrication of a CFE array with custom electrode lengths using Path II based on the laser input voltage and speed with the sharpest tip in Exp. II.

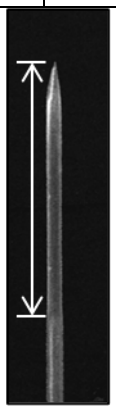
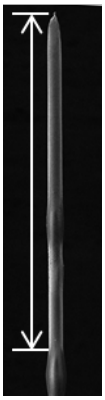
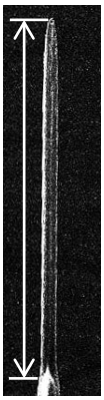
2.5 Results and discussions

Results of Exp. I laser cutoff speed are summarized in Section 2.5.1. Results of Exp. II, including tip angle and profile, insulation stripped length, impedance, and in-vivo recording, are presented and discussed in Sections 2.5.2, 2.5.3, and 2.5.4, respectively. The CFE array with different electrode lengths in Exp. III is illustrated in Section 2.5.5.

2.5.1 Exp. I: Laser speed for cutting off carbon fibers

Results of Exp. I are summarized in Table 2.1. Under the 5 DCV laser input voltage (1.5 W output power), all four carbon fibers could be cut off in one pass at 25 μm/s laser speed. This speed dropped to 20 μm/s as the voltage decreased to 4 DCV. At 2.5 DCV, the speed was further reduced to 1 μm/s. It took about 150 s to cut off one carbon fiber under 1 μm/s laser speed. The time required for cut off with input voltage less than 2.5 DCV was longer than 150 s and not practical. Under a lower input voltage, the rise in carbon fiber temperature would be slower, a longer time was required for the carbon oxidation and carbon fiber cutoff, and a slower laser speed was required for cutoff.

Table 2.1: Carbon fiber cutoff speed, tip profile, tip angle, and stripped length results under three laser input voltages

Input Voltage (V)	5		4		2.5	
Speed (μm/s)	25		20		1	
	Mean	SD*	Mean	SD*	Mean	SD*
Tip Profile L_1 (μm)	1.3	0.1	0.5	0.5	N/A	N/A
Tip Profile L_2 (μm)	5.3	0.4	5.8	2.7	3.3	2.6
Tip Profile L_3 (μm)	14.6	2.2	11.3	3.3	10.6	0.9
Tip Angle α (°)	27.9	1.7	41.4	13.8	N/A	N/A
Stripped Length S (μm)	122.5	10.4	177.3	11.4	195.3	14.1
SEM Images of Stripped Section	 50 μm		 50 μm		 50 μm	

* SD = Standard deviation

2.5.2 Exp. II: Tip angle and profile

Conically sharp caron fiber tips were achieved with 5.0 and 4.0 DCV laser input voltages, as shown in SEM images in Figures 2.6 (a) and (b). For the 2.5 DCV input voltage, serrated asymmetric carbon fiber tips were observed. As shown in Figure 2.6(c), only two of the four tips had a conically sharp tip. The L_1, L_2, L_3, and tip angle α (defined in Figure 2.5) of conical sharp tips from 5.0 and 4.0 DCV was quantitatively evaluated and results are summarized in Figure 2.7 and Table 2.1. Cutting at the highest laser power (1.5 W at 5.0 DCV input) gave a sharper

conical tip with a longer average L_1 of 1.3 μm and L_3 of 14.6 μm and a smaller average tip angle of 27.9°. As the laser input voltage decreased to 4.0 DCV (cutting at 20 μm/s), L_1 and L_3 were shortened to 0.5 μm and 11.3 μm, respectively, and the average tip angle was increased to 41.4°.

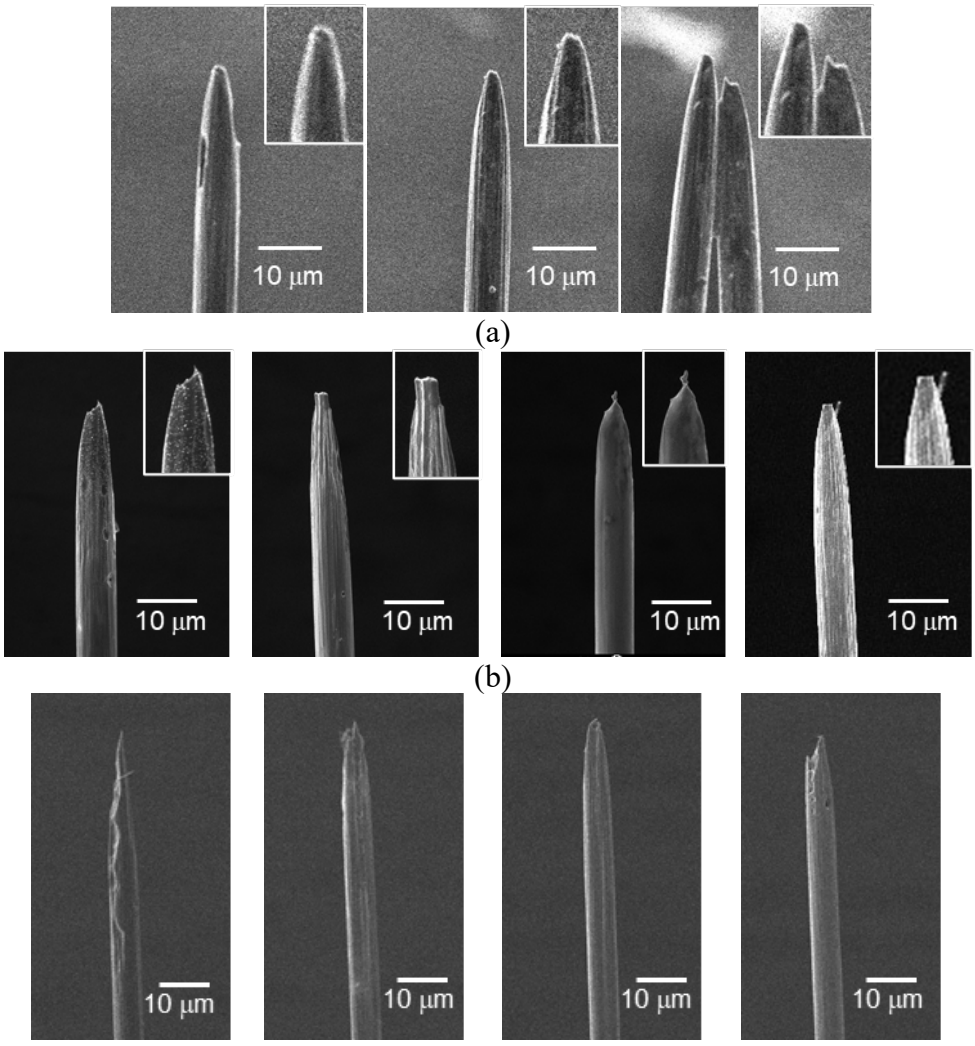


Figure 2.6: Four tips from (a) 5, (b) 4 and (c) 2.5 DCV input. Serrated asymmetric profiles were observed.

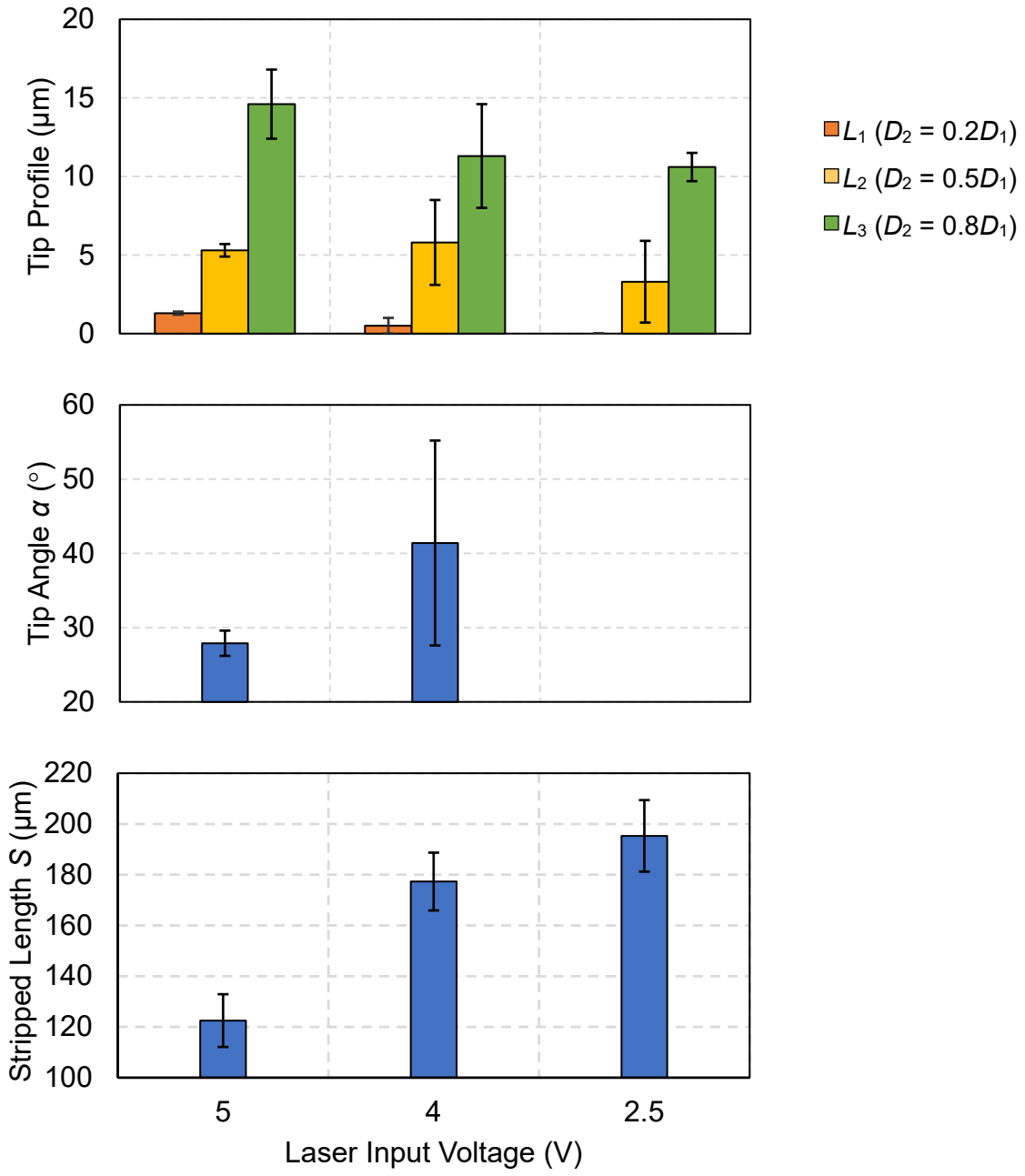


Figure 2.7: Tip geometry under three laser power levels: tip profile L_1, L_2, L_3, tip angle α and stripped length S.

Laser heating increased the temperature in carbon fibers, and the material removal was a result of carbon oxidation to carbon dioxide gas on the fiber surface at temperatures above 500°C [50]. When the laser moved across and the temperature dropped below 500°C, the material

removal stopped. The carbon fiber had a large surface to volume ratio and low thermal conductivity of 14 W/(m·K) [29]. Under laser heating, the carbon material near the laser focal point had higher heat flux and resulted in higher temperature and oxidation rate. The oxidation generated a reduced diameter section on the fiber as shown in Figure 2.4(b). This section had a larger specific surface area (inversely proportional to the diameter) compared to regions away from the laser cutting path, leading to a larger contact area between carbon material and oxygen in the air. The larger specific surface area and more heat flux from laser per unit volume further expedited the oxidation and material removal rate for carbon material near the forming tip and progressively generated a conical sharp tip geometry.

At a high laser input voltage and cutting speed, a shorter heat exposure time decreased the amount of heat conducted to the carbon fiber and created an uneven amount of carbon oxidation along the radial direction, leading to less material removal and a longer and sharper tip. In contrast, at lower laser input voltage and slower speed, less heat was conducted along the radial and axial directions of the carbon fiber, causing less axisymmetric carbon oxidation over a longer chemical reaction time and resulting less sharp tip at 4.0 DCV and 20 μm/s and non-conical shape at 2.5 DCV and 1 μm/s).

The variation in tip angle and profile of four carbon fibers under the same input voltage was mainly due to the difference in the *z*-direction height of carbon fibers in the CFE array assembly. The laser beam intensity will be higher at the center of laser focal spot. Therefore, the temperature in the carbon fiber would be higher at positions near the focal spot center, resulting in a faster oxidation rate [50] and a sharper carbon fiber tip. It was also observed that higher laser input voltage cutting at high speed leads to less deviations in tip geometry, yielding the standard deviation of 0.1 μm in L_1, 0.4 μm in L_2, 2.2 μm in L_3, and 1.7° in α when cutting with 5.0 DCV at

25 μm/s. The standard deviation increased to 0.5 μm, 2.7 μm, 3.3 μm and 13.8° for L_1, L_2, L_3, and α, respectively, during the laser cutting and sharpening of carbon fiber with decreased 4.0 DCV input and 20 μm/s speed.

2.5.3 Exp. II: Stripped length of Parylene C insulation

Results of the stripped length S at the maximum cutting speed under different laser input voltage levels are shown in Table 2.1 and Figure 2.7. The highest laser power 1.5 W resulted in the shortest average stripped length of 122.5 μm. The stripped length increased as the laser power (or input voltage) decreased. As the speed decreased, the laser heated the carbon fiber for a longer time. The temperature of a larger surface area on the carbon fiber reached the Parylene C melting point, resulting in a longer stripped length. The standard deviation in stripped length also increased from 10.4 μm to 14.1 μm as the laser input voltage decreased from 5 to 2.5 DCV.

In brain recording, a sharp tip with short stripped length (small surface area of recording site) is preferred for a low insertion force [31,45] and accurate recording of single neuron activities [6,7]. Sharpening with high laser power at the maximum allowable speed is preferred. Also, a short laser-carbon fiber interaction duration reduces the variation in sharpness caused by the variation of carbon fiber z-direction height.

2.5.4 Exp. II: Impedance of laser sharpened carbon fiber electrodes and in-vivo recordings

The impedance of Parylene C coated carbon fibers after laser sharpening and insulation removal was evaluated as a functionality test. Carbon fiber electrodes sharpened with a laser beam (1.5 W power and 25 μm/s speed) have an average 1 kHz impedance of 460 ± 225 kΩ (mean ± standard deviation), which is significantly lower than that of traditional steel scissor cut carbon fibers (6.7 ± 3.3 MΩ) [7] or torch burning carbon fibers (1.2 ± 1.3 MΩ) [6]. While low

impedance of the laser sharpened carbon fibers was partially due to the larger exposed area (2433 μm^2), compared to that of 629 μm^2 for torch burning [6]. The laser sharpening of carbon fiber electrodes is a highly controllable method and could be further investigated to optimize the balance between insulation stripping and impedance.

Acute recordings from four laser sharpened CFEs that were simultaneously implanted in rat motor cortex (n=1) are presented in Figure 2.8. For each of the four fibers, spikes from three units were found, suggesting that the laser sharpened CFEs are functional in recording neural units.

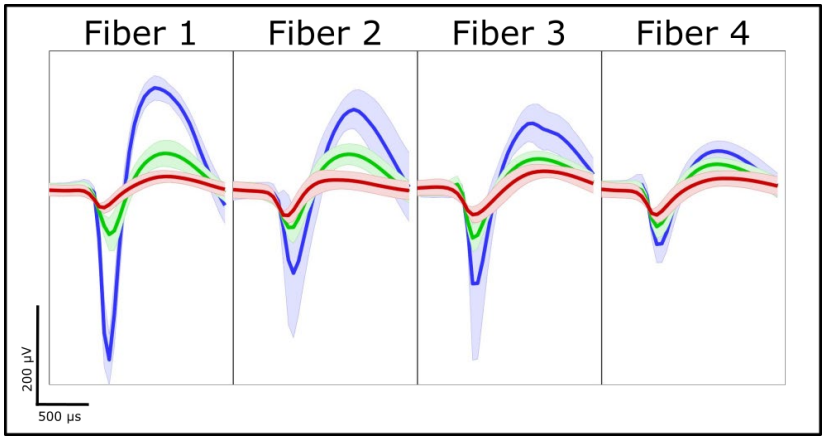
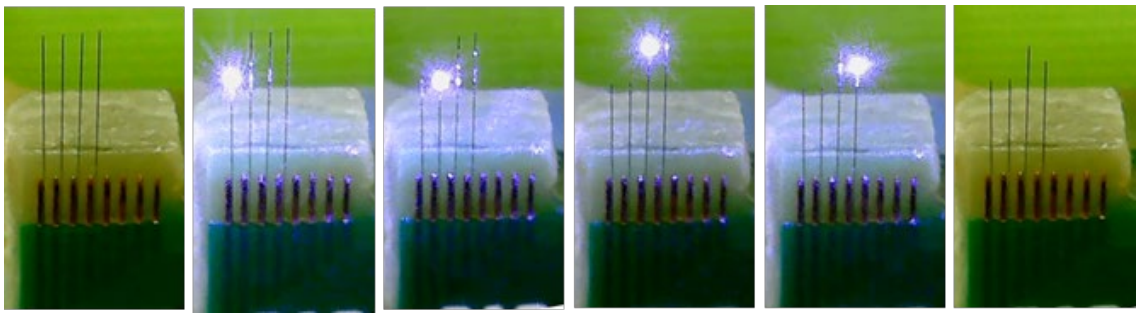


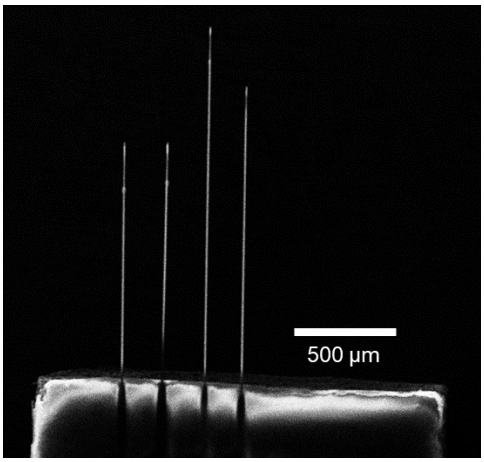
Figure 2.8: Acute electrophysiological spiking data from four laser sharpened CFEs [49].

2.5.5 Exp. III: Fabrication of an array with custom electrode lengths

As described in Figure 2.2(b), the fabrication of an array with different carbon fiber lengths using Path II was conducted under 1.5 W laser power at 25 µm/s speed. As shown in Figure 2.9(a), the laser moved along a staircase path from left to right. The carbon fiber array with defined electrode lengths was fabricated in one-pass of laser cutting. As shown in Figure 2.9(b), the array has custom electrode lengths and exposed carbon fiber tips.



(a)



(b)

Figure 2.9: Exp. III results: (a) snapshots of ongoing cutting and sharpening process to get an array of carbon fiber in different lengths (with l_1 = 1.2 mm, l_2 = 1.2 mm, l_3 = 1.6 mm, and l_4 = 1.4 mm in Figure 2.2) and (b) SEM image of the array.

2.6 Conclusions

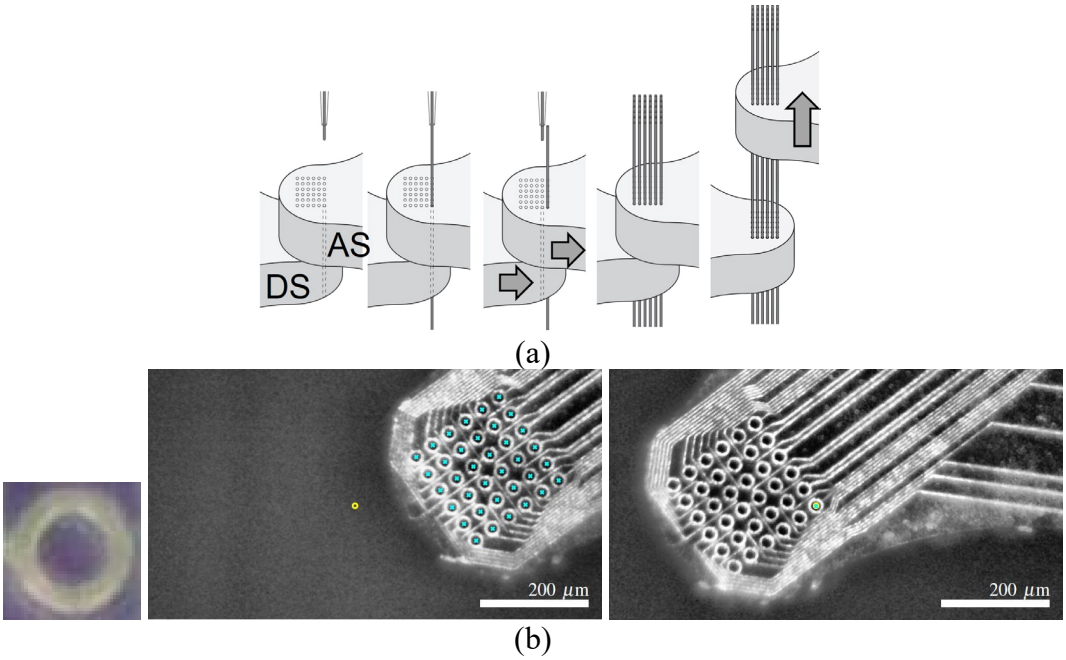
A new sharpening method for CFEs based on a moving laser beam was developed and tested. Results showed that the newly developed method enabled efficient sharpening of CFE arrays with custom electrode lengths. To achieve a sharper tip with minimal insulation layer stripped, a high-power laser at maximum allowable speed is preferred. This overcomes a key barrier in manufacturing pre-assembled CFE arrays by using the laser for non-contact sharpening with repeatable shapes.

Chapter 3 Algorithms for Automatic HDCF Array Assembly

The manual assembly of CFE arrays is labor-intensive, time-consuming, and limited by the accuracy and repeatability of the operator. Two difficulties in the fabrication of CFE arrays are 1) the alignment of CFE with other array components and 2) the observation and monitoring of the process. To overcome these problems, Massey et al. [39,51] proposed an automated micro-assembly method to build a 32-channel CFE array with 32 μm pitch as shown in Figure 3.1. Two silicon-based microfabricated substrates, namely device and alignment substrates, were precisely aligned and stacked with micro-positioners, forming 32 holes filled with conductive silver ink and epoxy. CF was extruded from a roller-based extruder. An image detection algorithm was used to align and insert each CF into corresponding hole. CFs inserted in holes were aligned vertically to the substrates by raising the assistive substrate and then fixed inside holes by silver ink and epoxy curing. An array with a small pitch distance and high assembly accuracy was achieved after removing the assistive substrate. This machine demonstrated the feasibility of using image processing techniques for alignment between centers of CF circular bottom surfaces and device substrate holes. However, there is a practical problem with 2.5 to 3 mm of CFE length based on this approach because the long unsupported length of CFE would lead to buckling during implantation.

In this chapter, a high density carbon fiber (HDCF) array with a silicon support structure for deep insertion is introduced and its assembly procedure is elaborated. The key step in the assembly of HDCF is the precise placement of CFEs. Two algorithms for imaging processing are

developed to align the orientation and position of CFE for the automatic assembly of HDCF. The lengths of the CFE can go up to 9 mm with this HDCF array configuration [42].



(a)

(b)

Figure 3.1: (a) CFE parallelization mechanism with the device and assistive substrates and (b) CF-hole alignment algorithm: the image of a hole as a template, automatically detected hole positions (teal) and tagged CF positions (yellow) before alignment, and CF alignment with the hole after moving substrates [39,51].

3.1 HDCF array and its components

As shown in Figure 3.2(a), the targeted HDCF array for assembly automation was composed of a connector (A79040-001 by Omnetics, Minneapolis, MN), a custom PCB, a silicon support structure (SSS), and 16 CFEs. The connector had standardized pins for back-end electrical connection to pre-amplifiers. SSS was fabricated with the six-step cleanroom procedure introduced in [42] as shown in Figure 3.3. The SSS, as shown in Figure 3.2 (b), provided physical and electrical connections between CFEs and custom PCB and had four components: 1) silicon base and shanks, 2) bond pads to PCB, 3) gold traces, and 4) gold pads, as well as two indented features: 1) silver epoxy wells beneath each gold pad and 2) trenches

along the middle line of each shank. The length and density of CFE in HDCF array were pre-determined by the length and pitch of the shanks. In this study, the shanks were 3 mm long and the pitch was 80 μm. CFEs extended about 3.5 mm from the silver epoxy wells and formed an array with 80 μm spacing.

During assembly of HDCF array, the CFEs were placed on the top of gold pads, laid in the trenches and supported by the shanks in the SSS. Each CFE overhangs by about 0.3 mm beyond the end of the shank trenches, as shown in Figures 3.2 (a) and (c), and had non-insulated recording sites at the free end tips. The CFEs and shanks of SSS were implanted together, providing a minimally invasive solution for the deep insertion of CFE into recording sites. The rigidity of SSS ensured the successful insertion of CFEs. The minimal invasiveness was a result of the small 15 μm by 15 μm cross-sectional area of the CFE and the shank (Figures 3.2(b) and (c)) [42].

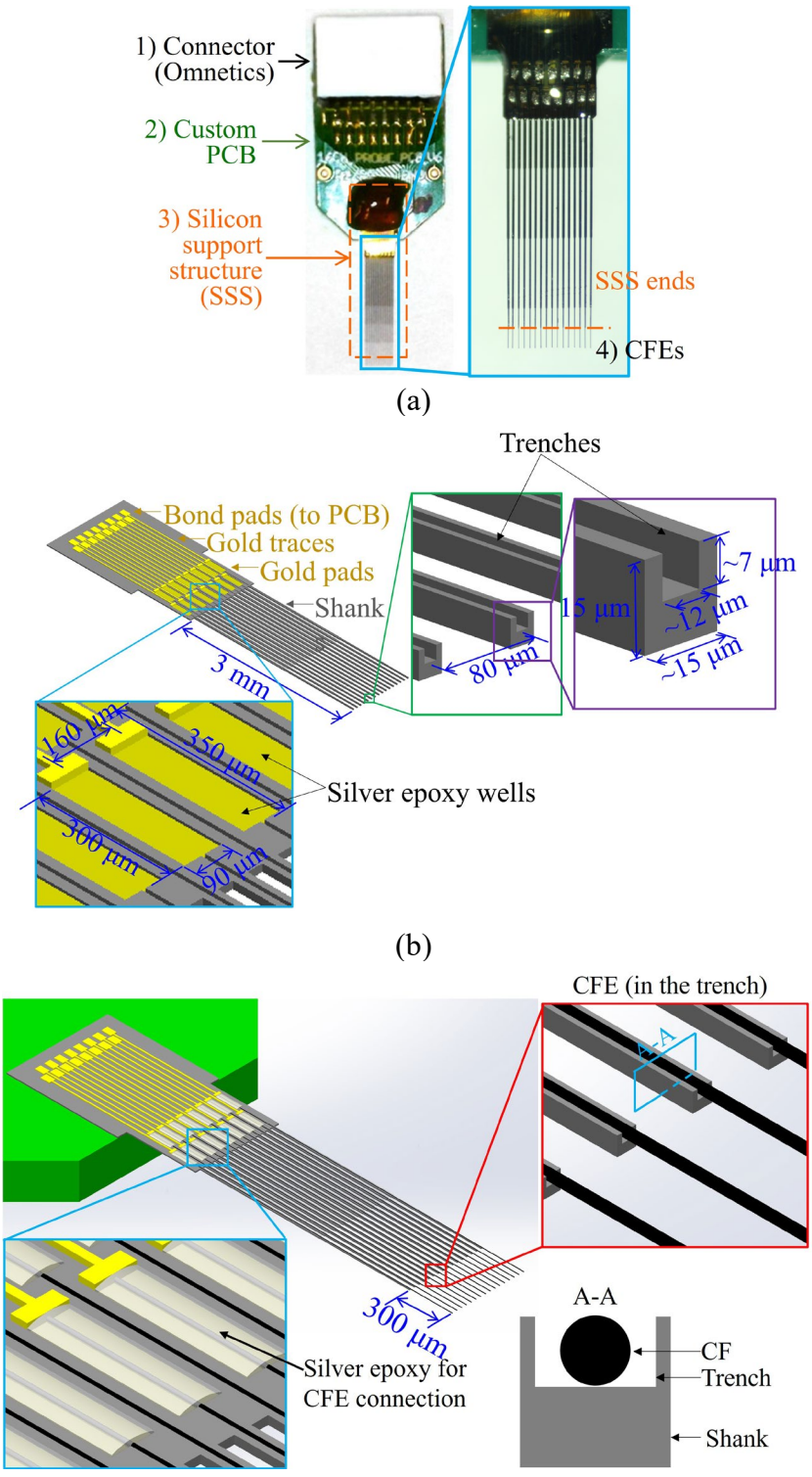


Figure 3.2: (a) HDCF array components: connector, custom PCB, SSS, and CFEs, (b) SSS components, features, and dimensions, and (c) CFEs started from the silver epoxy wells and overhangs from the trenches.

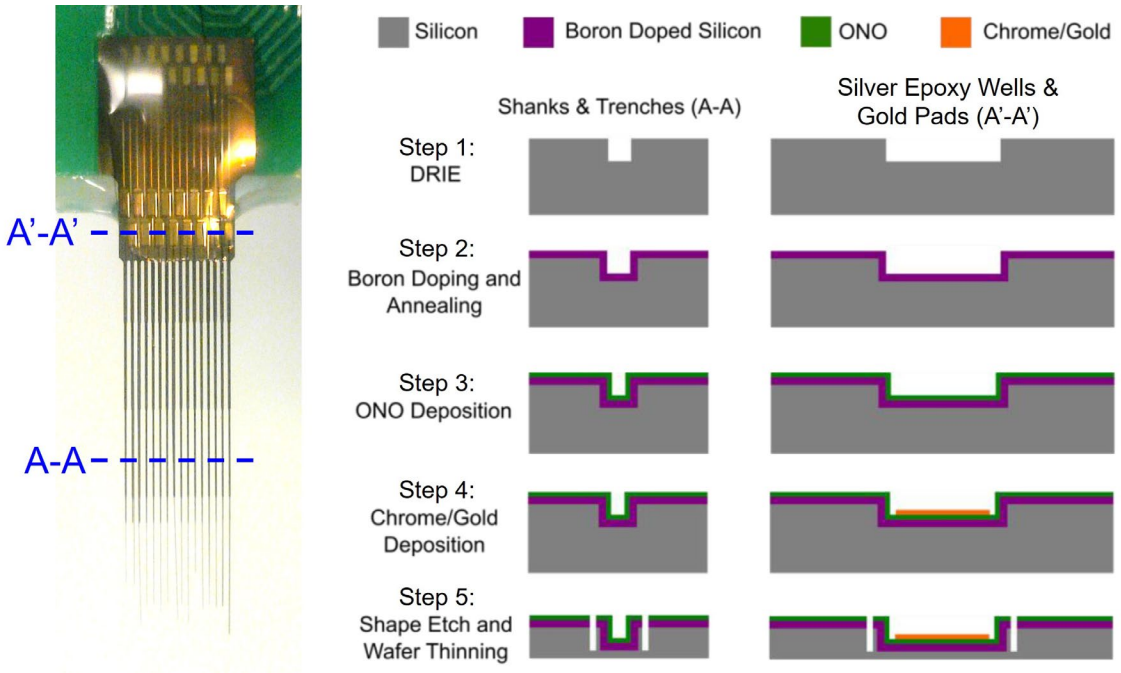


Figure 3.3: The SSS fabrication process: Cross-sectional diagram of the shanks and trenches region (A-A) and the silver epoxy wells and gold pads region (A'-A').

3.2 HDCF array assembly procedure

Seven steps were taken to assemble an HDCF array, as illustrated in Figure 3.5(a).

- Step 1 Connection of connector, PCB, and SSS. The connector, PCB, and SSS were connected physically and electrically as shown in Figure 3.5(b). The connector was soldered to the PCB and its pins were covered with two-part epoxy (Sy-SS, Super Glue Corporation, Ontario, CA). The silicon support structure was attached to the PCB with epoxy (301, Epoxy Technology, Billerica, MA) after curing at 140℃ for 20 minutes and further supported by applying two-part epoxy (Sy-SS, Super Glue Corporation, Ontario, CA) underside the overhanging portion containing gold pads and shanks. The gold pads on the PCB and bond pads on the silicon support structure were connected through wire bonding.

- Step 2 CF loading. A CF section (about 6 cm in length) was loaded onto the roller-based extruder which will be introduced in Section 4.1.1.
- Step 3 CFE population. 16 CFEs were placed in silver epoxy wells and trenches with the HDCF array assembly machine. Details of the machine and the process will be illustrated in Chapter 4.
- Step 4 CFE electrical connection. Silver epoxy (H20E; Epoxy Technology, Billerica, MA) was deposited in silver epoxy wells by a desktop nanolithography system (NLP 2000, Advanced Creative Solutions Technology, Carlsbad, CA) and then cured at 140 ℃ for 20 minutes. CFEs were electrically connected to the SSS and PCB.
- Step 5 CFE physical reinforcement. Epoxy (NOA 61, Norland Products, Cranbury, NJ) was applied on the gold pad area and along the shanks and UV cured to physically reinforce the connection between CFEs and the SSS.
- Step 6 Device insulation. The HDCF array was coated with approximately 800 nm of Parylene C (PDS 2035, Specialty Coating Systems, Indianapolis, IN) for insulation.
- Step 7 CFE functionalization. Overhang CFEs were laser cut to 300 μm using a 532nm Nd:YAG pulsed laser (LCS-1, New Wave Research, Fremont, CA; 5 mJ/pulse, 5 ns pulse duration), plasma treated using a Glen 1000P Plasma Cleaner (pressure 200 mT, power 300 W, time 120 s, oxygen flow rate 60 sccm, and argon flow rate 7 sccm), and coated with PEDOT:pTS as previously done in [5,8].

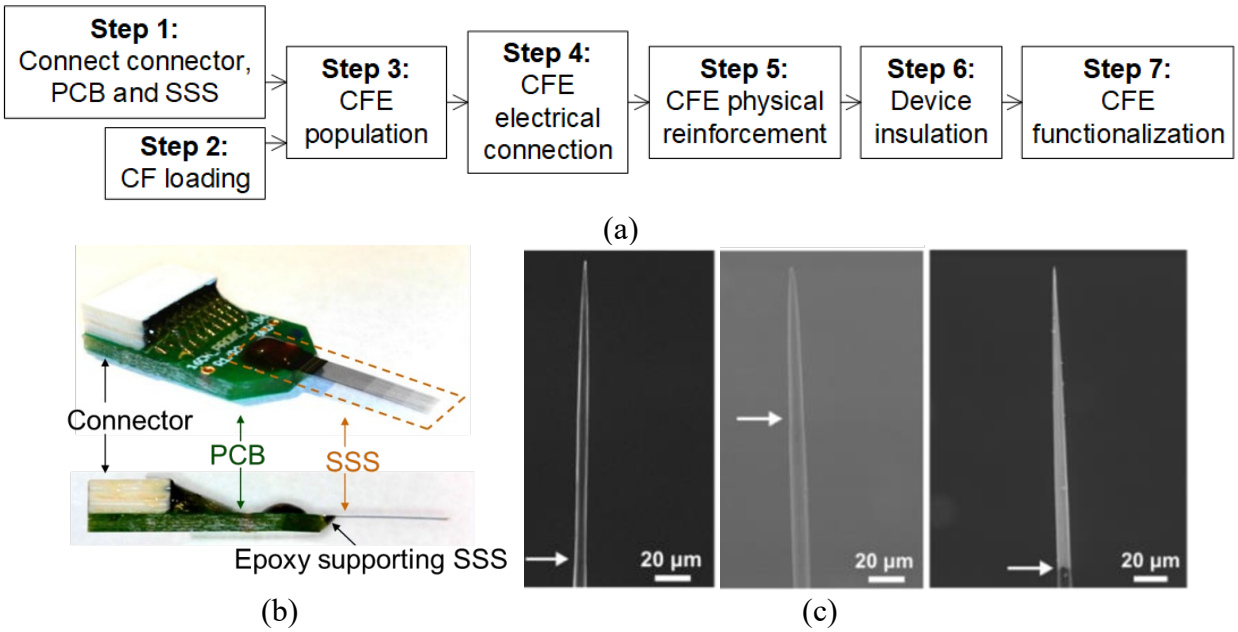


Figure 3.4: (a) Seven steps of HDCF array assembly, (b) the connector, PCB, and silicon support structure connected physically and electrically, and (c) SEM photos of CFE tip after sharpening, PEDOT:pTS coating, and PtIr coating (insulation above the arrow removed) [42].

Two algorithms were developed to achieve the automatic CFE population. To be placed precisely into the trench and silver epoxy well, the CFE needed to be aligned parallel with the shank first, then its tip should contact the center of a gold pad edge. Algorithm I measured the orientation of CF and shanks. Algorithm II calculated the distance between the CF tip and the desired edge center on gold pads where the tip would be placed. Both algorithms used the digital images taken from the top of the CF and the PCB as input. Details for Algorithms I and II are presented in Sections 3.3 and 3.4, respectively.

3.3 Algorithm I: CF-shank orientation alignment

The goal of Algorithm I was to measure the orientation of the shank and CF for their angular alignment.

3.3.1 Input and output variables

Two images used as input for Algorithm I were the image of the gold pad area and part of the shanks from camera #1 for measuring shank orientation β_1 and the image of the CF for measuring the CF orientation β_2. The CF and shanks were orientated diagonally as shown in Figure 3.6 to view a longer section of both. The output $\beta = \beta_2 - \beta_1$ was the difference between the two measured angles. The CF would be rotated by an angle β using the rotary stage in the motion system which will be introduced in Section 4.1.2 for the CF-shank alignment.



Figure 3.5: The measurement of β_1 and β_2. Green solid lines are the lines extracted from the image.

3.3.2 Orientation measurement

To measure the orientation of the shanks and the CF, the edge of the silicon support structure and the CF need to be extracted from the image in the following five steps.

- Step 1 Color normalization. The color image (marked as I0) from the camera is converted into a greyscale image I1 using MATLAB (R2020b, the MathWorks, Inc., Natick, MA). The RGB values of every pixel in I0 are weighed and transformed to a grayscale value. In this study, the weights are 0.299 for R, 0.587 for G, and 0.114 for B. All R, G, and B value in I0 range from 0 to 255. Every pixel in I1 has a grayscale value ranging from 0 to 255.

- Step 2 Background removal. The greyscale image I1 is converted to the binary image I2 by applying a black and white filter. In this study, the brightness threshold is 120. The bright background pixels with grayscale value larger than 120 are removed and assigned a zero value (black) in I2. The rest pixels are assigned a value of one (white) in I2.
- Step 3 Edge extraction. Edges in image I2 are extracted to a binary image I3 using MATLAB (R2020b, the MathWorks, Inc., Natick, MA). For β_1 measurement, edges of the rectangular gold pad area and comb-like shanks are extracted. For β_2 measurement, a single line of CF is extracted.
- Step 4 Line parameterization. Lines in I3 are parameterized through a Hough transform, which outputs a matrix $\boldsymbol{H}$ in the (r, θ) space [52]. Each element of the matrix $\boldsymbol{H}(r_0, \theta_0)$ denotes the number of pixels that are located on the line $r_0 = x\cos\theta_0 + y\sin\theta_0$, where r_0 is the distance from the origin to the closest point on the straight line, and θ_0 is the angle between the x-axis and the line connecting the origin with that closest point, as shown in Figure 3.7. The peak element (local maxima) of the matrix $\boldsymbol{H}$ is represented by $\boldsymbol{H}(r_p, \theta_p)$ and indicates that I3 contains the line $r_p = x\cos\theta_p + y\sin\theta_p$. Lines in I3 are parameterized.
- Step 5 Line selection and angle measurement. Peaks are selected from $\boldsymbol{H}$ as well as the corresponding θ_p. For β_1, five peaks and θ_ps are selected, and the median of the θ_ps (denoted as θ_m) is used to calculate β_1 with the formula $\beta_1 = \begin{cases} 90 - \theta_m & (\theta_m > 0) \\ -90 - \theta_m & (\theta_m < 0) \end{cases}$. For β_2, only one peak and θ_p need to be selected because there is only one line (CF) in I3, and β_2 can be calculated by $\beta_2 = \begin{cases} 90 - \theta_p & (\theta_p > 0) \\ -90 - \theta_p & (\theta_p < 0) \end{cases}$.

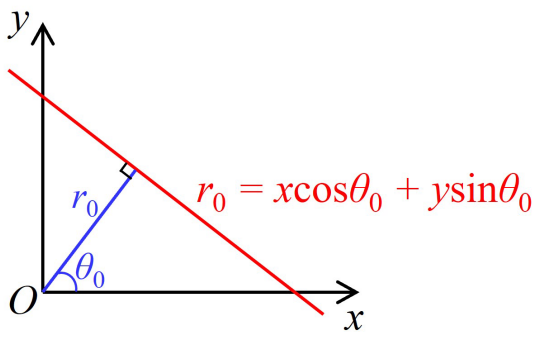


Figure 3.6: Each entry of $\boldsymbol{H}((r_0, \theta_0)$ represents the line $r_0 = x\cos\theta_0 + y\sin\theta_0$.

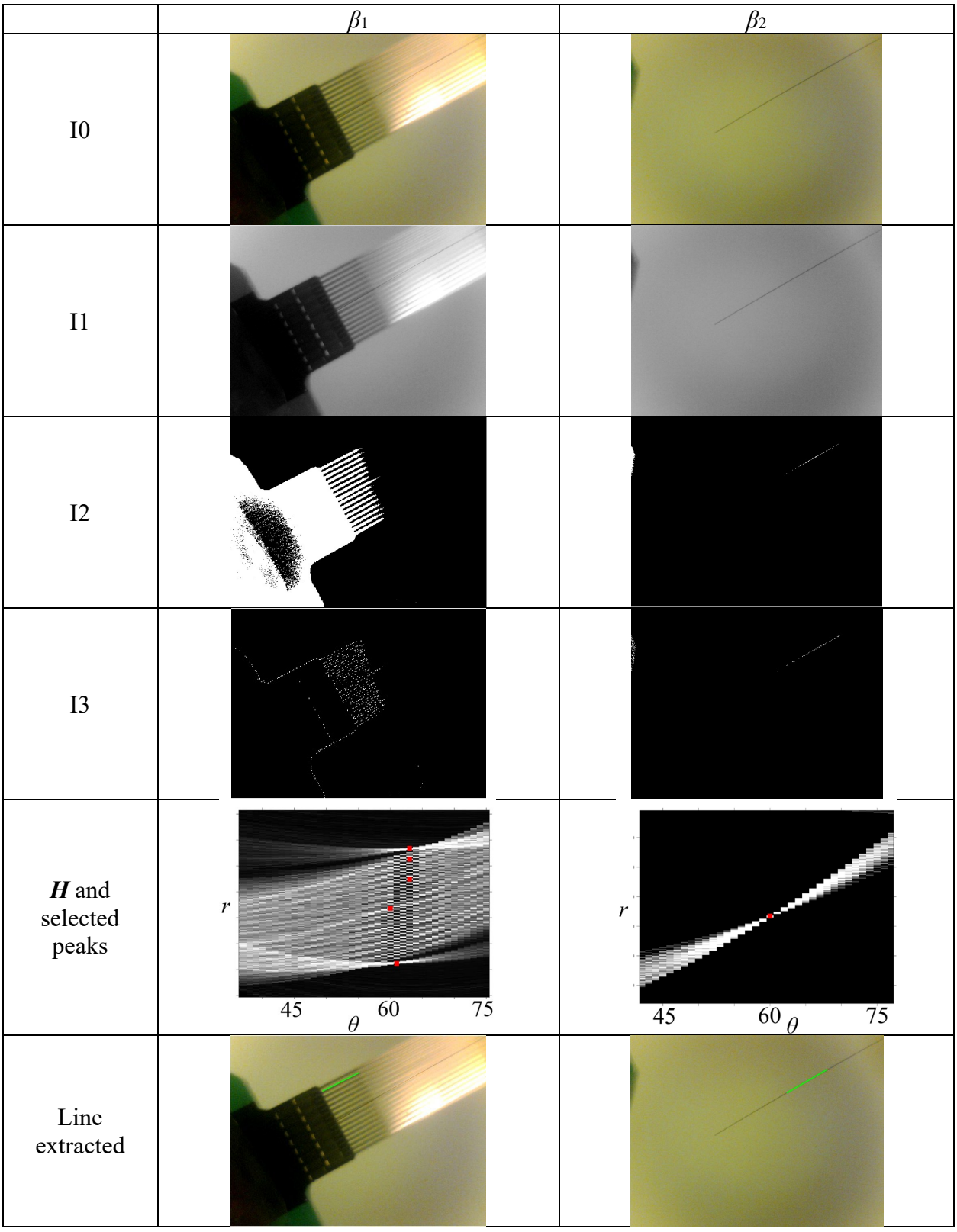


Figure 3.7: Measurement of β_1 and β_2 in Algorithm I.

3.4 Algorithm II: CF tip – gold pad edge center alignment

Algorithm II calculated the distance between the desired gold pad edge center position and the CF tip and decomposed it into *x*- and *y*-displacements in two orthogonal directions for the translational motion of the PCB.

3.4.1 Input and output variables

The input for Algorithm II was the digital image of the gold pad area and CF tip location. The CF tip pixel location was tagged manually as *O* (see Figure 3.9) and used as the origin for the Cartesian coordinate for the PCB translational motion. *O* remained still in the view during CF rotation and PCB translation because the camera was fixed with respect to the CF.

The output variables were the distances Δx and Δy, as shown in Figure 3.9, between the CF tip and the target (highlighted in yellow) in *x*- and *y*-directions, respectively. For each of the sixteen rectangular gold pads, the target was the middle point of the shorter edge away from the shanks. The CF tip would be aligned with the target and placed in the trench of SSS. In this way, when silver epoxy was deposited on the gold pads after CFE placements, a long section of CFE would be in contact with silver particles in the epoxy to ensure proper electrical connection.

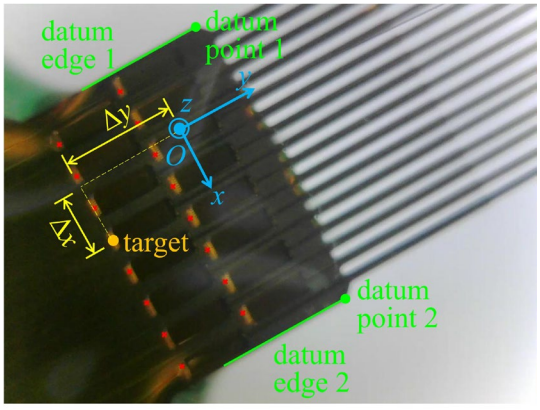


Figure 3.8: Algorithm II: inputs, outputs, and datum edges.

3.4.2 Datum edges extraction and distance calculation

To calculate Δx and Δy from the image, two mappings had to be constructed. These were 1) between the line orientation in the image and the directions for PCB translation and 2) between the pixel distance in the image and the distance in PCB translational motions. To build such connections, two datum edges, the upper and lower bounds of the gold pad area, and two datum points, the corners of the gold pad area, were extracted using MATLAB (R2020b, MathWorks, Natick, MA). The orientation of the datum edges in the image was mapped to the y-direction for PCB translation and the pixel distance was mapped to the width of the gold pad area. Positions of centers of the gold pad's edges could be calculated based on the datum edges, points, and design sketch of the silicon support structure. The pixel distance of the CF tip and target gold pad edge's center was first decoupled into x- and y-directions, then converted into distance Δx and Δy.

Datum edges and points are extracted in the following seven steps using MATLAB (R2020b, the MathWorks, Inc., Natick, MA) as shown in Figure 3.9.

- Step 1 Color normalization. The color image (marked as I0 in Figure 3.9(a)) from the camera is converted into a greyscale image I1 using the same method as in Step 1 of Algorithm I.
- Step 2 Background removal. The grayscale image I1 is converted to a binary image I2 by applying a black and white filter (as in Step 2 of Algorithm I) with a brightness threshold of b. In this study, $b = 75$.
- Step 3 Edge detection. Edges in I2 are extracted to a binary image I3. The edges of the rectangular gold pad area and some of the comb-like shanks are extracted.

- Step 4 Line parameterization. A Hough transform is applied to I3 and outputs a matrix $\boldsymbol{H}$ in the (r, θ) space. Lines in I3 are parameterized by entries of the peaks in $\boldsymbol{H}$ as in Step 4 of Algorithm I.
- Step 5 Datum edge candidates extraction. Peaks are selected from $\boldsymbol{H}$ and corresponding lines are recovered from the peaks with parameters (n, l_1, l_2), where n is the number of lines (default $n = 10$), l_1 is the maximum gap length which will be filled if the line is intermittent ($l_1 = 200$ pixels), and l_2 is the minimum length of the extracted lines ($l_2 = 40$ pixels). The extracted lines include the two boundaries of the gold pad area and edges of the shanks, as shown by the green solid lines in Figure 3.9(f).
- Step 6 Datum edge and datum points selection. The n extracted lines are sorted by their intersection, and lines with the maximal and minimal intersection would be the two datum edges. Their orientation is mapped to the y-direction in the coordinates. The starting points of the edges (the corners of the gold pad area) are the two datum points. Their pixel distance is used as the scale for pixel and physical length conversion.
- Step 7 Target position calculation and motion decoupling. The position of centers of gold pad edges is calculated based on the datum edges, points, and design sketch of the silicon support structure. The pixel distance of CF tip and target gold pad edge center is first decoupled into x- and y-directions, then converted into distance Δx and Δy.

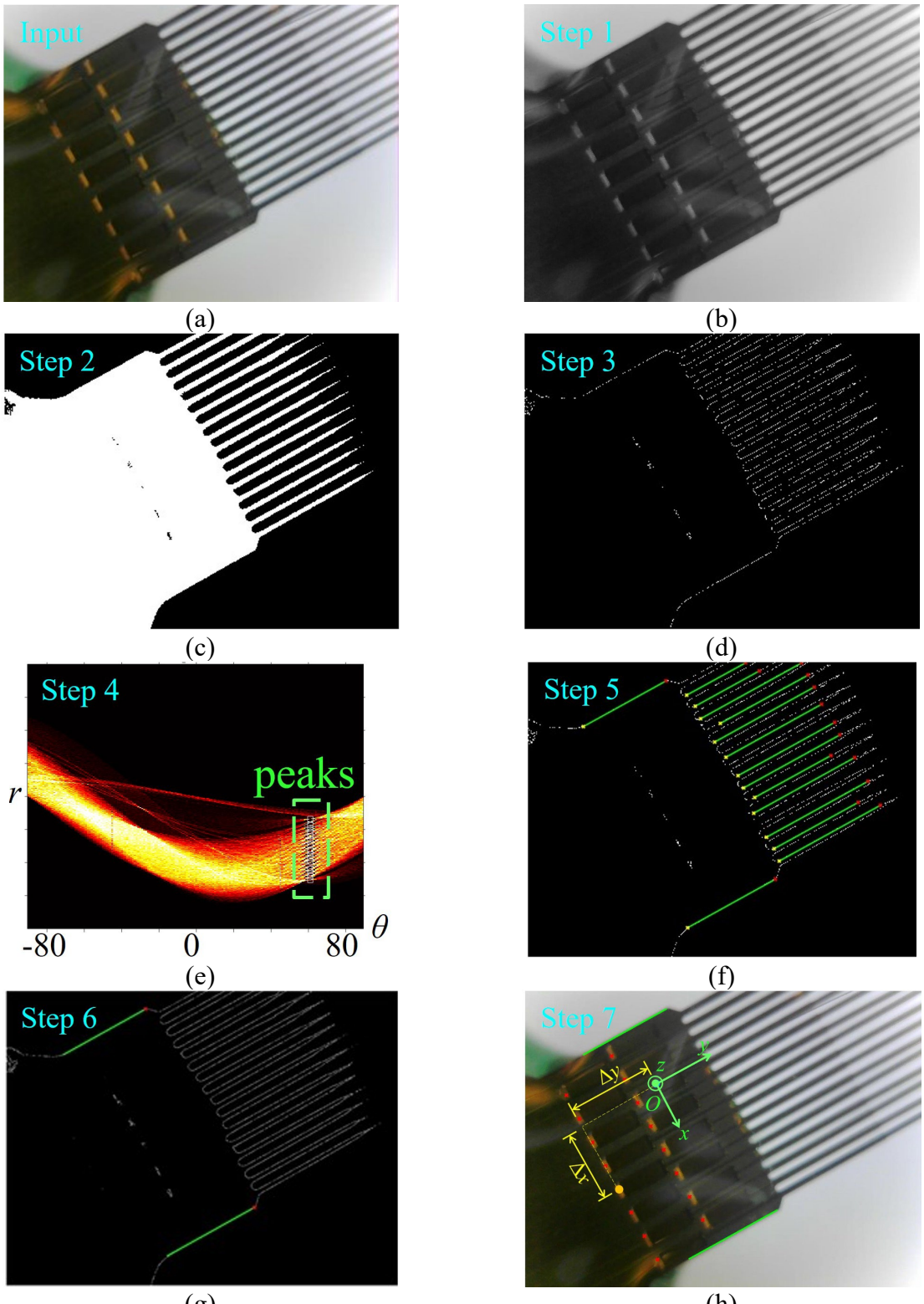


Figure 3.9: Algorithm II for Δx and Δy calculation: (a) Input I0, (b) Step 1 I1, (c) Step 2 I2, (d) Step 3 I3, (e) Step 4 $\boldsymbol{H}$ and peaks, (f) Step 5 n extracted lines, (g) Step 6 two datum edges (green) and datum points (red), and (h) Step 7 calculated gold pad edge centers (red), target edge center (yellow), Δx and Δy.

3.5 Experiments for Algorithms I and II performance evaluations

Two experiments, marked as Exps. I and II, were conducted to evaluate the performance of Algorithms I and II. Exp. I measured the angle between CF and the shank before and after Algorithm I execution to evaluate how well the CF could be aligned parallel to the silicon supports. Exp. II measured the error in CF tip location after Algorithm II application to evaluate how precise the machine could place the CF tip to the target point on the gold pad.

3.5.1 Exp. I: CF deviation angle reduction with Algorithm I application

We first evaluated how well the CF could be aligned parallel to the silicon supports. After aligning CFs using the apparatus, 15 sets of CF deviation angles (angle between the CF and the shank in the top view, denoted by θ_{xy} as shown in Figure 3.10) before and after Algorithm I execution were measured and compared. The θ_{xy} was measured three times with the Fiji image processing package [47] in ImageJ (v.1.52r). The average value of θ_{xy} before Algorithm I application was 1.16 ± 0.94 degrees (mean ± SD) and was reduced to 0.54 ± 0.51 degrees after the adjustment. The alignment in the orientation between CF and the shank is improved with the Algorithm I application.

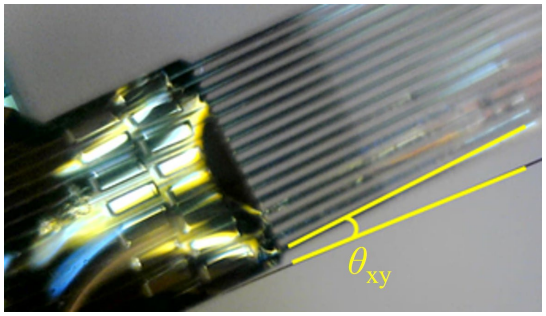
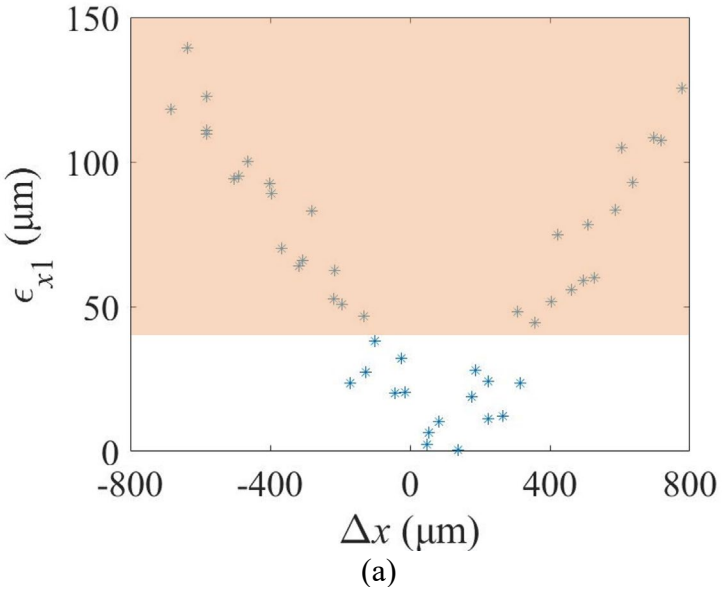


Figure 3.10: Definition of CF deviation angle θ_{xy}

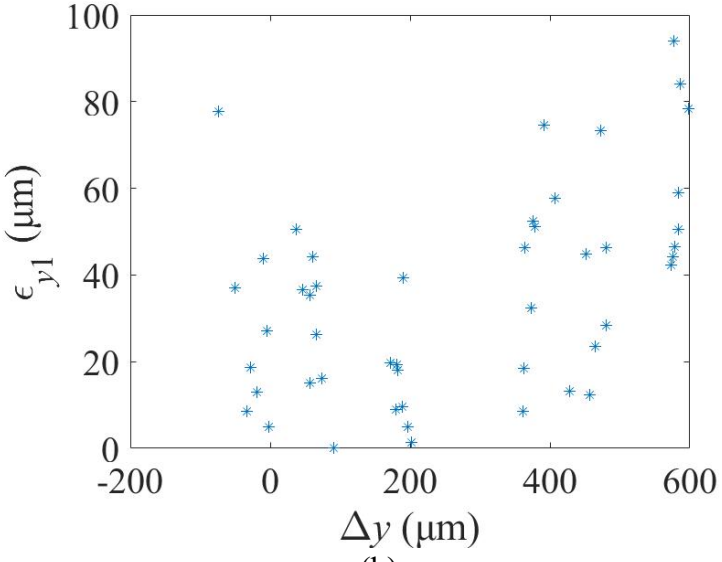
3.5.2 Exp. II: CF tip positioning accuracy using Algorithm II

We next evaluated how precise the machine could place the CF tip to the target point on the gold pad. CF tip positioning accuracy after applying Algorithm II was evaluated by measuring the distance (error) between the CF tip *O* and the target in *x*- and *y*- directions (denoted as ε_{x1} and ε_{y1}) after moving the PCB by Δx and Δy calculated by Algorithm II. A total number of 49 measurements were performed. The results of ε_{x1} vs. Δx and ε_{y1} vs. Δy are summarized in Figure 3.11. Due to image distortion further from the center, the error in tip position in the *x*-direction ε_{x1} increased as the absolute value of Δx increased. The ε_x larger than 40 μm would end up as a failed assembly because CF tip would be outside of the gold pad. The gold pad had a large dimension (300 μm) in the *y*-direction, the ε_{y1} ranging from 0 to 100 μm was tolerable.

After the first iteration using Algorithm II, the CF tip moved to a position closer to the center of the target gold pad with less image distortion. The Algorithm II was applied again based on positions from the first iteration. Errors were measured and denoted as ε_{x2} and ε_{y2}. The changes of ε_{x1} and ε_{x2} of the 49 measurements are summarized in Figure 3.12(a). For 46 out of the 49 cases, the error in the *x*-direction was reduced to less than 40 μm after the second iteration. For the three cases with ε_{x2} greater than 40 μm, a third iteration of Algorithm II was utilized and the CF tip was aligned within the gold pad with the error ε_{x3} all less than 30 μm. For HDCF machine operation, Algorithm II was operated 3 times.

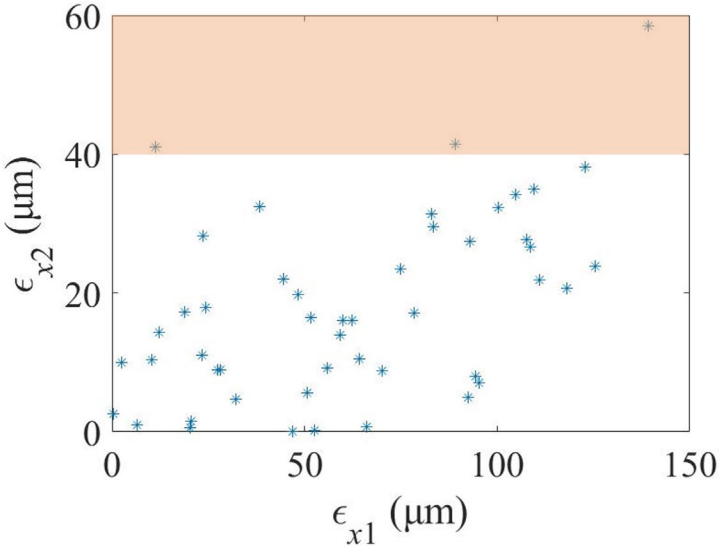


(a)

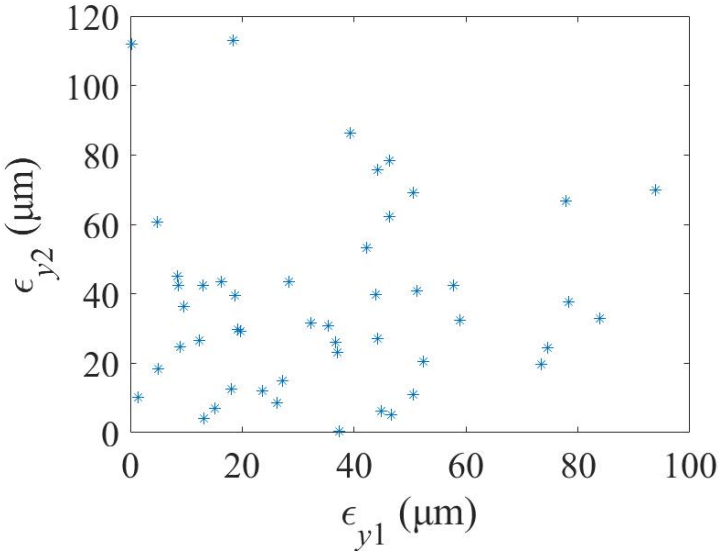


(b)

Figure 3.11: CF tip positioning accuracy in (a) *x*- and (b) *y*- directions after first iteration of Algorithm II. The failure area is shaded with ε_{x1} larger than 40 μm.



(a)



(b)

Figure 3.12: (a) ε_x after the first and second Algorithm II iterations (the failure area is shaded with ε_{x2} larger than 40 μm), and (b) ε_y of repeated Algorithm II application.

3.5.3 Parameter selection for Algorithm II

There are four parameters in Algorithm II: b, n, l_1, and l_2. b is the brightness threshold for the black and white filter in Step 2, n is the number of datum edge candidates extracted in Step 5, l_1 is the maximum gap length which will be filled if the line is intermittent (unit: pixel), and l_2 is the minimum length of the extracted lines (unit: pixel). The default (b, n, l_1, l_2) value (75, 10, 200, 40) is selected through trials and works for over 80% of the detection trials. All the failure cases can be fixed and achieve a successful detection by searching for (b, n) around the default value (75, 10) in two steps:

- Step1. Increase the value of b with an increment of 1 for every search, until a successful detection is achieved or b reaches 90.
- Step 2. Reset b to 75, decrease the value of n with an increment of -1 for every search, until a successful detection is achieved.

Figure 3.13 provides some cases where default (b, n) does not work but successful detections are achieved with the above searching strategy.

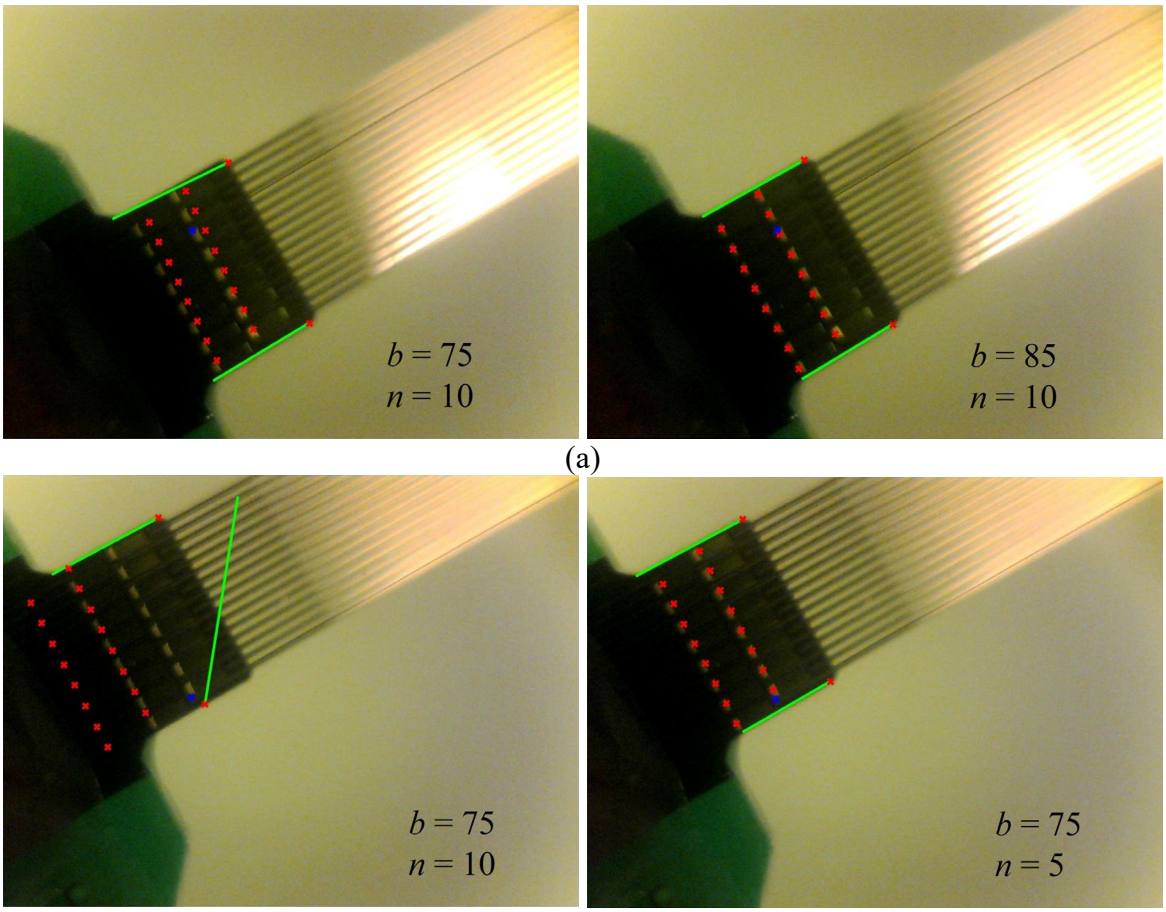


Figure 3.13: Cases not working with default (b, n) = (75, 10) and required parameter searching: (a) searching Step 1 applied, detection works when $b \in$ [83, 89], n = 10 and (b) searching Steps 1 and 2 applied, detection works when b = 75, $n \in$ [2, 6].

3.6 Conclusions

Two algorithms were developed to align the orientation of the CF with the shanks and the CF tip location with the desired edge center on gold pads. Parameters within the algorithm could be selected, manually or automatically adjusted following searching strategies, under different working conditions. The dedicated adjustments of the orientation of CF and the position of PCB could be visualized and quantified, which were essential for the high precision assembly of the HDCF array.

Chapter 4 High Density Carbon Fiber Array Assembly Machine

The carbon fiber (CF) is thin (7 μm), fragile, and difficult to handle manually. The shank of the silicon support structure (SSS) is small (3 mm by 0.015 mm by 0.015 mm as shown in Figure 3.1(a)) and brittle. The automatic high density carbon fiber (HDCF) assembly machine is developed to automate the population of carbon fiber electrodes (CFEs) on the narrow (12 μm) and shallow (12 μm) trenches (Figure 3.1(a)) in SSS. This machine requires sensitive visual-based detection, precise calculation from the image algorithms (in Chapter 3), and the hardware design demanding the: 1) precise (in the 1 μm level) and stable motions, 2) soft physical contact between CF and machine components, 3) compact spatial configuration in 5 mm by 2 mm by 2 mm space to complete the CFE assembly without interference among machine parts, and 4) motions of machine parts to be visualized, monitored, and recorded for safety and quality purposes.

In this chapter, the description of the HDCF assembly machine and three subsystem tests to study the 1) effect of Parylene C coating in the extruder capillaries, 2) CF extrusion accuracy of the extruder, and 3) effect of translational speed in the vertical direction on CF placement are presented. Two HDCF arrays were assembled. The assembled HDCF arrays were evaluated by impedance test and in-vivo recording from rat motor cortex.

4.1 Overview of the HDCF array assembly machine

The HDCF array assembly machine developed in this study is shown in Figure 4.1. It consisted of four subsystems: 1) a roller-based extruder for CF feeding, 2) a motion system for PCB translation and CF rotation, 3) an imaging system for motion trajectory planning and process monitoring, and 4) a laser cutter for CF cutoff. The Subsystems 1-4 are described in the following Sections 4.1.1 to 4.1.4. The controller and software platform applied to coordinate the subsystems are presented in Section 4.1.5. The target workpiece for the machine was the PCB with SSS, which was attached to the motion system by a 3D-printed fixture.

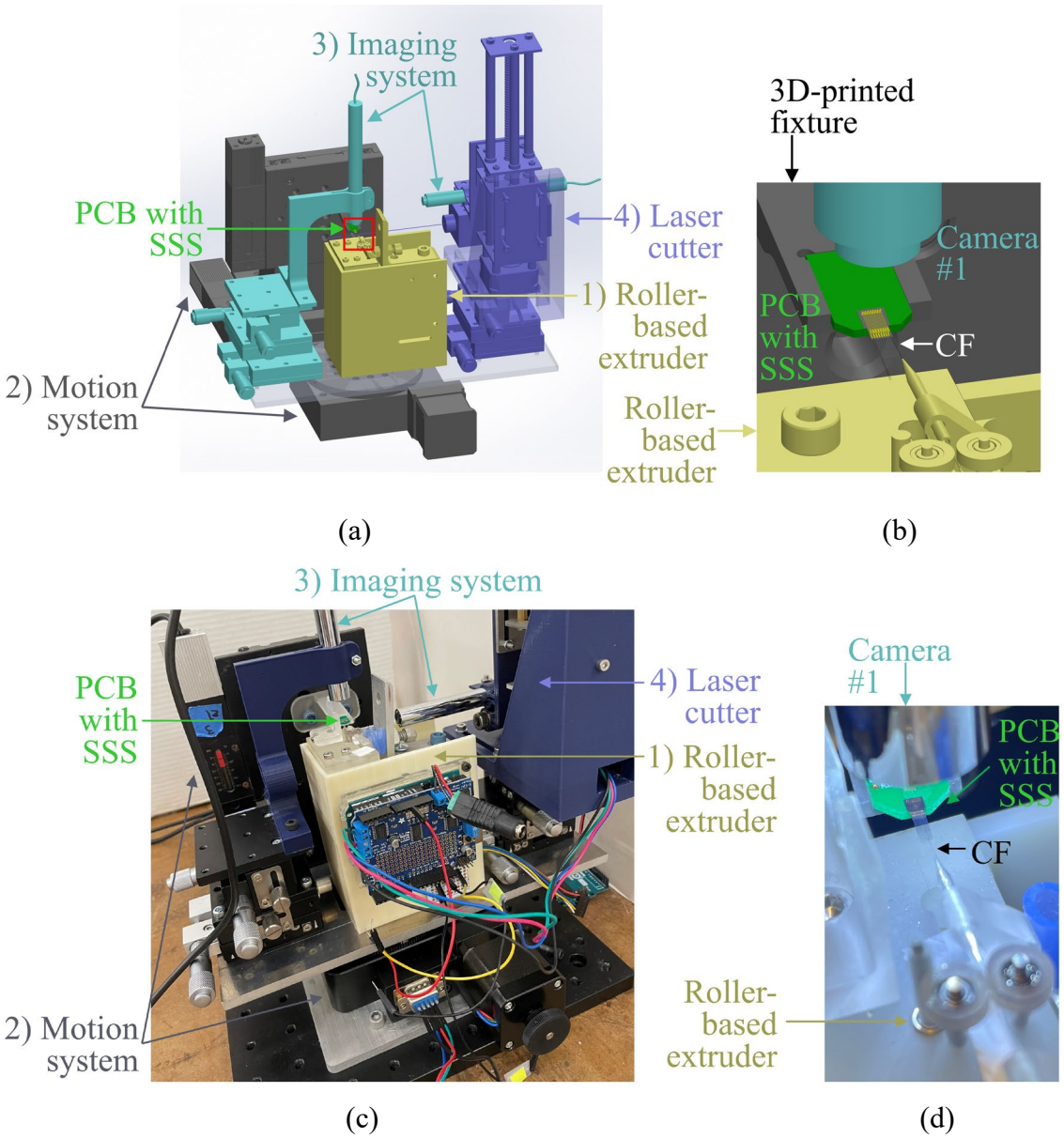


Figure 4.1: HDCF array assembly system and its four subsystems: (a) 3D overview of the 1) roller-based extruder, 2) motion system, 3) imaging system, and 4) laser cutter, together with the PCB with SSS as the starting workpiece, (b) close-up view of the red-boxed area in figure 2A including the PCB with SSS, camera (in the imaging system), and CF (from the roller-based extruder); pictures of (c) the physical machine and (d) close-up view of the roller-based extruder, the PCB with SSS, Camera #1, and the CF.

4.1.1 Subsystem 1: Roller-based extruder

The roller-based extruder realized automatic feeding of single CF for the HDCF array assembly system. As shown in Figure 4.2, this subsystem consisted of: 1) an adjustable base, 2) two feeding rollers, 3) a direct current (DC) drive motor, and 4) two Parylene C coated tapered glass capillary tubes. Two main features distinguished this CF feeding extruder from the open-source automated high-density microwire neural recording array assembly system [51]: 1) adjustable roller compression preload for feeding, 2) coated capillary tubes to prevent CF sticking due to electrostatic charging.

The adjustable base (Figure 4.2(b)) contained two base plates 10 mm apart, to provide structural support for the rollers and the motor shaft. Both plates were 3D-printed (Form 2, Formlabs Inc., Somerville, MA) with transparent stereolithography resin (RS-F2-GPCL-04, Formlabs, Somerville, MA). The top plate had a 1.5 mm wide slot parallel and close to the edge, forming a flexural beam structure. Two rollers (5.4 mm in diameter) were located on the opposite side of this slot. The surfaces of the two feeding rollers and the motor drive shaft were wrapped by a layer of soft silicone (durometer 50A hardness) to increase the frictional force along the feed direction and move CF at the roller contact surface. By adjusting the clamping screw, the roller shaft distance and thus roller compressive preload could be precisely controlled.

Two tapered glass capillary tubes were used to provide guidance for the CF along the feeding direction. The two tubes were set along the perpendicular bisector of the two roller's centers with their tips pointing towards the feeding direction. CF would be advanced through capillary tube #1, between two rollers, then through capillary tube #2 towards the PCB, as shown in Figures 4.2(c) and (d).

To load the CF into the extruder for automatic feeding, a long section (about 6 cm in length) of CF was manually threaded into capillary tube #1 until the CF tip touched the contact region of the two rollers. The motor (Model 2285, Pololu, Las Vagas, NV) was turned on and its drive shaft (1.8 mm in diameter) in contact with roller #1 drives both rollers under a synchronized rotation through friction. The CF was advanced to the outlet of capillary tube #2 and the extruder was ready for use to feed CFEs onto SSS of the HDCF array.

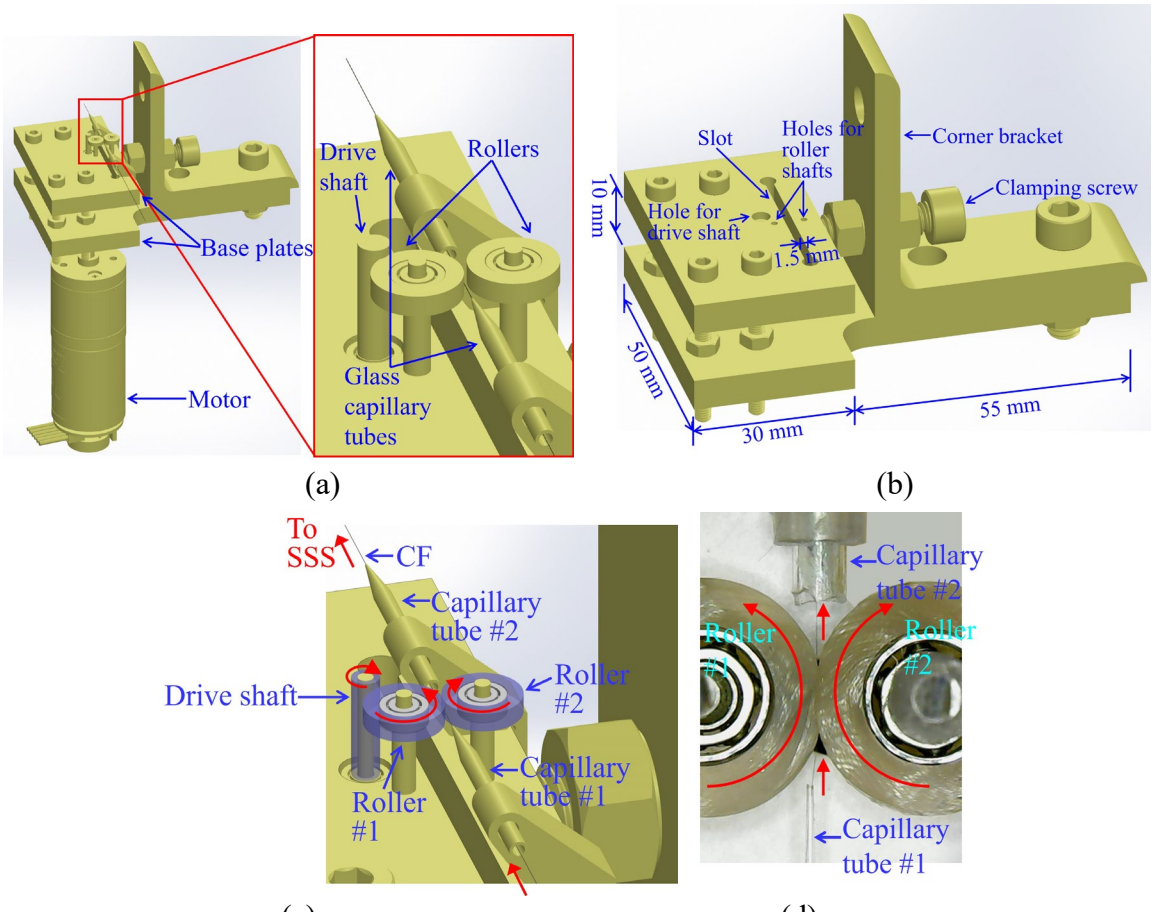


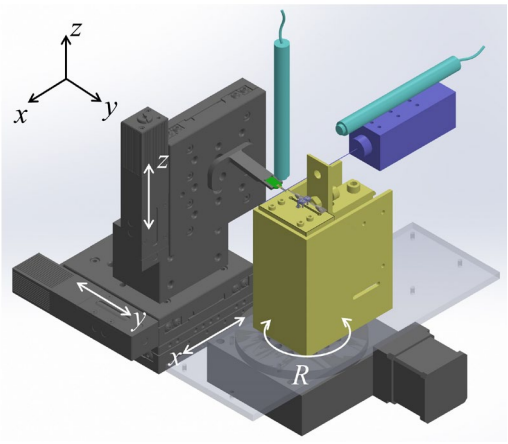
Figure 4.2: Roller-based extruder: (a) overview of the adjustable base, the rollers, the motor, and the glass capillary tubes, (b) the adjustable base, (c) rollers and shaft with soft silicone coating (colored in transparent azure) and CF extrusion mechanism (motions are marked in red arrows), and (d) a photo of CF being advanced from capillary tube #1 to capillary tube #2 by the friction from the rollers.

4.1.2 Subsystem 2: Motion system

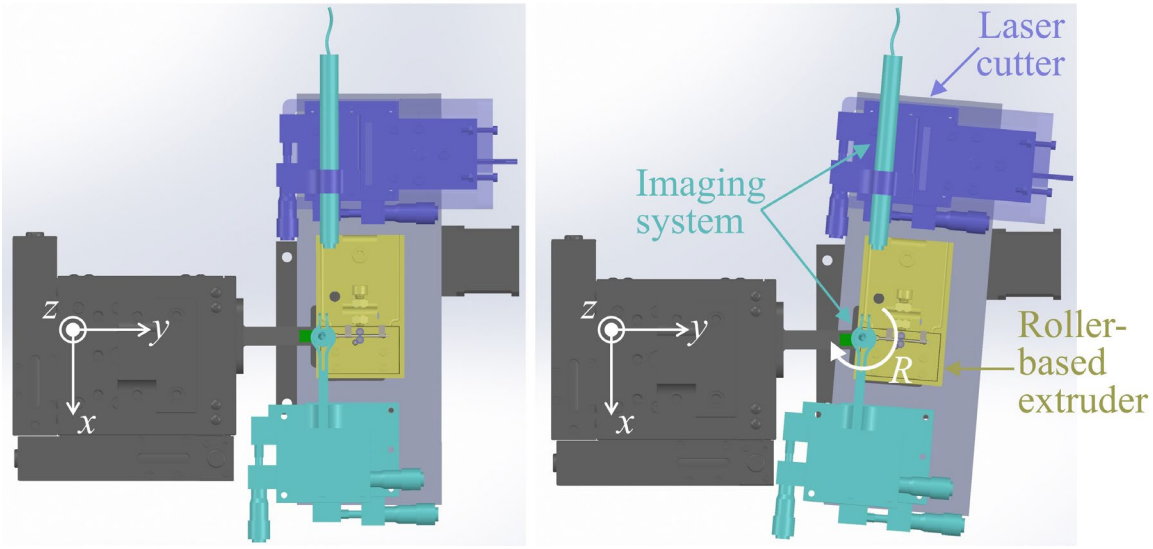
The motion system had one rotary stage (HT03RA100, Jiangyun Technology, Beijing, China) and three linear stages (100cri-R, Siskiyou, Grants Pass, OR), as shown in Figure 4.3(a). The rotary stage rotated the roller-based extruder to get the extruded CF parallel with the shanks in the SSS. The center of rotation was selected as the tip of the capillary tube #2 of the roller-based extruder. The rotary stage also rotated the two digital cameras in the imaging system and the laser cutter together to keep the CF-camera-laser relative position and alignment. The *x* and *y* linear stages then translated the PCB with the information from the imaging system (Section 4.1.3) and image processing algorithms (Sections 3.3 and 3.4) to align a CF with the specific trench in the shank of the SSS along the *x*- and *y*-directions. Finally, the *z* linear stage elevated the PCB to land the CF tip on the gold pad in the SSS and place the CF within the trench in the shank of the SSS (to be elaborated in Section 4.2).

4.1.3 Subsystem 3: Imaging system

Two digital microscope cameras (OT-HD, Opti-TekScope, Chandler, AZ), marked as cameras #1 and #2, are shown in Figure 4.4(a). Camera #1 was mounted on the rotating stage platform through a manual 3-axis linear stage (LD60-LM, ToAuto, Shenzhen, China), and pointed along the negative *z*-direction. The focus of camera #1 was adjusted to the extruded CF tip. Camera #1 provided an image of shanks and CF orientation in the *xy* plane. This image was the input for the image processing algorithms to find the CF tip's relative position to the gold pads (Figure 4.4(b)). Camera #2 was located on the side of the PCB and pointed along the positive *x*-direction with its focus on the shanks. Camera #2 provided the image of the shanks and CF orientation in the *yz* plane. This image was used to find the height of the PCB and determine the contact of CF with the SSS (Figure 4.4(c)).

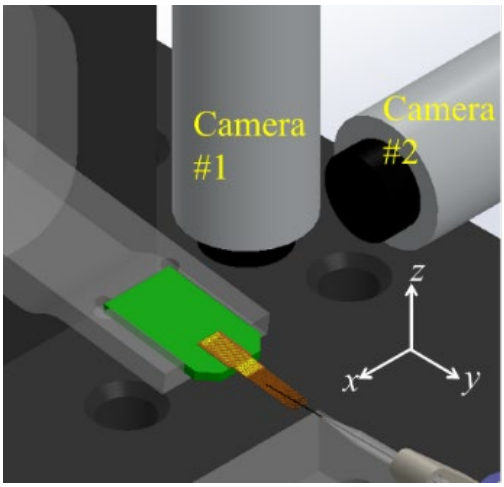


(a)

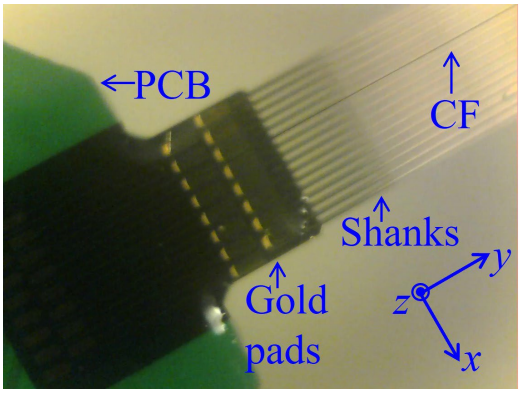


(b)

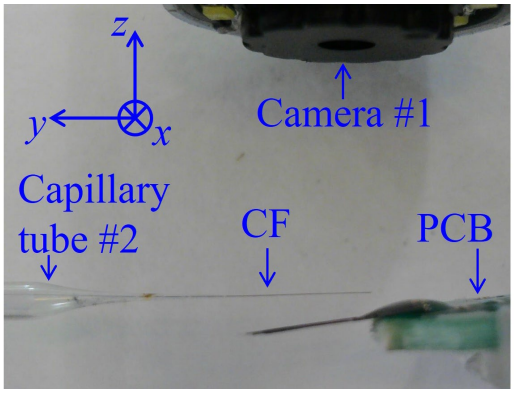
Figure 4.3: (a) Motion system: three linear stages for PCB translation in x-, y- and z-directions and the rotary stage R for CF rotation and (b) the rotary stage rotates the roller-based extruder, the imaging system, and the laser cutter together (top view).



(a)



(b)



(c)

Figure 4.4: Imaging system: (a) camera #1 and camera #2, (b) top view of assembly area from camera #1, and (c) side view of assembly area from camera #2.

4.1.4 Subsystem 4: Laser cutter

The laser cutter subsystem, as shown in Figure 4.5(a), consisted of 1) a blue laser head with 500 mW output power and 445 nm (± 5 nm) wavelength (D-B500F, Lian Dian Chuang Technology, Shenzhen, China), 2) a motorized linear stage (T8-Z150, Huizhou Bachin Electronic Technology, Huizhou, China), and 3) a manual 3-axis linear stage (LD60-LM, ToAuto, Shenzhen, China). The position of the laser head in *y*-direction was adjusted to align with the Capillary #2 tip with the manual linear stage prior to assembly.

To cut off the CF from the extruder, the laser head was powered on and moved by the motorized linear stage in the positive *z*-direction until the laser beam hit the CF, as shown in Figure 4.5(b). The CF could be cut off in less than five seconds with the 12 DCV input voltage of the focused laser beam. After cutting, the laser head was moved down to its original position to allow the camera #2 for imaging.

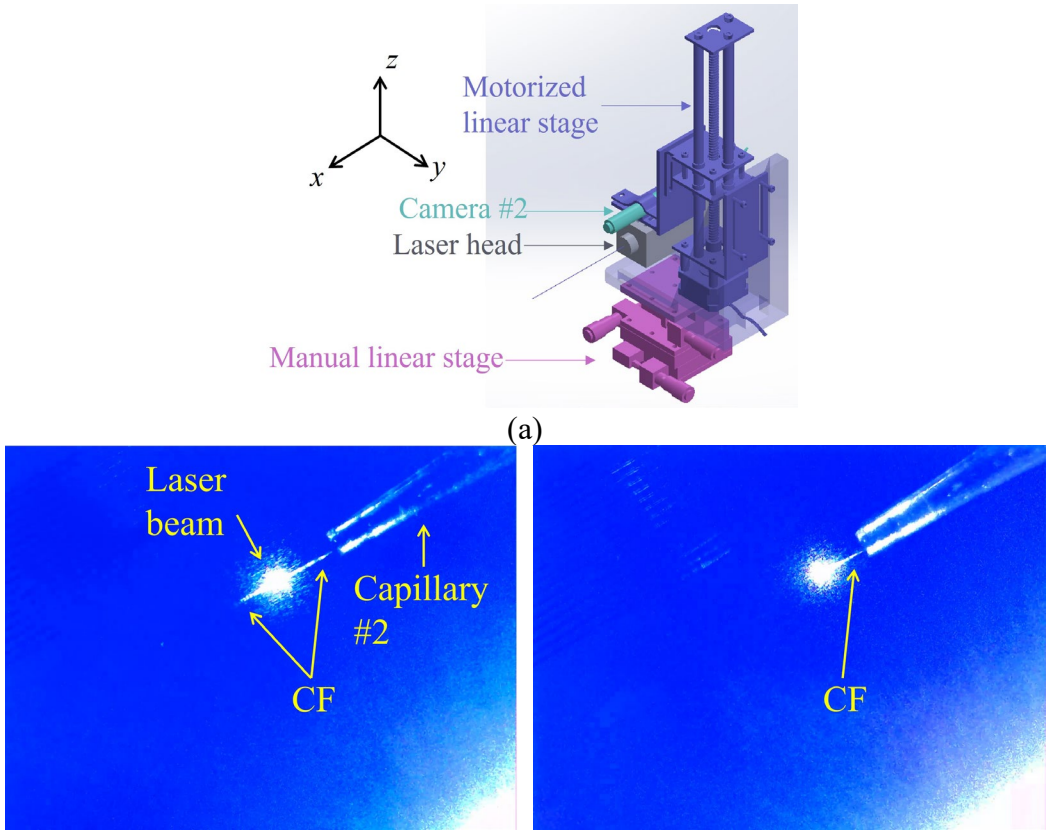


Figure 4.5: (a) Laser cutter components: laser head, motorized linear stage, and manual linear stage and (b) laser beam cutting off the CF (top view).

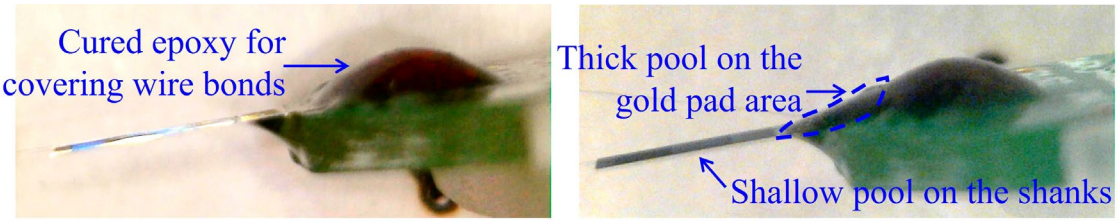
4.1.5 Controller and software platform

MATLAB (R2020b, Mathworks, Natick, MA) was used as the master software platform for computer control and synchronization of all subsystems in the HDCF array assembly machine. The roller-based extruder was controlled using an Arduino Uno microcontroller. The

controller of three linear stages was NI PCI-7344 with LabVIEW VIs (National Instruments, Austin, TX). The controller of the rotating stage and the motorized linear stage for the laser cutter was the Arduino Uno microcontroller with a DRV8825 stepper motor driver.

4.2 Carbon fiber electrodes population

To facilitate CFs sliding into the trenches, a drop of deionized water was put on and spread across the SSS with a tapered glass capillary tube. As shown in Figure 4.6, around the epoxy which secures the SSS to the PCB (refer to Section 3.2 Step 1), a liquid pool was formed. The deionized water pool was thick at the gold pad area and shallow around the shank. During the CFE population, deionized water needed to be refilled whenever it totally evaporated. At the completion of the CFE population, deionized water had evaporated and no solid residue was left on the SSS.

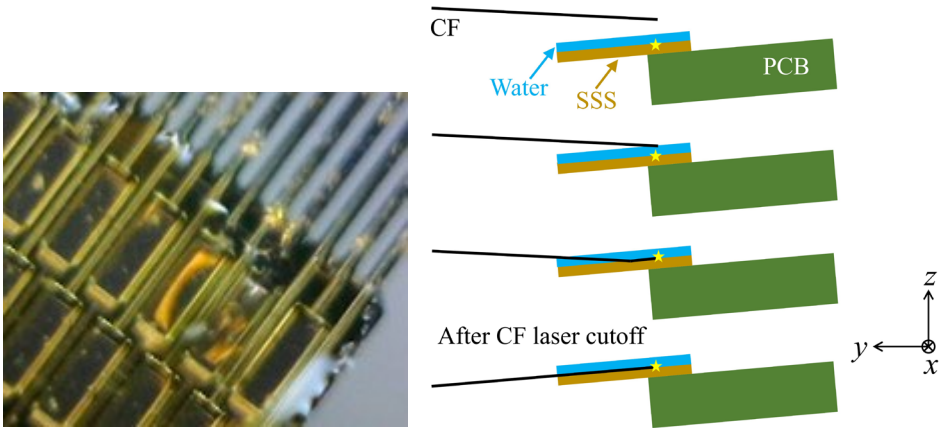


(a) (b)

Figure 4.6: Photos from camera #2 (a) before and (b) after the deionized water application around the epoxy covering the wire bonds between the SSS and the PCB.

CFEs were populated on the SSS shank-by-shank by repeating an extrusion-placement-cut off process. First, a 4 mm long CF was fed from the tip of capillary tube #2. The CF tip is located above the gold pad area and inside the viewing area of Camera #1. Second, CF was aligned parallel to the shank based on Algorithm I, and its tip was moved to the target position based on Algorithm II, which was executed 3 times iteratively. Third, the CF tip was landed on

the gold pad and the rest of the CF was pulled into the trench by surface tension, as shown in figure 10. Lastly, the CF was cut off with the laser cutter after verifying that the full length of the shank was occupied by CF in camera #2's view. The extrusion-placement-cutoff process is repeated 16 times for the CFE population in 16 gold pads on the SSS.



(a) (b)

Figure 4.7: CF landing: (a) CF tip touching the gold pad and (b) CF pulled into the trenches on the shanks by the surface tension of the water.

4.3 Subsystem tests and results

Three subsystem tests, marked as Exps. I, II, and III, were conducted to study the: 1) effect of Parylene C coating in the extruder capillaries, 2) CF extrusion accuracy of the extruder, and 3) effect of translational speed in *z*-direction on CF placement, respectively.

4.3.1 Exp. I: Effect of Parylene C coating in the extruder capillary tubes

CF loading and extruding tests were carried out for extruders with borosilicate glass capillary tubes with and without the Parylene C coating. For the capillary tube without coating, five attempts on CF loading/extrusion were made, and none of them succeeded due to CF adhering, likely by electrostatic force, to the inner wall of the glass capillary tube. For the

capillary tube with Parylene C coating, extrusion tests on four CFs (15 extrusions per CF) were performed with 100% success (n = 60). This indicated that the Parylene C coating on the glass capillary tube reduced the adhesion force and the static friction. Thus, the inner walls of glass capillary tubes were coated with approximately 800 nm of Parylene C through chemical vapor deposition to prevent the CF-tube adhesion due to electrostatic charge.

Prior studies show that Parylene C leads to larger electrostatic force due to higher resistivity compared to that of borosilicate glass [53,54]. As shown in Figure 4.8, the glass capillary tube with Parylene C coating outside can attract CF from a larger distance compared to the bare glass capillary tube. However, Parylene C coating is also a solid lubricant film with a lower coefficient of friction [55,56]. The lubrication from Parylene C likely contributes to the better performance of the extruder.

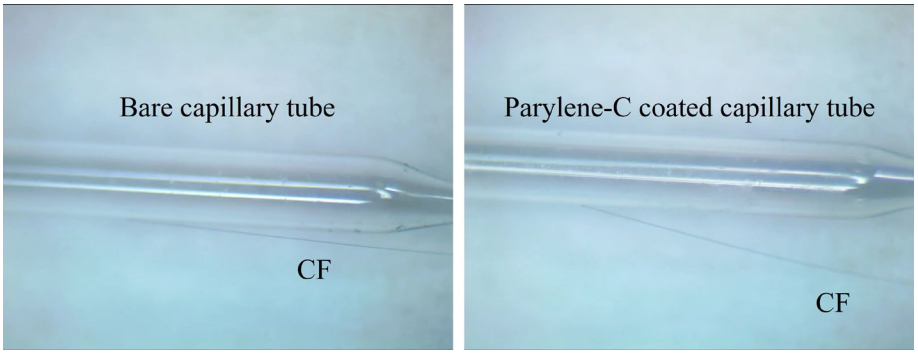


Figure 4.8: Parylene C coated capillary tube exhibiting more static charges and attracting CF from a larger distance.

4.3.2 Exp. II: the CF extrusion accuracy of the roller-based extruder

To test the accuracy of the extruder, 11 CF extrusion tests were carried out. The desired length of extrusion was set as 4 mm. The length of extruded CF was evaluated based on images taken by the imaging subsystem (Section 4.1.3) before and after extrusion using the diameter of

the glass capillary tube as a scale. The results showed good accuracy with extrusion length of 4.009 ± 0.073 mm (n = 11, mean ± SD).

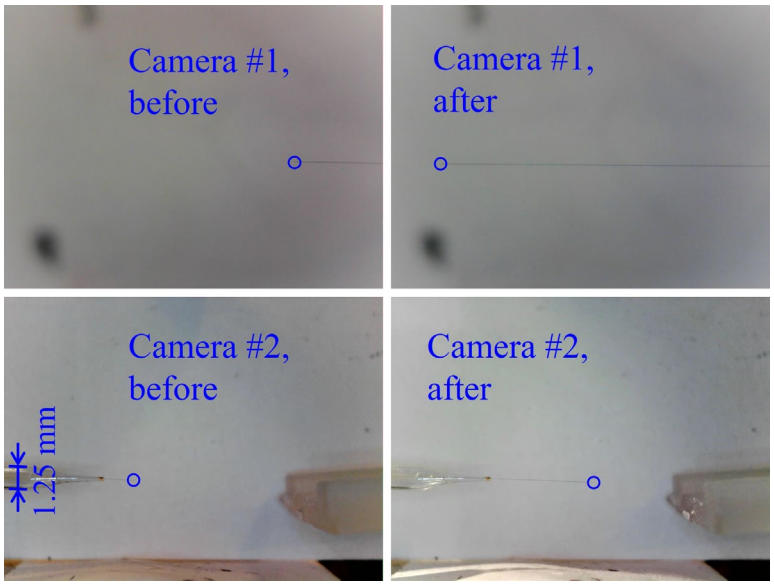


Figure 4.9: CF extrusion length measurement based on the pixel of the CF tip (blue circle) with the capillary tube diameter as the scale.

4.3.3 Exp. III: Effect of translational speed in the z-direction on CF placement

The goal for Exp. III is to select a speed for PCB elevation in *z*-direction that ensures the CF lands on the gold pads and trenches successfully. Exp. III was conducted by elevating the PCB with SSS at four speeds (0.02, 0.05, 0.1, 0.25 mm/s) and observing whether the CF landed on the gold pads and trenches correctly. At a high speed greater than 0.05 mm/s, a large portion of the CF would touch the liquid pool surface before the CF tip could be pinned on the gold pad. In this situation, the tip of CF would deviate suddenly from the gold pad because of the surface tension and curvature of the liquid pool. When the speed was less than or equal to 0.05 mm, the CF would land on the trench gradually with its tip pinned at the gold pad. Therefore, the speed of 0.05 mm/s in the *z*-direction was selected.

4.4 HDCF assembly machine evaluation

CFEs are populated on the SSS repeatedly to evaluate the performance of the machine. Two HDCF arrays with 16 CFEs populated on 3 mm shanks (with 80 μm pitch) were fully assembled using this machine. Results of the time duration of each step is summarized in Section 4.4.1. The failures are analyzed in Section 4.4.2. The fully populated devices are evaluated in Section 4.4.3.

4.4.1 Duration of assembly steps

The estimated time duration of each step is summarized in Table 4.1. The estimated operation time for placing one CFE is between 288 and 398 s. The variation comes from the corrective operations in Steps 1 and 2.2. This does currently take a longer time than the manual assembly (about 10 to 20 s per CFE for an experienced assembler) but does not require a skilled technician. The machine can eliminate manual alignment of 7 μm CF with 12 μm trench. The assembly process is monitored with visualization from the top and side.

Table 4.1: Estimated time of each assembly step

Step #	Operation	Time (s)
0	Water application	40
	Water pool inspection	30
1	Extrusion	3
	Extrusion inspection	15
	CF cutoff if extrusion goes wrong	50
2.1	CF rotation	10
	Rotation inspection	20
2.2	CF tip alignment	20
	Parameter searching if the default (b, n) does not work	60
2.3	CF landing	30
	CF landing inspection	60
3	CF cutoff	30
	Reset for next CFE	30
Total		288-398

4.4.2 Failure analysis

Two types of failure were observed during the assembly trials. The first and most common failure is the breakage of shanks during the water application, as shown in Figure 4.10. The water pool covering the SSS would evaporate in three to four minutes. A drop of deionized water needs to be put on and spread across the SSS at least once for every CFE. The glass capillary tube could accidentally touch and break the thin shank during the manual water refill. A

way to avoid this failure is to automate the water refilling process. A setup will be proposed in Chapter 5.

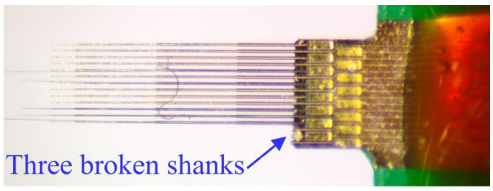
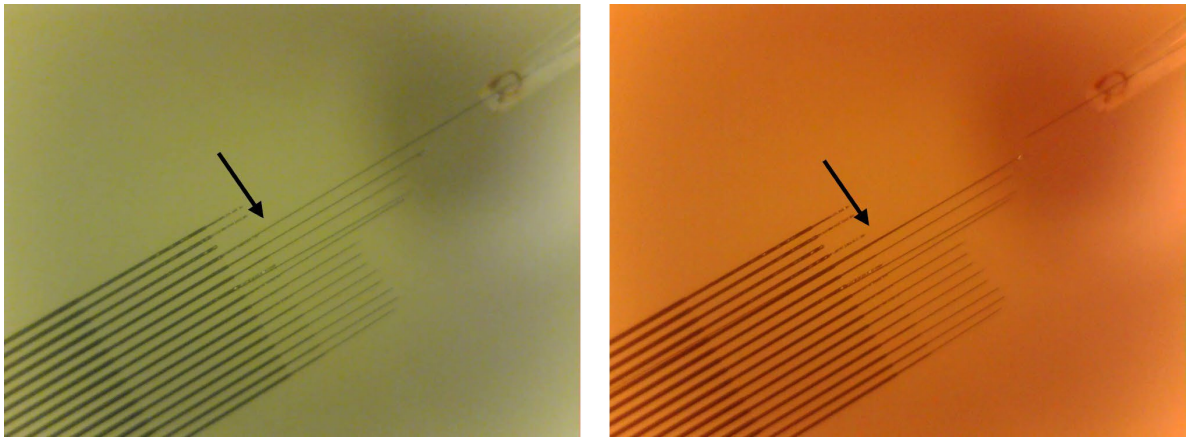


Figure 4.10: Shank breakage due to deionized water application.

The second failure is the escaping of a landed CFE from its original trench after laser cutting, as shown in Figure 4.11. The CF might be bent but temporarily pulled into the trench by the surface tension of the water while still connected to the long section of CF in the capillary tube #2 of the extruder. The bent CFE could move out of the trench after laser cutting. To avoid this failure, it is necessary to inspect the bending of the 4 mm extruded CF using Camera #1. If excess bending is observed, this segment of CF can be cut by laser and discarded.



(a) (b)

Figure 4.11: CFE escaped from the trench: (a) CFE landed in the trench before cutting and (b) CFE deviated from the shank and touched the nearby CFE.

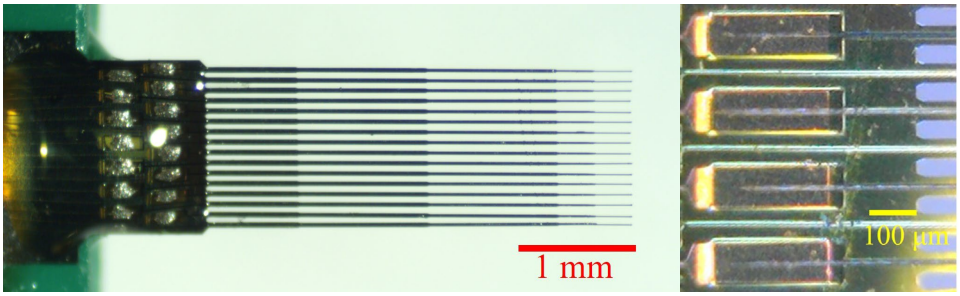
4.4.3 EIS and in-vivo electrophysiology recording with assembled HDCF arrays

Two HDCF arrays with 16 CFEs populated on 3 mm shanks (with 80 μm pitch) were fully assembled using this machine, as shown in Figure 4.12. CFEs were placed accurately within the silver epoxy wells and trenches. The HDCF arrays demonstrated the feasibility and repeatability of the developed assembly machine.

Assembly Steps 4-7 including electrical connection, physical reinforcement, device insulation, and CFE functionalization described in Section 3.2 for HDCF array were carried out. To characterize the arrays' impedances, measurements were taken with a PGSTAT12 Autolab potentiostat (Metreohm/Eco Chemie, Utrecht, Netherlands) which was controlled using the vendor supplied NOVA software. For each measurement session the device was submerged by approximately 1 mm in 1x phosphate buffered saline (BP3994, Fisher, Waltham, MA). The reference was provided by an Ag|AgCl electrode (RE-5B, BASi, West Lafayette, MA) and the counter by a stainless steel rod. Measurements were applied from 10 Hz to 31 kHz with a 10 μV_{RMS} signal. Data was analysed using custom MATLAB scripts. After each major step listed below impedance measurements were taken. In brief, silver epoxy was applied to the wells, heat cured, and the protruding fibers scissor cut to 350 μm (n=27 connected fibers, 164 ± 28 kΩ, 1 kHz impedance). Then the devices were coated with Parylene C, laser cut to 300 μm which exposes the tip [7], and plasma treated (1682 ± 158 kΩ) [41]. Finally the newly exposed tips were coated with PEDOT:pTS via electrodeposition (18 ± 1 kΩ) [7]. The impedance measurements were found to be in good agreement with our past findings (Figure 4.13) [7,41].

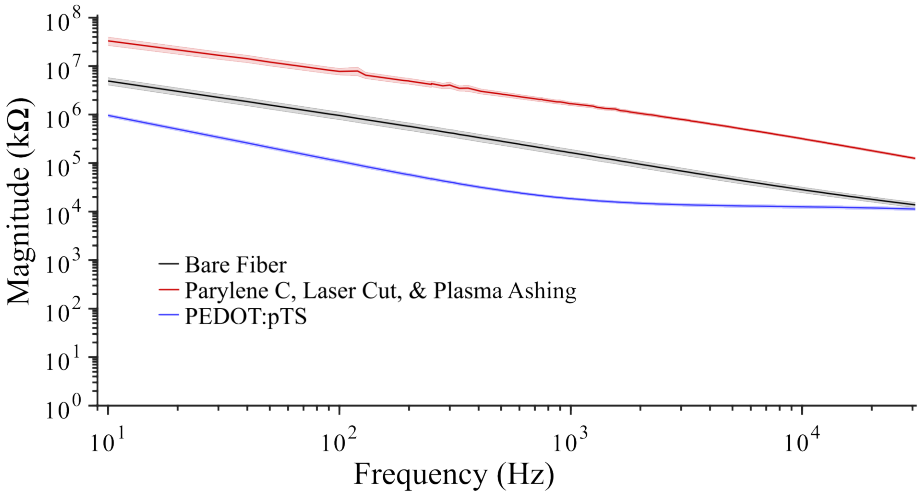
To validate the fully assembled and functionalized devices, one of them was implanted in layer V of the motor cortex in an anesthetized rat. A male Long Evans rat was first anesthetized using a combination of ketamine (90 mg/kg) and xylazine (5 mg/kg) via intraperitoneal (IP)

injection. Carprofen (5 mg/kg) was given once, subcutaneously. Subsequent boosters of ketamine (30 mg/kg) were also given IP. Once down the rat's head was shaved, then cleaned using alternating wipes of 70% ethanol and betadine. Next a midline incision was made and the skin pulled back. A bone screw in the posterior portion of the skull was screwed in and served as the ground/reference connection. Next a craniotomy was made over motor cortex, the dura resected, and the probe inserted. All procedures and monitoring complied with the University of Michigan's Institutional Animal Care & Use Committee. Recordings were taken with a system from Tucker-Davis Technologies and is described in detail elsewhere [5]. Electrophysiology data analysis was conducted with Offline Sorter (Plexon, Dallas, TX) with the full methodology described in [7]. Of the 16 channels present, 10 were able to detect single unit activity (Figure 4.14). Across those 10 channels, 17 individual units were detected with a mean amplitude of 105 μV.

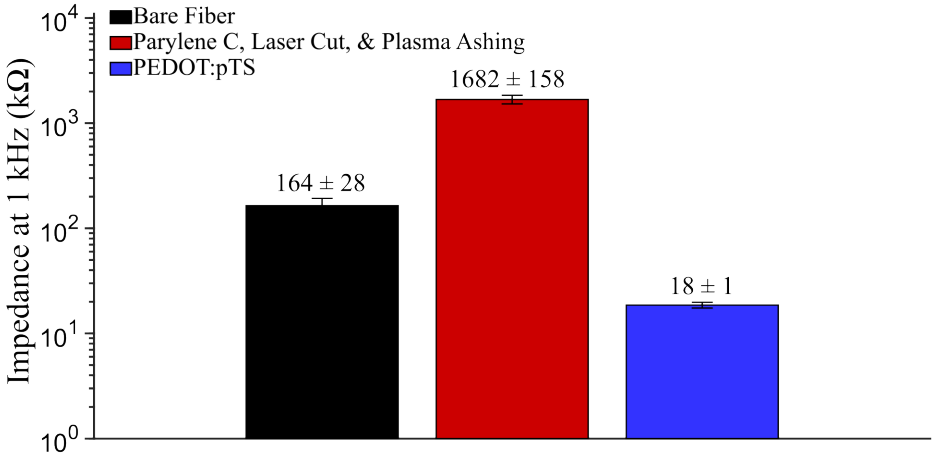


(a) (b)

Figure 4.12: (a) Fully populated HDCF array and (b) the closed-up view of CFEs on the gold pads (before silver epoxy application).



(a)



(b)

Figure 4.13: (a) Bode magnitude plots of the measured impedance after the three major functionalization steps (n=27 fibers, mean ± SD) and (b) one kilohertz impedance values (n=27 fibers, mean ± SD) shown for the three major processing steps. As seen in previous results, coating with PEDOT:pTS greatly reduces the impedance of the electrodes.

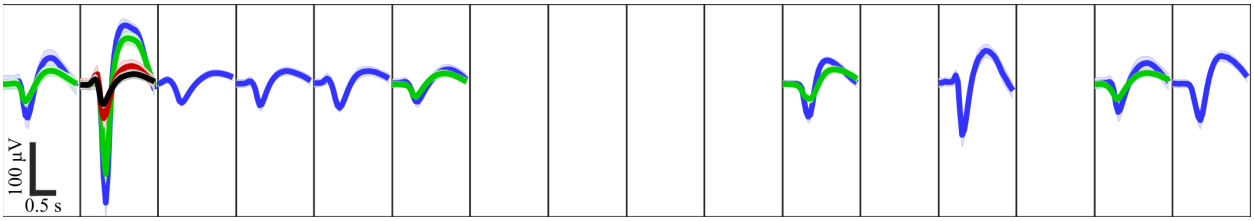


Figure 4.14: Spike panel of the detected unit activity from layer V motor cortex of an anesthetized rat.

4.5 Conclusions

An automatic HDCF array assembly machine capable of the repeated precise placement of CFEs along 12 μm wide trenches with an 80 μm pitch in SSS was developed. The machine's hardware requirements, including the 1) precise and stable motion to position the CF, 2) soft physical contact of the CF and SSS, 3) compact spatial configuration, and 4) ability to record and monitor the process, were demonstrated. The machine was capable to assemble two functional HDCF arrays.

Chapter 5 Conclusions and Future Work

5.1 Conclusions

This work has shown the laser cutting and sharpening of CFEs and the automatic HDCF array assembly machine. The laser cutoff and sharpening method is the only way, to the best of our knowledge, that gives a CFE array with sharp tips and custom lengths. The automatic HDCF array assembly machine is novel in the capability to repeatedly align both the CFE tip location and its orientation with the SSS to assemble an array.

In Chapter 2, a laser CFE cutoff and sharpening method was elaborated. A moving laser beam traced across the CF could realize the cutting, sharpening, and insulation removal of CFEs in an array with custom electrode length simultaneously. A combination of high cutting speed and high power was selected to achieve a sharp tip geometry and short insulation stripped length. The laser path was designed based on targeted electrode lengths. An array of four laser sharpened CFEs was fabricated. EIS and an in-vivo recording with rat motor cortex were conducted and validated the function of the laser sharpened CFEs.

In Chapter 3, Algorithm I to measure the orientation of the CF and Algorithm II to calculate the distance between the CF tip and the desired target location were developed for aligning the CF with the SSS of the HDCF array. Algorithm II had two adjustable parameters for flexibility under different lighting conditions. Both algorithms were implemented in and tested with the HDCF assembly machine introduced in Chapter 4. Algorithm I could reduce the CF deviation to less than one degree. Algorithm II could achieve the distance in the critical x-direction between CF tip and desired target location to less than 40 μm. Both algorithms played

important roles in ensuring the CFE's successful placement with the automatic HDCF array assembly machine introduced in Chapter 4.

In Chapter 4, an HDCF array assembly machine was constructed for automatic accurate placement of CFEs with an 80 μm pitch. This machine had a roller-based extruder, a motion system, an imaging system, and a laser cutter. CF was extruded from the roller-based extruder, aligned parallel to and placed along the shanks by the motion system with the calculation based on Algorithms I and II and inputs from the imaging system, and cut off by the laser. Subsystem tests were conducted on extruder accuracy and *z*-axis speed on CF placement. This machine was proved to be feasible by the assembly of two HDCF arrays with 16 CFEs. The impedance measurements were taken and found to be in good agreement with our past findings. The assembled HDCF array was implanted in a rat motor cortex and was able to detect single unit activities.

5.2 Future work

The automatic HDCF array assembly machine shows the potential to replace or supplement manual fabrication of HDCF array. Two ideas to further automate the CFE placement process are: 1) automate the parameter selection process for Algorithm II and 2) automate the water refill process.

The parameters in the elaborated algorithms may need manual tuning to reach an optimal detection. The integrated parameters were selected through preliminary trials and worked for over 80% of the detection trials. The failure might be a result of the fluctuating lighting conditions and was fixed by searching for two parameters following some strategy within the nearby range manually. This tuning process could be later automated according to the elaborated strategy. The parameters may also be selected by collecting the information of lighting condition

through the background pixels and calculating the optimal value. The machine may work better in a controlled environment.

Figure 5.1 shows the concept using with a pump to constantly dispense water on SSS. The spatial configuration of the water outlet would be challenging because it needs to move with the PCB, get around the cured epoxy for SSS fixture, stay close to the gold pad area but no contact. These two improvements would make the machine less dependent on the user's experience and hand steadiness.

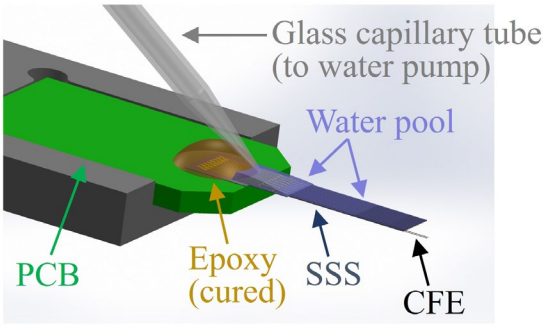


Figure 5.1: Automatic water pool refill using a water pump to constantly dispense deionized water on the SSS for compensation of the water evaporation.

There are multiple implications of this work. First, like recent work using additive manufacturing [57], this HDCF array assembly machine demonstrates another alternative to traditional silicon array fabrication. While this work utilized carbon fiber, it could likely be extended to fabrication in other geometries and with other electrode materials not amenable to lithography such as tungsten. Second, this machine was relatively inexpensive and could be implemented by neuroscience labs that struggle with manual assembly of microwire arrays. Finally, the primary benefit of carbon fiber arrays compared to other softer subcellular electrodes is ease of surgical insertion, which simply requires a stereotaxic frame and micromanipulator.

This paper suggests that a robotic approach at time of fabrication may obviate the need for a robot to perform the surgery itself.

Appendix Flexible High-Resolution Force and Dimpling Measurement System for Pia and Dura Penetration During In Vivo Microelectrode Insertion Into Rat Brain

The study on microwire insertion force measurement is introduced in Appendix A. The work has been published in IEEE Transactions on Biomedical Engineering and Tianshu Dong contributed to design, experiments and data analysis. The result explains the motivation for Chapter 2 carbon fiber electrode sharpening.

In this study, a new force and dimpling measurement system is presented to evaluate the in vivo forces of thin microwires under 100 μm diameter with μN resolution in an anesthetized animal. The system is based on a simple cantilever beam setup made with easily accessible components to achieve high resolution (<1 μN) and sampling rate (500 Hz), making it broadly duplicable by the neuroscience community. By using cantilever beams of various sizes, this flexible and reconfigurable system can evaluate both pia-only and dura-pia penetration processes, even with multi-shank silicon-based probes as the insertion device. Taking advantage of the developed system, live-rat force profiles and dimpling depths of microwires with various diameters, materials, and tip shapes were studied.

A.1 Methods

A.1.1 Force measurement system design

A conceptual overview of the force measurement system is shown in Figure A.1(a). The system consisted of a cantilever beam, a 3D-printed top plate on the beam for microwire fixation,

and three computer-controlled linear stages (Model 100cri by Siskiyou, Grants Pass, OR) to move the rat and brain along *x*-, *y*-, and *z*-axes. A laser displacement sensor was used to measure the cantilever beam deflection during the in vivo microelectrode insertion, as shown in Figure A.1(b). The brain of a live anesthetized rat was exposed and fixed on *x*-axis linear stage by laying the animal on its side with its head fixed by a 3D-printed fixture (Figure A.1(c)). The vertical cantilever beam setup with the animal on its side was chosen over the more standard top-down insertion orientation to mitigate the effect of gravity on bending of the long and highly flexible and sensitive cantilever beam (to be demonstrated in Section A.1.2). Stages in *y*- and *z*-axes positioned the exposed brain region of anesthetized animal to the microwire for in vivo insertion. The *x*-axis linear stage moved the brain against the microwire by a distance d_t. Due to the force (F_i) that the microwire encountered during the implantation, the cantilever beam deflected by d_l at the microwire height (l from the base of the cantilever beam) and d_c at the laser sensor height (c from the base of the cantilever beam). The laser sensor used in this study (Model LK-G10 by Keyence, Osaka, Japan) had a 0.3 mW 650 nm red semiconductor laser and used optical triangulation to measure distance. The sensor had a 0.01 μm measurement repeatability and 2 mm range. The distance c was 171 mm. To enable force measurement at different ranges (sub-mN to tens of mN) for various microelectrodes and membrane penetration conditions, four different cantilever beams (Beams #1-4) with parameters listed in Table A.1 were used. These four beams have different widths and thicknesses to achieve various flexural stiffness. The beam flexural rigidity (EI) is calculated as:

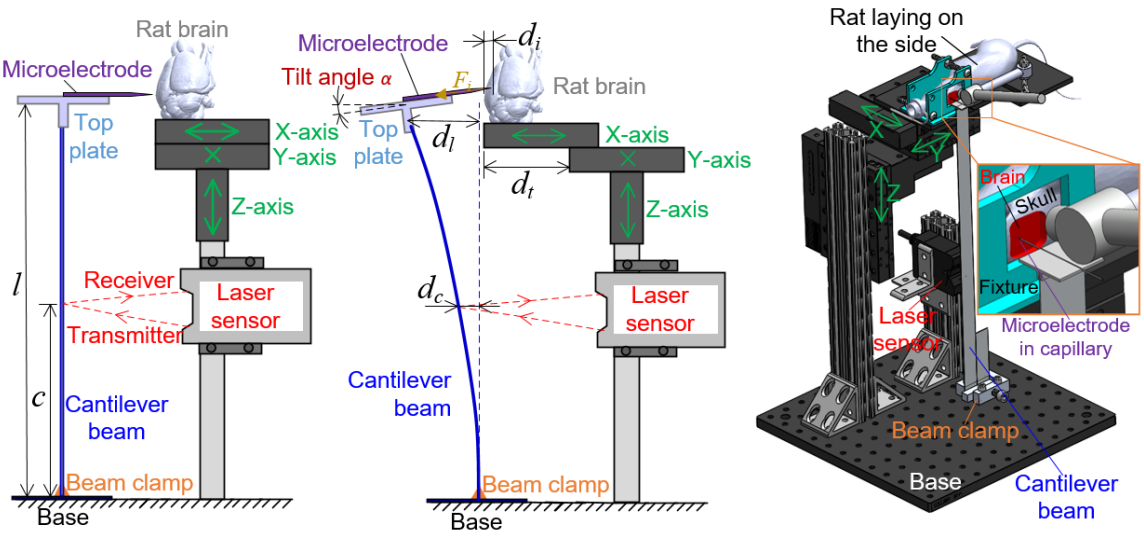
$$EI = E\frac{bh^3}{12}, \tag{A.1}$$

where E is the elastic modulus of the beam material (73.1 GPa for Al-2024 and 68.9 GPa for Al-6061), I is the moment of inertia of the beam, and b and h are width and thickness of the beam, correspondingly.

The displacement between the microwire tip and the undeformed brain surface, d_i, which indicates the tissue dimpling before membrane penetration and the insertion depth after tissue rebounding, is:

$$d_i = d_t - d_l, \tag{A.2}$$

where d_l is estimated from the laser sensor measurement of the beam deflection d_c. The correlations between F_i, d_l, and d_c were obtained through cantilever beam calibration (to be elaborated in Section A.1.2).



(a) (b) (c)

Figure A. 1: The in vivo microwire force measurement system: (a) conceptual overview, (b) side-view of cantilever beam bending during insertion, and (c) perspective view of experimental setup with anesthetized rat.

A perspective view of the cantilever beam force measurement system (with Beam #1 installed) and a window of exposed brain for microwire insertion in live anesthetized rat are shown in Figure A.1(c). The microelectrode was glued inside a capillary tube (0.3 mm inner diameter and 0.1 mm wall thickness) with the tip overhang outside. The tube was fixed onto the top just before testing with both ends extended beyond the plate by 10 mm to ensure the weight balance.

Table A. 1: Design parameters of four cantilever beams used in the study

Beam number	Material	Length l (mm)	Thickness h (mm)	Width b (mm)	Flexural rigidity EI ($N \cdot m^2$)
1	Al-2024	375	0.5	20	0.0152
2	Al-2024	375	0.625	20	0.0297
3	Al-2024	380	0.8	40	0.1248
4	Al-6061	380	1.5	20	0.3876

A.1.2 Force measurement system calibration

This newly developed force measurement system was calibrated through both experiments and finite element modeling (FEM) to correlate d_c with F_i and d_l.

A FEM was developed for each one of the four cantilever beams with corresponding top plates and capillary tubes. The effect of the microelectrode weight (less than 0.1 mN) was assumed to be negligible. As shown in the model overview for Beam #1 in Figure A.2(a), bottom of the beam (15 mm high, same as the beam clamp in experiment shown in Figure A.1) was fixed in all directions as boundary condition. The interfaces between the beam, top plate, and capillary tube were tied together in the model to simulate the rigid connection in experiments. Material properties of Al-2024 or Al-6061, borosilicate glass, and 3D-printed parts (using

Formlabs^{TM} clear resin) were applied to the beam, capillary tube, and 3D-printed top plate correspondingly. The force was applied on the end surface of the capillary tube and gravity of all three components were added. Note that a wider design of Beam #3 led to a wider top plate with larger weight (1.19 g) than the ones used for Beams # 1, 2, and 4 (0.60 g). The magnitude of the force applied was up to 60 mN for Beams #1, #2, and #3 and up to 200 mN for Beam #4. Figure A.2(b) shows the mesh setup of the Beam #1 model with 202,155 elements in total. Linear hexahedron elements were assigned to all three parts with average element size of 0.3, 0.8, and 0.1 mm for the beam, top plate, and capillary tube, respectively. Static analysis with steps of incrementally increasing force was conducted for all four beam models using Abaqus v6.11-1 FEM software.

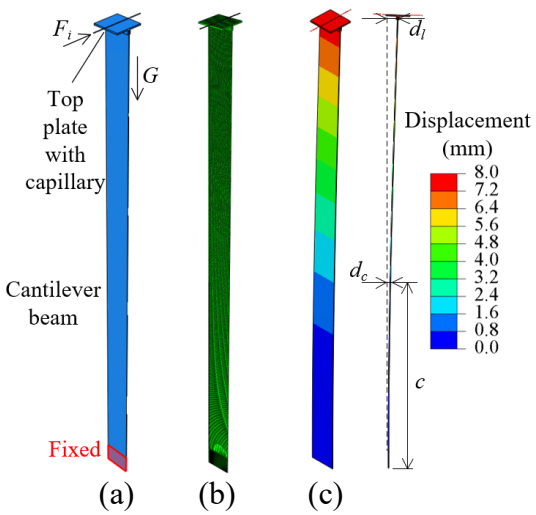
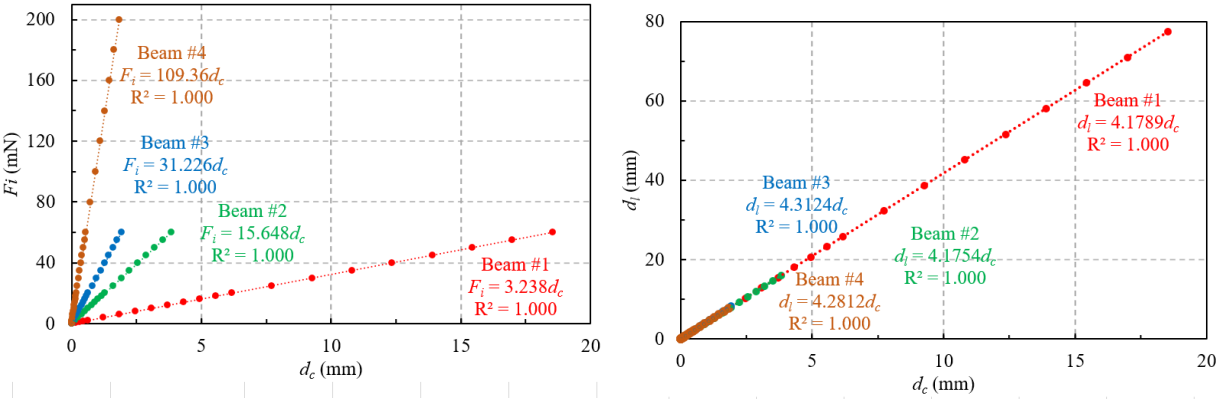


Figure A. 2: FEM of the cantilever beam system with Beam #1 as example: (a) model configuration overview, (b) FEM mesh setup, and (c) perspective and side views of the beam deflection result under 6 mN load.

A sample deflection result of Beam #1 under 6 mN force is as shown in Figure A.2(c), which generates a correlation between the F_i (6 mN), d_c (1.853 mm), and d_l (7.745 mm). A summary of all these correlations for four beams under incremental loadings is shown in Figure

A.3. Good linear correlations (R^2 = 1.000) were achieved for all eight mappings and the correlation coefficients are summarized in Table A.2.



(a) (b)

Figure A. 3: Calibration results of mapping between (a) F_i and d_c and (b) d_l and d_c for four different cantilever beam structures.

Table A. 2: Correlation coefficients from calibration results

Beam		#1	#2	#3	#4
F_i/d_c (mN/mm)	FEM	3.238	15.648	31.226	109.36
	Ideal cantilever	4.058	16.62	32.712	101.76
	Difference	20.21%	5.85%	4.54%	7.47%
d_l/d_c	FEM	4.1789	4.1754	4.3124	4.2812
	Experiment	4.2816	4.2544	4.3999	4.3775
	Discrepancy	2.40%	1.86%	1.99%	2.20%

Theoretical calculation of the F_i/d_c ratio (as in Table A.2) based on an ideal cantilever beam assumption yielded an up to 20% difference with the FEM results, indicating that gravity of the components did play an important role in the deflection due to high sensitivity of the beams and needed to be considered. This is also the reason why the vertical orientation of the

cantilever beam was chosen instead of the conventional top-down insertion orientation. To validate the accuracy of the FEM, experimental calibrations were carried out by pushing the capillary tube and top plate with *x*-axis linear stage (to achieve specific d_l) and recording d_c simultaneously. The experimentally achieved d_l/d_c ratio, as listed in Table A.2, matched well with FEM results with discrepancies less than 2.4%, validating the FEM setup and results. Note that direct calibration of the cantilever beam system or direct validation of the FEM model by force measurement was not achievable because there was not a commercially available force sensor that could measure μN-level resolution over tens and hundreds of mN-level range under a few mm displacement at μN accuracy and repeatability.

Given the 0.01 μm resolution and 2 mm range of the laser sensor at 171 mm height from the base used in this study, this force measurement system could measure up to 6.5 mN with 0.032 μN resolution with Beam #1 and up to 218 mN with 1.09 μN resolution with Beam #4.

A.1.3 Animal preparation

All animal experiments were carried out in accordance with the University of Michigan Institutional Animal Care and Use Committee (protocol number PRO00007803 Approved for 9/8/2017-9/8/2020 and PRO00009818 Approved for 7/13/2020-7/13/2023). For each insertion test, an anesthetized Sprague-Dawley rat was placed in a stereotaxic apparatus to fix the head and to perform a craniotomy to remove a window in the skull for microwire insertion. Anesthesia was induced and maintained with isoflurane throughout the procedure and vital signs were monitored during the entire process to make sure the animal remained within normal physiologic limits under anesthesia. Prior to surgery, carprofen was administered as an analgesic and a local anesthetic was administered to the scalp incision site prior to incision. After the animal was secured and positioned, scalp hair was removed, and the skin on the top of the head was cut by

surgical scalpel to expose the skull. To prevent tissue swelling, methylprednisolone (steroid) was given intraperitoneally at 15 mg/kg of animal weight. A dental drill with a 0.5-0.9 mm diameter burr bit was then used to remove one piece of the parietal bones to create a craniotomy window to expose the membrane layers. For dura-pia penetration tests, dura mater was left undamaged after craniotomy. For pia-only penetration tests, the dura mater of the exposed hemisphere was carefully removed using fine tweezers while leaving the pia mater intact. The rat was then moved and fixed on the *x*-axis linear stage of the force measurement system with the craniotomy window perpendicular to the microelectrode. To maintain anesthesia, a mobile oxygen and isoflurane mixing system was used and the nose cone was kept affixed to the animal's nose at all times. The animal and attached nosecone with both isoflurane delivery and exhaust tubing lines was transported to the top of the linear stages. The head was affixed with the craniotomy facing the cantilever beam using a custom 3D-printed head fixture with silicone padding lining to softly hold the head via pressure mount. Once the rat was affixed with gas tubing lines routed, the craniotomy was aligned with microwires to be inserted via movement of the rat with the linear stages along *y*- and *z*-directions.

During experiments, the surface of the pia or dura was cleaned with sterile 0.9% physiologic saline and re-wetted with this saline between insertions (about every 4-5 minutes) to prevent drying and to wash away any small amounts of blood to prevent clotting and consequent formation of a hardened surface outside the membrane, which would interfere with our insertion measurements. After insertion tests on one hemisphere, the exposed membrane layer was covered with triple antibiotic ointment in petroleum jelly to prevent any potential infections before conducting craniotomy surgery on the other hemisphere.

A.1.4 Setup of the force measurement system

Experimental setup of the developed force measurement system for in vivo insertion tests is shown in Figure A.4(a). The anesthetized rat was placed on its side with the head clamped by a 3D-printed fixture so that the craniotomy window was aligned with the fixture opening (as shown in Figure A.4(b)). During the experiment, motion of the entire rat was controlled by three linear stages with 25 mm travel range and 1 μm resolution. By moving the rat along the *x*-axis, the microwire was inserted into the brain through the craniotomy window (Figure A.4(b)). Simultaneously with the laser sensor recording, dimpling of the brain tissue and microelectrode penetration into the brain could be directly observed through the digital camera.

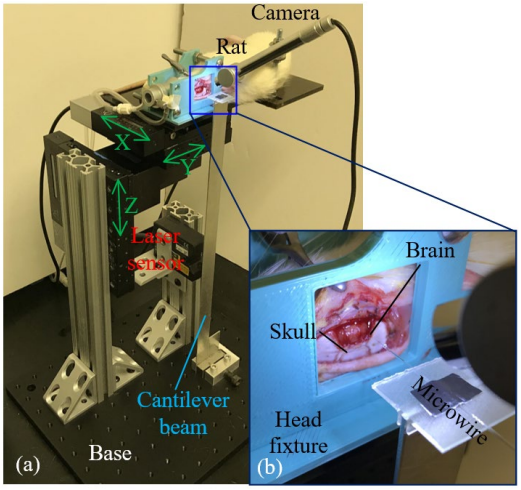


Figure A. 4: Experimental setup of microwire force measurement system: (a) anesthetized rat test setup overview and (b) close-up view of the microwire insertion into exposed rat brain.

A.1.5 Design of experiments

In this study, eight Sprague-Dawley rats (four males and four females, weighted 305-560 g) were used for in vivo insertion measurements. On each rat, one hemisphere was used for pia-only penetration tests and the other for dura-pia penetration measurements. As shown in Figure

5(a), 11 types of microwires including two materials (AISI 304 stainless steel and tungsten), four diameters (12, 25, 50, and 100 μm), and two tip geometries (polished blunt and electrochemical machining sharpened with 30° cone tip angle) were used for in vivo insertions. Overhang of microwires out of the capillary tubes were set as 1.5 mm for 12 and 25 μm wires and 3.0 mm for 50 and 100 μm wires. These values were chosen through preliminary trials to ensure manual microwire assembly practicability, reasonable critical buckling load for penetration, and minimal possibility of the thick capillary tube poking into the brain during cantilever beam rebounding after membrane penetration. For pia-only penetration, two new wires of each type were used for testing on each rat, yielding 22 insertion sites on the hemisphere. For dura penetration, preliminary studies showed obvious difficulties of penetration for 12 μm microwires with the 1.5 mm overhang. Thus, 18 tests were conducted using the remaining nine microwire types on the dura penetration hemisphere of each rat. Insertion locations and orders were randomized on each hemisphere to minimize the variance from slight heterogeneities in brain structures and tissue property differences, though all penetrations were aimed at dorsal cortex. One exception to the random sequencing was that all the 100 μm wire insertions were conducted sequentially last for each hemisphere as these tests had the highest possibilities of excessive brain trauma and bleeding, preventing other insertion trials to be conducted afterwards. Random errors were also minimized by counterbalancing factors including animal sex, left/right hemisphere, and experiment order (conducting insertions on pia-only or dura-pia penetration hemisphere first).

Major blood vessels visible from the brain surface were avoided during the insertion tests. However, challenges still existed during the insertion tests including excessive bleeding by hitting a deep vessel or pia damage during dura removal. Also, whenever significant brain edema, evident opacification, or bleeding was observed, indicating inflammation of that tissue

and consequent changes in mechanical properties, experiments on that hemisphere were terminated with ongoing trial recording disregarded. As a result, 238 effective microwire insertion trials were conducted in total with 115 for pia-only penetration and 123 for dura-pia penetration.

To demonstrate the flexibility and wide application of the developed system, six pia-only penetration tests were conducted with silicon probe shanks, including two tests with single-shank, two with dual-shank (as in Figure A.5(b)), and two with a four-shank probe. The shanks were cut from an 8-shank silicon probe (Buzsaki64 – H64LP probe by Neuronexus, Ann Arbor, MI). Each shank was 50 µm wide and 15 µm thick with 200 µm gap between adjunct shanks. The shanks overhang from the capillary tube by 3 mm, similar to conventional stereotactic-based probe insertion situations.

Table A. 3: Cantilever beam selection for each microelectrode based on preliminary insertion tests

Membrane		Pia		Pia and dura	
Silicon probe shank number	1	#1		-	
	2	#1			
	4	#2			
Microwire tip type		Sharp	Blunt	Sharp	Blunt
Microwire diameter (µm)	12	-	#1	-	-
	25	#1	#1	#3	#3
	50	#1	#1	#3	#3
	100	#2	#2	#3	#4

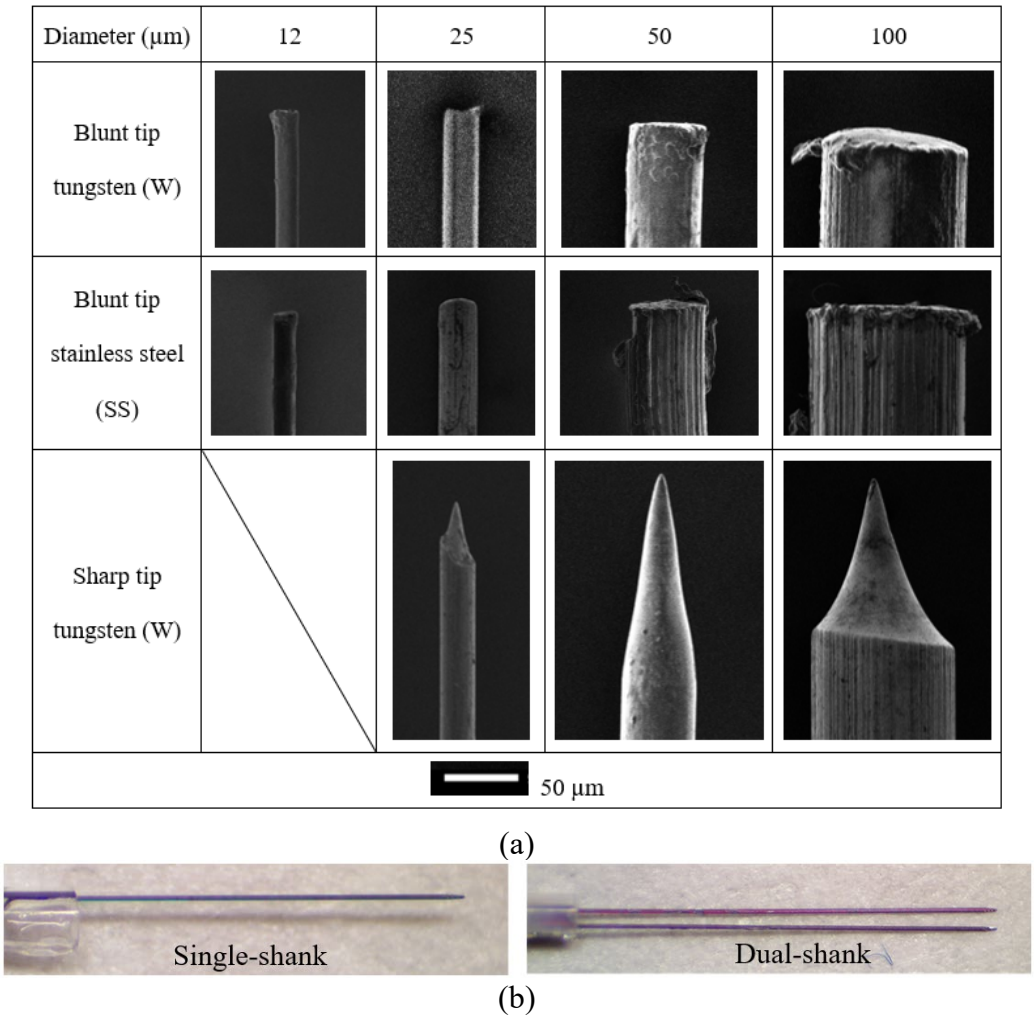


Figure A. 5: Microelectrodes used in the animal insertion tests: (a) scanning electron microscope images of various microwires and (b) single- and dual- shank silicon probes from Buzsaki64 – H64LP probe by Neuronexus fixed in capillary tube.

Preliminary insertion tests were conducted to determine the proper cantilever beam for each microelectrode device, as listed in Table A.3. During each insertion test, the rat brain was moved toward the microelectrode at a constant 100 μm/s insertion rate (speed) until membrane rupture or microelectrode buckling occurred. This speed was suggested by Sharp et al. [31] as a balance between tissue stiffness and electrode adhesion. After membrane rupture or microelectrode buckling, the microwire was retracted from the brain by the *x*-axis linear stage.

A.1.6 Data collection and processing

During each insertion, the cantilever beam deflection was monitored by the laser displacement sensor (Model LK-G10 by Keyence, Osaka, Japan). Displacement sensing data was sampled and stored at 500 Hz rate by a laser sensor controller with data storage (Model LK-G3001 by Keyence, Osaka, Japan). At the end of each insertion, the recorded displacement data set of d_c with 2 ms time increments were sent to a data-acquisition system for storage and further processing. Based on calibration results in Table A.2, the recorded d_c was then converted to force F_i and top plate displacement d_l at each time increment. The corresponding x-axis linear stage movement (d_t) was calculated by multiplying the constant feed rate (100 μm/s) by the insertion time. The d_l and d_t was then implemented in Equation (A.1) to find the displacement (d_i), which represented the tissue dimpling before membrane rupture.

A.2 Data analysis and results

A.2.1 Microwire insertion buckling rate

Out of the 238 effective microwire insertion tests conducted, the microwire penetrated the membrane in 215 trials and buckled in 23 trials, including 3 buckled trials for pia-only penetration and 20 for dura-pia penetration. Failure cases and buckling rates (expressing the number of buckled cases as a percentage of all trials) of each microwire type under each membrane penetration condition are presented in Table A.4.

Table A. 4: Membrane penetration success rates

Microwire Type	Diameter (μm)	Pia-only		Dura-pia	
		Penetrated / Total trials	Buckling rate	Penetrated / Total trials	Buckling rate
Sharp W	25	10 / 11	9.1%	10 / 14	28.6%
	50	11 / 11	0	14 / 14	0
	100	10 / 10	0	14 / 14	0
Blunt W	12	8 / 9	11.1%	-	-
	25	11 / 11	0	8 / 14	**42.9%**
	50	10 / 10	0	13 / 14	7.1%
	100	11 / 11	0	12 / 12	0
Blunt SS	12	10 / 11	9.1%	-	-
	25	10 / 10	0	6 / 14	**57.1%**
	50	11 / 11	0	13 / 14	7.1%
	100	10 / 10	0	13 / 13	0
Sum		112 / 115	2.6%	103 / 123	16.3%

A.2.2 Microwire force profile during insertion

Sample profiles of the microwire force vs. insertion time in in vivo anesthetized rat are as shown in Figure A.6. Force vibrations with a periodicity of 1 – 2 seconds were observed for in vivo tests of all microwires, which showed the animal's breathing under anesthesia [58]. For each insertion, the process start time was considered to be the moment when the microwire touched

the brain membrane surface. An initial rise in the force resulted from the microwire compressing and deforming (dimpling) the membrane without penetration, which caused a linear increase in the force. Slope of this initial rise mainly depended on the beam bending stiffness as the same insertion rate (100 μm/s) was used for all tests. Once the microwire ruptured the membrane, the force dropped suddenly. These force-drop points were captured to determine the membrane rupture force (insertion force) and the membrane dimpling at rupture based on Eq. (A.2). Unlike in previous studies [31,32,59,60] where the microwire stayed fixed on the rigid force sensor after penetration, in this study, the cantilever beam also bounced back after rupture together with the brain tissue rebounding. Such beam bouncing further inserted the microwire into the brain and generated a flat or slightly increasing force profile composed of the friction, cutting, and tissue clamping forces [61]. The interaction between beam bouncing, brain tissue rebounding, brain retraction, and complex brain structure (e.g., blood vessel) at the specific insertion location might cause variance (e.g., 50 μm wire in Figure A.6(b) and 100 μm wire in Figure A.6(c)) in this section of force profile. The force dropped again when the microwire retraction was initiated and the force might become negative because of frictional forces preventing the wire from extraction.

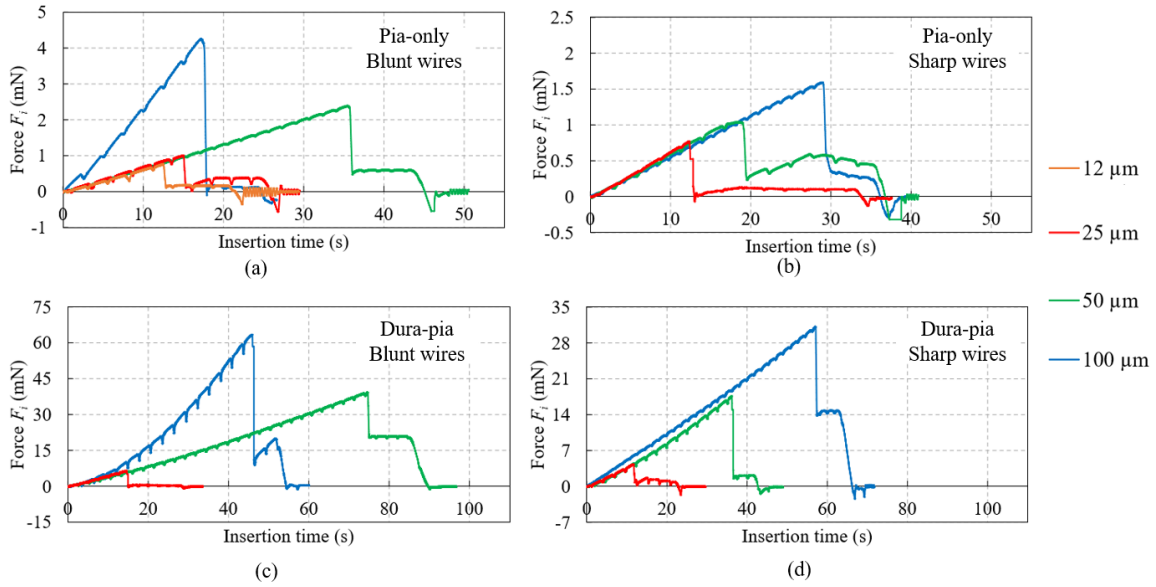


Figure A. 6: Sample force profiles of tungsten microwires: (a) blunt and (b) sharp microwires for pia-only penetration and (c) blunt and (d) sharp microwires for dura-pia penetration.

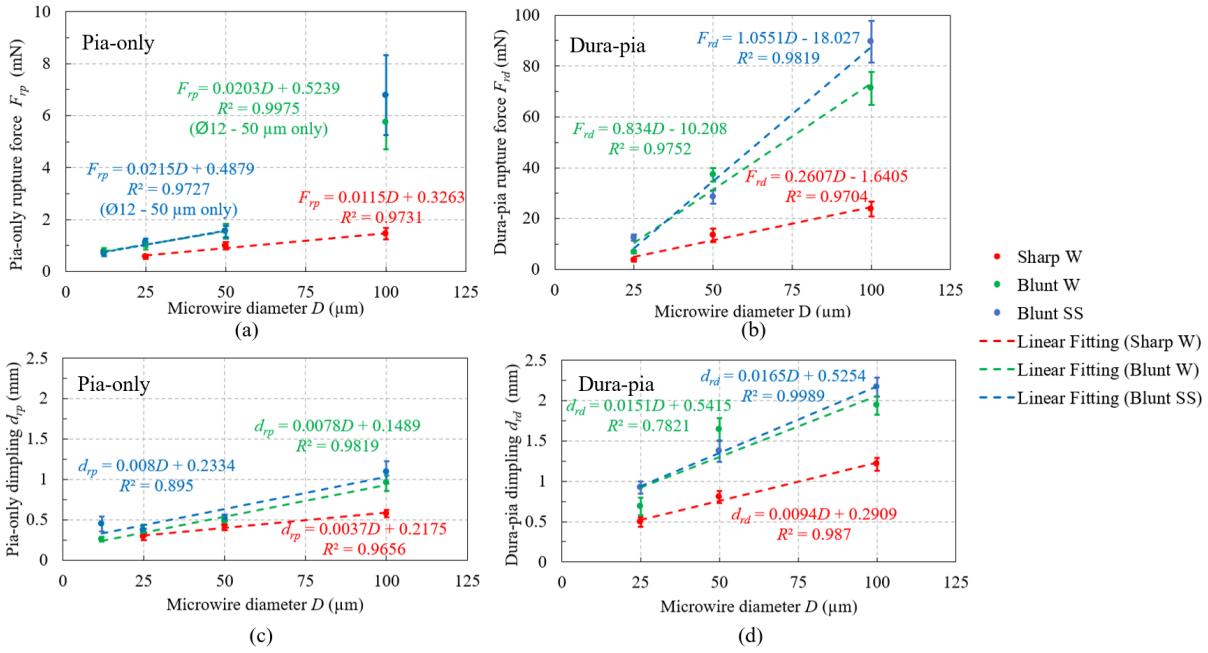


Figure A. 7: The (a) pia-only and (b) dura-pia rupture force during microwire insertions and dimpling depth at (c) pia-only and (d) dura-pia penetration by different microwires. Average value of each condition is plotted with standard error as the error bar.

A.2.3 Microwire force profile during insertion

Rupture force and dimpling depth at membrane rupture obtained from force profiles of all 215 successful trial are shown in Figure A.7 in terms of average value and standard error of each insertion condition. Overall speaking, dura-pia rupture force was an order of magnitude higher than pia-only rupture forces (note scale of vertical axes in Figures A.6, A.7(a), and A.7(b)) while the dimpling depth was about 2-3 times larger. As shown by the linear curve fittings based on the average value of each dataset in Figure A.7, for both in vivo pia-only and dura-pia penetration of rat brain, both the dimpling depth and rupture force are linearly related to the microwire diameter (instead of the cross-sectional area) with $R^2 > 0.97$ for rupture forces and $R^2 > 0.78$ for dimpling depth. Both rupture force and dimpling depth increased with larger microwire diameter and decreased by sharpened microwires.

A.2.4 Statistical analysis on the effect of microwire parameters

To investigate the effects of microwire parameters on the membrane rupture process, analysis of variance (ANOVA) was conducted with microwire material (tungsten or stainless steel), tip geometry (sharp or blunt), and diameter (12, 25, 50, 100 μm) as three independent variables. Six ANOVA were conducted with the rupture force, dimpling depth, and dimpling-to-rupture force ratio under both pia-only and dura-pia penetration conditions as the dependent variable. The results are as summarized in Table A.5 and a p value < 0.05 was considered statistically significant in this study, which is indicated in bold in the table. In every trial, the tip geometry and wire diameter significantly impacted rupture force, dimpling depth, and the ratio of dimpling depth to rupture force.

Table A. 5: Analysis of variances (ANOVA) results of microwire insertions

Dependent Variable	Independent Variable	*F*	*p*
Pia rupture force	Material	0.25	0.618
	Tip geometry	12.217	**0.001**
	Diameter	24.683	**<0.001**
Pia dimpling depth	Material	1.612	0.207
	Tip geometry	8.783	**0.004**
	Diameter	39.068	**<0.001**
Pia dimpling-to-rupture force ratio	Material	0.96	0.329
	Tip geometry	4.888	**0.029**
	Diameter	3.253	**0.025**
Dura & pia rupture force	Material	0.95	0.332
	Tip geometry	40.536	**<0.001**
	Diameter	63.409	**<0.001**
Dura & pia dimpling depth	Material	<0.001	0.983
	Tip geometry	67.803	**<0.001**
	Diameter	69.422	**<0.001**
Dura & pia dimpling-to-rupture force ratio	Material	0.2	0.656
	Tip geometry	36.058	**<0.001**
	Diameter	43.315	**<0.001**

A.2.5 Statistical analysis on the effect of microwire parameters

Without an easily accessible force measurement system, dimpling depth has been commonly used by the neuroscience community to indirectly evaluate the force. Among the force profile, the membrane rupture force is of specific interest as it leads to potential buckling of the microelectrode. The Pearson product-moment correlation coefficient (r) was calculated between the rupture force and dimpling depth at rupture. Given the ANOVA result that both diameter and tip geometry significantly impact the membrane dimpling-to-rupture force ratio, seven different data sets were used to calculate the r of pia-only penetration for: (1) all insertions, insertions with (2) sharp or (3) blunt microwires only, and insertions with (4) 12 μm, (5) 25 μm, (6) 50 μm, or (7) 100 μm diameter microwires only. Same analysis was conducted for dura-pia penetrations except for the 12 μm diameter set. The results are summarized in Table A.6 in terms of sample size (n), p-value (p), and Pearson correlation coefficient (r).

Statistically significant strong correlations (p <0.05 and absolute value of correlation coefficient > 0.7), as indicated in bold, were only observed for pia-only penetrations under same tip geometry or with 100 μm diameter. The correlation decreased with smaller diameter for pia-only penetration and only moderate correlation (absolute value of r between 0.3 and 0.7) existed for most dura-pia penetrations.

Table A. 6: Correlation between rupture force and dimpling depth at rupture

Membrane		Pia-only			Dura-pia		
Correlation result		*n*	*p*	*r*	*n*	*p*	*r*
All insertions		**112**	**<0.001**	**0.758**	103	<0.001	0.668
Tip geometry	Sharp	**31**	**<0.001**	**0.770**	38	0.069	0.298
	Blunt	**81**	**<0.001**	**0.764**	65	<0.001	0.605
Microwire Diameter	12	18	0.755	0.079	-	-	-
	25	31	0.049	0.357	24	0.001	0.615
	50	32	<0.001	0.588	40	0.048	0.314
	100	**31**	**<0.001**	**0.725**	39	<0.001	0.561

A.2.6 Silicon-based probe shank insertion results

Rupture force and dimpling depth at pia-only penetration by silicon probe shanks are as shown in Figure A.8. All six trials had pia penetration without buckling. It can be seen that due to interactions between shanks, rupture force and dimpling depth caused by dual- or four-shank devices tended to be smaller than twice or four times of the values generated by single-shank devices. It is worth noting that these experiments were conducted to demonstrate the wide application of the developed force measurement system. The six tests with sample size of two for each case may not be enough to draw any statistically significant conclusions in terms of absolute rupture force and dimpling depth values.

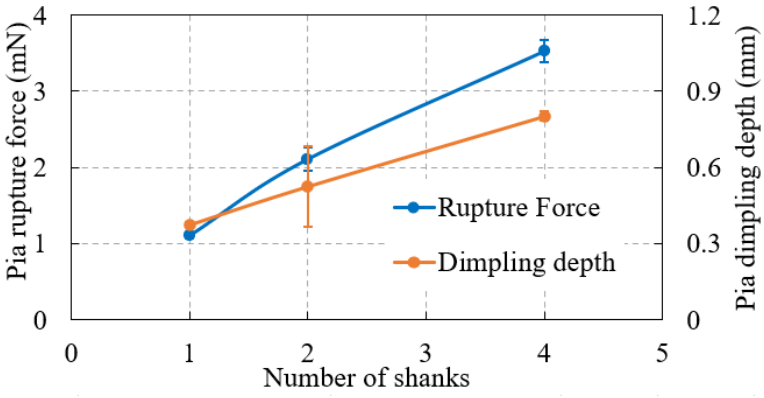


Figure A. 8: Rupture force and dimpling depth of pia-only penetration by silicon probes containing various number of shanks. Average value of each condition is plotted with standard error as the error bar.

A.3 Conclusions

A cantilever beam-based flexible high-resolution system for evaluation of microelectrode force and membrane dimpling depth has been developed. The easily duplicable and reconfigurable system was shown feasible for in vivo evaluation of both the pia-only and dura-pia penetration process with either microwires or silicon-based probe shanks. The following conclusions could be drawn based on microwire insertion tests conducted with the developed system:

(1) For both pia-only and dura-pia penetrations, the rupture force and membrane dimpling depth at rupture are linearly related to the microwire diameter.

(2) Microwire sharpening and diameter reduction have statistically significant impacts on rupture force, dimpling depth, and dimpling-to-rupture force ratio.

(3) Microwire material does not significantly impact the rupture force or dimpling depth but it affects the microwire buckling rate by determining the wire critical buckling load through its elastic modulus.

(4) The membrane dimpling depth and rupture force are not always strongly correlated, especially for small diameter microelectrodes (<100 μm) and dura-pia penetration cases, making

the dimpling depth observation adequate for only indirect qualitative estimation of the force profile. Direct measurement of the actual force profile would be recommended for buckling prevention analysis and detailed microelectrode design optimizations.

Bibliography

[1] Wickenden AD, Overview of Electrophysiological Techniques. Curr. Protoc. Pharmacol. 2000; 11: 11.1.1-11.1.17. https://doi.org/10.1002/0471141755.PH1101S64.

[2] Kozai TDY, The History and Horizons of Microscale Neural Interfaces. Micromachines 2018, Vol. 9, Page 445 2018; 9: 445. https://doi.org/10.3390/MI9090445.

[3] Xie K, Fox GE, Liu J, Tsien JZ, 512-Channel and 13-Region Simultaneous Recordings Coupled with Optogenetic Manipulation in Freely Behaving Mice. Front. Syst. Neurosci. 2016; 10:. https://doi.org/10.3389/fnsys.2016.00048.

[4] Du ZJ, Kolarcik CL, Kozai TDY, Luebben SD, Sapp SA, Zheng XS, Nabity JA, Cui XT, Ultrasoft microwire neural electrodes improve chronic tissue integration. Acta Biomater. 2017; 53: 46–58. https://doi.org/10.1016/J.ACTBIO.2017.02.010.

[5] Patel PR, Zhang H, Robbins MT, Nofar JB, Marshall SP, Kobylarek MJ, Kozai TDY, Kotov NA, Chestek CA, Chronic in vivo stability assessment of carbon fiber microelectrode arrays. J. Neural Eng. 2016; 13: 066002. https://doi.org/10.1088/1741-2560/13/6/066002.

[6] Guitchounts G, Markowitz JE, Liberti WA, Gardner TJ, A carbon-fiber electrode array for long-term neural recording. J. Neural Eng. 2013; 10:. https://doi.org/10.1088/1741-2560/10/4/046016.

[7] Welle EJ, Patel PR, Woods JE, Petrossians A, Della Valle E, Vega-Medina A, Richie JM, Cai D, Weiland JD, Chestek CA, Ultra-small carbon fiber electrode recording site optimization and improved in vivo chronic recording yield. J. Neural Eng. 2020; 17: 026037. https://doi.org/10.1088/1741-2552/ab8343.

[8] Patel PR, Na K, Zhang H, Kozai TDY, Kotov NA, Yoon E, Chestek CA, Insertion of linear 8.4 μm diameter 16 channel carbon fiber electrode arrays for single unit recordings. J. Neural Eng. 2015; 12:. https://doi.org/10.1088/1741-2560/12/4/046009.

[9] Schwarz DA, Lebedev MA, Hanson TL, Dimitrov DF, Lehew G, Meloy J, Rajangam S, Subramanian V, Ifft PJ, Li Z, Ramakrishnan A, Tate A, Zhuang KZ, Nicolelis MAL, Chronic, wireless recordings of large-scale brain activity in freely moving rhesus monkeys. Nat. Methods 2014; 11: 670–676. https://doi.org/10.1038/nmeth.2936.

[10] Mukamel R, Fried I, Human Intracranial Recordings and Cognitive Neuroscience. Annu. Rev. Psychol. 2012; 63: 511–537. https://doi.org/10.1146/annurev-psych-120709-145401.

[11] Drachman DA, Do we have brain to spare?, 2005.

https://doi.org/10.1212/01.WNL.0000166914.38327.BB.

[12] Henze DA, Borhegyi Z, Csicsvari J, Mamiya A, Harris KD, Buzsáki G, Intracellular Features Predicted by Extracellular Recordings in the Hippocampus In Vivo. J. Neurophysiol. 2000; 84: 390–400. https://doi.org/10.1152/jn.2000.84.1.390.

[13] Sakai K, What single-unit recording studies tell us about the basic mechanisms of sleep and wakefulness. Eur. J. Neurosci. 2019; https://doi.org/10.1111/ejn.14485.

[14] Baars BJ, Gage NM, Cognition, Brain, and Consciousness: Introduction to Cognitive Neuroscience, second, Academic Press, 2010.

[15] Burle B, Spieser L, Roger C, Casini L, Hasbroucq T, Vidal F, Spatial and temporal resolutions of EEG: Is it really black and white? A scalp current density view. Int. J. Psychophysiol. 2015; 97: 210–220. https://doi.org/10.1016/j.ijpsycho.2015.05.004.

[16] Dale AM, Liu AK, Fischl BR, Buckner RL, Belliveau JW, Lewine JD, Halgren E, Dynamic statistical parametric mapping: Combining fMRI and MEG for high-resolution imaging of cortical activity. Neuron 2000; 26: 55–67. https://doi.org/10.1016/S0896-6273(00)81138-1.

[17] Thach WT, Bastian AJ, Role of the cerebellum in the control and adaptation of gait in health and disease. Prog. Brain Res. 2004; 143: 353–366. https://doi.org/10.1016/S0079-6123(03)43034-3.

[18] Drake KL, Wise KD, Farraye J, Anderson DJ, BeMent SL, Performance of Planar Multisite Microprobes in Recording Extracellular Single-Unit Intracortical Activity. IEEE Trans. Biomed. Eng. 1988; 35: 719–732. https://doi.org/10.1109/10.7273.

[19] Campbell PK, Jones KE, Huber RJ, Horch KW, Normann RA, A Silicon-Based, Three-Dimensional Neural Interface: Manufacturing Processes for an Intracortical Electrode Array. IEEE Trans. Biomed. Eng. 1991; 38: 758–768. https://doi.org/10.1109/10.83588.

[20] Polikov VS, Tresco PA, Reichert WM, Response of brain tissue to chronically implanted neural electrodes. J. Neurosci. Methods 2005; 148: 1–18. https://doi.org/10.1016/j.jneumeth.2005.08.015.

[21] Karumbaiah L, Saxena T, Carlson D, Patil K, Patkar R, Gaupp EA, Betancur M, Stanley GB, Carin L, Bellamkonda R V., Relationship between intracortical electrode design and chronic recording function. Biomaterials 2013; 34: 8061–8074. https://doi.org/10.1016/j.biomaterials.2013.07.016.

[22] Chung JE, Joo HR, Fan JL, Liu DF, Barnett AH, Chen S, Geaghan-Breiner C, Karlsson MP, Karlsson M, Lee KY, Liang H, Magland JF, Pebbles JA, Tooker AC, Greengard LF, Tolosa VM, Frank LM, High-Density, Long-Lasting, and Multi-region Electrophysiological Recordings Using Polymer Electrode Arrays. Neuron 2019; 101: 21-31.e5. https://doi.org/10.1016/j.neuron.2018.11.002.

[23] Musk E, An Integrated Brain-Machine Interface Platform With Thousands of Channels. J. Med. Internet Res. 2019; 21: e16194. https://doi.org/10.2196/16194.

[24] Patel PR, Carbon FIiber Microelectrode Arrays for Neuroprosthetic and Neuroscience Applications, University of Michigan, 2015.

[25] Rose JD, Weishaar DJ, Tapered tungsten fine-wire microelectrode for chronic single unit recording. Brain Res. Bull. 1979; 4: 435–437. https://doi.org/10.1016/S0361-9230(79)80022-2.

[26] Liao YF, Tsai ML, Yen CT, Cheng CH, A simple method for fabricating microwire tetrode with sufficient rigidity and integrity without a heat-fusing process. J. Neurosci. Methods 2011; 195: 211–215. https://doi.org/10.1016/j.jneumeth.2010.12.017.

[27] Kim S-J, Manyam SC, Warren DJ, Normann RA, Electrophysiological Mapping of Cat Primary Auditory Cortex with Multielectrode Arrays. Ann. Biomed. Eng. 2006; 34: 300–309. https://doi.org/10.1007/s10439-005-9037-9.

[28] 3D Matrix Array - Global Bio Inc. n.d.; http://www.glo-bio-inc.com/product/3d-matrix-array-3/ (accessed March 15, 2022).

[29] MatWeb, Solvay Thornel® T-650/35 3K Carbon Fiber, Polyacrylonitrile (PAN) Precursor. 2012; http://www.matweb.com/search/datasheet.aspx?matguid=7e9aca60a2e84538a4e8038784f2b629&ckck=1.

[30] Budai D, Carbon fiber-based microelectrodes and microbiosensors, in: Intell. Biosens., 2010: pp. 269–288. www.intechopen.com (accessed November 29, 2019).

[31] Sharp AA, Ortega AM, Restrepo D, Curran-Everett D, Gall K, In vivo penetration mechanics and mechanical properties of mouse brain tissue at micrometer scales. IEEE Trans. Biomed. Eng. 2009; 56: 45–53. https://doi.org/10.1109/TBME.2008.2003261.

[32] Obaid AM, Wu Y-W, Hanna M-E, Nix WD, Ding JB, Melosh NA, Ultra-sensitive measurement of brain penetration with microscale probes for brain machine interface considerations. BioRxiv 2018; 454520. https://doi.org/10.1101/454520.

[33] Obaid A, Wu Y-W, Hanna M, Jáidar O, Nix W, Ding J, Melosh N, Ultra-sensitive measurement of brain penetration mechanics and blood vessel rupture with microscale probes. BioRxiv 2020; 2020.09.21.306498. https://doi.org/10.1101/2020.09.21.306498.

[34] Guitchounts G, Cox D, 64-Channel Carbon Fiber Electrode Arrays for Chronic Electrophysiology. Sci. Rep. 2020; 10: 1–9. https://doi.org/10.1038/s41598-020-60873-y.

[35] Welle EJ, Woods JE, Jiman AA, Richie JM, Bottorff EC, Ouyang Z, Seymour JP, Patel PR, Bruns TM, Chestek CA, Sharpened and Mechanically Durable Carbon Fiber Electrode Arrays for Neural Recording. IEEE Trans. Neural Syst. Rehabil. Eng. 2021; 29: 993–1003. https://doi.org/10.1109/TNSRE.2021.3082056.

[36] Xu H, Hsiao MC, Song D, Berger TW, Recording place cells from multiple sub-regions of the rat hippocampus with a customized micro-electrode array, in: 2014 36th Annu. Int. Conf. IEEE Eng. Med. Biol. Soc. EMBC 2014, Institute of Electrical and Electronics Engineers Inc., 2014: pp. 4876–4879. https://doi.org/10.1109/EMBC.2014.6944716.

[37] Millar J, Pelling CWA, Improved methods for construction of carbon fibre electrodes for extracellular spike recording. J. Neurosci. Methods 2001; 110: 1–8. https://doi.org/10.1016/S0165-0270(01)00411-3.

[38] Inagaki K, Heiney SA, Blazquez PM, Method for the construction and use of carbon fiber multibarrel electrodes for deep brain recordings in the alert animal. J. Neurosci. Methods 2009; 178: 255–262. https://doi.org/10.1016/j.jneumeth.2008.12.009.

[39] Massey TL, Santacruz SR, Hou JF, Pister KSJ, Carmena JM, Maharbiz MM, A high-density carbon fiber neural recording array technology. J. Neural Eng. 2019; 16:. https://doi.org/10.1088/1741-2552/aae8d9.

[40] Lee Y, Jun SB, Carbon fiber based microeletrode with biodegradable silk for in vivo neural recording, in: 2020 Int. Conf. Electron. Information, Commun. ICEIC 2020, Institute of Electrical and Electronics Engineers Inc., 2020. https://doi.org/10.1109/ICEIC49074.2020.9051026.

[41] Patel PR, Popov P, Caldwell CM, Welle EJ, Egert D, Pettibone JR, Roossien DH, Becker JB, Berke JD, Chestek CA, Cai D, High density carbon fiber arrays for chronic electrophysiology, fast scan cyclic voltammetry, and correlative anatomy. J. Neural Eng. 2020; 17:. https://doi.org/10.1088/1741-2552/abb1f6.

[42] Huan Y, Gill JP, Fritzinger JB, Patel PR, Richie JM, Della Valle E, Weiland JD, Chestek CA, Chiel HJ, Carbon fiber electrodes for intracellular recording and stimulation. J. Neural Eng. 2021; 18: 066033. https://doi.org/10.1088/1741-2552/AC3DD7.

[43] McCarthy PT, Otto KJ, Rao MP, Robust penetrating microelectrodes for neural interfaces realized by titanium micromachining. Biomed. Microdevices 2011; 13: 503–515. https://doi.org/10.1007/s10544-011-9519-5.

[44] Dong T, Chen L, Shih A, Laser Sharpening of Carbon Fiber Microelectrode Arrays for Brain Recording. J. Micro Nano-Manufacturing 2020; 8:. https://doi.org/10.1115/1.4049780.

[45] Chen L, Hartner J, Dong T, Li A, Watson B, Shih A, Flexible High-Resolution Force and Dimpling Measurement System for Pia and Dura Penetration during in Vivo Microelectrode Insertion into Rat Brain. IEEE Trans. Biomed. Eng. 2021; 68: 2602–2612. https://doi.org/10.1109/TBME.2021.3070781.

[46] Goode L, Are Exoskeletons the Future of Physical Labor? Exoskelet. Rep. 2017; https://www.theverge.com/2017/12/5/16726004/verge-next-level-season-two-industrial-exoskeletons-ford-ekso-suitx.

[47] Schindelin J, Arganda-Carreras I, Frise E, Kaynig V, Longair M, Pietzsch T, Preibisch S, Rueden C, Saalfeld S, Schmid B, Tinevez JY, White DJ, Hartenstein V, Eliceiri K, Tomancak P, Cardona A, Fiji: An open-source platform for biological-image analysis. Nat. Methods 2012; 9: 676–682. https://doi.org/10.1038/nmeth.2019.

[48] Schneider CA, Rasband WS, Eliceiri KW, NIH Image to ImageJ: 25 years of image analysis. Nat. Methods 2012; 9: 671–675. https://doi.org/10.1038/nmeth.2089.

[49] Richie JM, Patel PR, Welle EJ, Dong T, Chen L, Shih AJ, Chestek CA, Open-source Toolkit: Benchtop Carbon Fiber Microelectrode Array for Nerve Recording. JoVE (Journal Vis. Exp. 2021; e63099. https://doi.org/10.3791/63099.

[50] Yin Y, Binner JGP, Cross TE, Marshall SJ, The oxidation behaviour of carbon fibres. J. Mater. Sci. 1994; 29: 2250–2254. https://doi.org/10.1007/BF01154706.

[51] Massey TL, Lee JH, Ray M, Sathe NS, Liu X, Pister KSJ, Maharbiz MM, Open-source automated system for assembling a high-density microwire neural recording array. 2016 Int. Conf. Manip. Autom. Robot. Small Scales, MARSS 2016 2016; https://doi.org/10.1109/MARSS.2016.7561750.

[52] Duda RO, Hart PE, Use of the Hough transformation to detect lines and curves in pictures. Commun. ACM 1972; 15: 11–15. https://doi.org/10.1145/361237.361242.

[53] Borosilicate Glass Material Properties - Imetra, Inc. n.d.; https://www.imetra.com/borosilicate-glass-material-properties/.

[54] Parylene Electrical Properties. n.d.; https://pctconformalcoating.com/parylene/parylene-electrical-properties/.

[55] Friction - Friction Coefficients and Calculator. n.d.; https://www.engineeringtoolbox.com/friction-coefficients-d_778.html.

[56] The Benefits of Parylene - Curtiss-Wright Parylene Coatings. n.d.; https://parylene.co.uk/about-parylene/.

[57] Ali MA, Hu C, Yttri EA, Panat R, Ali MA, Hu C, Panat R, Yttri EA, Recent Advances in 3D Printing of Biomedical Sensing Devices. Adv. Funct. Mater. 2022; 32: 2107671. https://doi.org/10.1002/ADFM.202107671.

[58] Thomas J, Lerche P, Anesthesia and Analgesia for Veterinary Technicians, 5th ed., Elsevier, 2017.

[59] Jensen W, Yoshida K, Hofmann UG, In-vivo implant mechanics of flexible, silicon-based ACREO microelectrode arrays in rat cerebral cortex. IEEE Trans. Biomed. Eng. 2006; 53: 934–940. https://doi.org/10.1109/TBME.2006.872824.

[60] Haj Hosseini N, Hoffmann R, Kisban S, Stieglitz T, Paul O, Ruther P, Comparative study on the insertion behavior of cerebral microprobes, in: 29th Annu. Int. Conf. IEEE Eng.

Med. Biol. Soc., IEEE, Lyon, France, 2007: pp. 4711–4714. https://doi.org/10.1109/IEMBS.2007.4353391.

[61] Okamura AM, Simone C, O'Leary MD, Force Modeling for Needle Insertion Into Soft Tissue. IEEE Trans. Biomed. Eng. 2004; 51: 1707–1716. https://doi.org/10.1109/TBME.2004.831542.